AFCRL-64-26
JANUARY 1964

Research Report

The Structure of Occlusions as Determined From Serial Ascents and Vertically-Directed Radar

CARL W. KREITZBERG

METEOROLOGY LABORATORY PROJECT 8641
AIR FORCE CAMBRIDGE RESEARCH LABORATORIES, OFFICE OF AEROSPACE RESEARCH, UNITED STATES AIR FORCE

AFCRL-64-26
JANUARY 1964

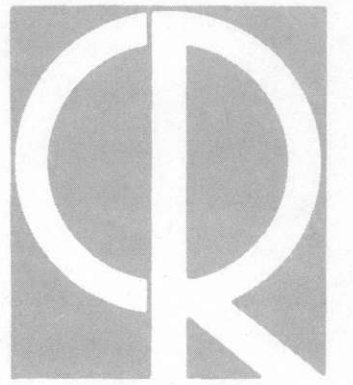

Research Report

The Structure of Occlusions as Determined From Serial Ascents and Vertically-Directed Radar

CARL W. KREITZBERG

METEOROLOGY LABORATORY PROJECT 8641

AIR FORCE CAMBRIDGE RESEARCH LABORATORIES, OFFICE OF AEROSPACE RESEARCH, UNITED STATES AIR FORCE, L.G. HANSCOM FIELD, MASS.

Abstract

The thermal, cloud, and precipitation structures of occluded frontal systems on both the meso- and synoptic-scales are examined. The data used include serial-ascent radiosonde observations of five systems and the time-height precipitation structure of these and many other frontal systems as obtained using vertically-directed, 1.87-cm radar.

For the serial-ascent cases, mesoscale vertical motions have been computed using a variation of the 'adiabatic method' which requires only single-station radiosonde data. The reliability of each vertical velocity is also computed to indicate the proper weighting of the values in the analysis. The reliabilities justify placing confidence in the principal features of the mesoscale vertical motion fields. The 'static energy' function ($\sigma \equiv gz + c_{pd} T + L_o m$), which is quasi-conservative for adiabatic and pseudo-adiabatic processes, has been found to be very useful for interpreting structures and processes, including turbulent mixing, in cloudy regions of the troposphere.

The mesoscale thermal structure of frontal zones is characterized by multiple, narrow hyperbaroclinic subzones within the broader baroclinic zones separating relatively barotropic air masses. A front based on synoptic data cannot accurately depict the details of the mesoscale structure, but it can approximately locate the principal subzones within the broader baroclinic zone. The mesoscale vertical motions are much more complex than classical frontal theory implies, but certain interesting and recurring features are observed.

The cloud and precipitation structure of occlusions is highly variable, and a model or average sequence must be interpreted as either the average state or a

particular example. Computations based on observed frequencies indicate that even a loosely defined model can be expected to exist in only 14% of the occlusions. The variety of processes and factors which significantly affect cloud and precipitation structures is examined and is found to account for the observed variability. These processes and factors deserve consideration, rather than general models, in the prediction of weather to be expected with any particular occlusion.

Contents

Illustrations

Tables

Symbols *

ACC	Acceleration term in advective temperature change equation – see Equation (A-7)
ADV	Approximate advective temperature change – see Equation (A-9)
c_p, c_{pd}, c_{pm}	Specific heats at constant pressure; subscripts 'd' and 'm' refer to dry and moist air respectively.
e, e_s	Vapor pressure over water; subscript 's' refers to value at saturation
f	Coriolus parameter ($f \equiv 2\Omega \sin \Phi$).
g	Acceleration of gravity
$\vec{i}, \vec{j}, \vec{k}$	Unit vectors along the x, y, and z axes, respectively.
K	Eddy diffusivity of static energy – equals eddy diffusivity of water vapor and sensible heat if these latter diffusivities are assumed to be identical.
K_m	Eddy diffusivity of momentum.
L, L_0	Latent heat of vaporization of water; the subscript '0' refers to its value at T = 0°C.
m, m_s	Mixing ratio; subscript s refers to the value at saturation.
$\vec{n}$	Unit vector normal to and to the left of the horizontal wind vector ($\vec{n} = \vec{k} \times \vec{t}$), except in Section 3.5 where it is the unit vector along $\vec{\nabla} \sigma$.
p	Pressure.
PRC	Parcel rate of condensation (see p. 14)

* These symbols have the same meanings in all sections.

R, R_d, R_v	Specific gas constants; subscripts 'd' and 'v' refer to dry air and water vapor, respectively.
Rh, Rhi	Relative humidity with respect to water and ice (i) .
t	Time
$\vec{t}$	Unit vector in the direction of the horizontal velocity.
T	Temperature – in °K unless otherwise specified.
u, v	Velocity components along the x and y axes, respectively.
V, V_H, V_g	Wind speed; subscripts 'H' and 'g' refer to horizontal and geostrophic winds respectively.
$\vec{V}, \vec{V}_H, \vec{V}_g$	Wind velocity vectors; subscripts 'H' and 'g' refer to horizontal and geostrophic winds, respectively.
w	Vertical velocity in meteorological coordinates, dz/dt .
x, y, z	Meteorological coordinate axes; east, north, and up, respectively.
Z	Greenwich Civil (or Mean) Time (GCT or GMT).
$\gamma, \gamma_d, \gamma_s$	Temperature lapse rates; subscripts 'd' and 's' refer to dry and saturate adiabatic ascent, respectively, while γ is the spatial lapse rate.
Γ	Adiabatic temperature lapse rate; either γ_d or γ_s depending on whether or not the parcel is saturated.
$\delta\chi$	Uncertainty in the measurement of χ , normally taken to be an infinitesimal.
$\frac{\delta\chi}{\delta t}$	Rate of change of χ following the motion of surface of constant static energy.
$\vec{\nabla}, \vec{\nabla}_z, \vec{\nabla}_p$	Hamilton operators: $\vec{\nabla} \equiv \vec{i}\ \frac{\partial}{\partial x} + \vec{j}\ \frac{\partial}{\partial y} + \vec{k}\ \frac{\partial}{\partial z}$; $\vec{\nabla}_z \equiv \vec{i}\ \frac{\partial}{\partial x} + \vec{j}\ \frac{\partial}{\partial y}$; $\vec{\nabla}_p \equiv \vec{i}\ \frac{\partial}{\partial x}\Big\|_p + \vec{j}\ \frac{\partial}{\partial y}\Big\|_p$.
ρ	Density of air.
σ	Static energy ($\sigma \equiv gz + c_{pd}T + L_0M$) .
ϕ	Angle of a vector – measured in the horizontal plane counter-clockwise from the x-axis .
Φ	Geodetic latitude.
ω	Vertical velocity in pressure coordinates, dp/dt .
Ω	Rotation rate of earth.

Foreword

This report resulted from research conducted at the University of Washington under the supervision of Dr. Richard J. Reed, and was completed after the author began his employment at the Air Force Cambridge Research Laboratories. The research at the University was sponsored by AFCRL under contract No. AF19(604)-5192. This report is essentially the same as the doctoral dissertation submitted to the University of Washington in August 1963.

The Structure of Occlusions as Determined from Serial Ascents and Vertically-Directed Radar

1. INTRODUCTION

The purpose of this study is to investigate the structure of occluded frontal systems, primarily on the mesoscale, through short-interval radiosonde observations and continuous vertically-directed radar data. This study was prompted by difficulties encountered in an attempt to develop a cloud and precipitation model for the occlusion. The Radar Data Studies Project at the University of Washington* using vertically-directed radar found a large variability in the precipitation structure of storms. This observation, along with difficulties and inconsistencies in frontal analysis, raised questions as to the detailed structure of frontal systems and cloud and precipitation features. The literature contains numerous references to observations which indicate that the real atmosphere does not conform to classical frontal theories. Conflicting views of meteorologists as to frontal theory and methods of analysis greatly limit the usefulness of frontal concepts. The successful integration of frontal theory into numerical analysis and forecasts is dependent on a clearer understanding of the nature of real fronts.

Attention will be directed toward the frontal systems, that is, regions of relatively intense baroclinity including the warm, cold, and occluded fronts. While

* Sponsored by the Geophysics Research Directorate of the Air Force Cambridge Research Laboratories.

(Received for publication 22 October 1963)

frontal systems include only a fraction of the troposphere, they are active participants in extratropical weather phenomena, and it is very important to understand these features.

This study is basically observational in character rather than theoretical, but efficient observational deduction requires full use of physical principles and theoretical advances as well as dynamically important concepts and parameters. While less precise than theory and less quantitative than many measurements, meso- and synoptic-scale observational studies are essential for gaining an understanding of processes on these scales. The necessarily restricted theoretical models are dependent on observations for their inspiration and/or verification.

The data used in this investigation were gathered during the Radar Data Studies Project and include time-height radar records and synoptic-scale (12 hourly soundings) time sections from a twenty-three month period. In addition, special short-interval radiosonde ascents were made during five periods.

The data, then, supply information on a large number (over 100) of ordinary fronts. Even the limited number of serial-ascent cases include old and new, weak and strong, diffuse and sharp fronts. The mesoscale serial ascents provide insight into many problems encountered in the more routine synoptic-scale studies and a check on procedures and beliefs common in synoptic meteorology. The detailed radar records for many storms can now be viewed in light of the correspondence of radar records and the detailed thermal and wind fields in the serial-ascent cases.

Admittedly, all the data are influenced by the location of the observations, Seattle, Washington. Important regional and topographical effects must be expected. It is believed that the local factors can be taken into account so that the majority of the conclusions will have general applicability.

It is the purpose of this investigation, therefore, to determine the structure of occluded frontal systems and the related cloud and precipitation features. Such information is essential for understanding the processes and constructing or verifying theoretical models.

2. REVIEW OF OCCLUDED CYCLONE MODELS

2.1 Frontal Models

The occluded front and the classical occlusion process were introduced by Bergeron to complete the life cycle of the cold and warm fronts. While the frontal terminology was established around 1919, cyclone models had been developed and cold fronts examined prior to 1900. The distinction between polar and equatorial currents was identified scientifically as early as 1840; and, at that time, it was speculated that the interaction of these currents was a primary storm-producing

mechanism. The formal and extensive identification of air masses was introduced by Bergeron. For a more detailed discussion of the historical development of frontal concepts, see Reference [1] or Section 17.0 of Reference [2].

The principal observational support for frontal models was initially limited to surface synoptic charts, sparse soundings, and a dense surface-observation network in Norway. The observational basis was greatly extended by swarm ascents made in Europe between 1928 and 1935.[3] This program involved the release of balloon-sondes, at intervals on the order of one hour, from several cooperating European countries on particular days. The spacing of observations was somewhat a matter of chance because the balloon-sonde instrument package had to be recovered for the data to be obtained. These time sections, obtained simultaneously from several European stations, provided the major upper-air support to the frontal theories until World War II.

By the middle 1930's, Bergeron had consolidated his concepts of the occlusion and air masses with the work of his associates on cyclone dynamics.[4] Many factors had been introduced by observations and supporting theoretical work which modified the simple models into more realistic models. Consideration was given to such factors as: (1) friction, (2) masking of frontal location by inversions, (3) orographic modifications, and (4) the distinction between ana- and kata-type cold fronts and warm- and cold-type occlusions. Frontal theory, as it existed in the 1930's, is referred to as the classical Norwegian theory.

Frontal concepts—as presented in popular treatments, in introductory and intermediate meteorological texts, and in handbooks—are essentially the classical Norwegian theories. In view of the tremendous increase in observations capable of verifying or refuting their ideas, it is a tribute to those who developed the models from very limited data that these models remain in widespread use. As Sutcliffe[5] points out, extensive deviations have been observed between nature and the classical models, and extensive criticism of those models has been forthcoming. However, the classical models have not, in general, been replaced. They are only modified slightly with emphasis given to the more common deviations of nature from the models. The classical models of Bergeron, with some updating, are presented clearly in Chapter 14 of Reference [2], and no useful purpose would be served in describing the models here.

A major modification of the classical viewpoint was presented by Palmén,[6] who emphasized that structures possessing all the characteristics of a mature occlusion can, and often do, form without evolving by the classical process (the merging of a cold and warm front). The occlusion of a wave on the polar front is not necessary for the development of the occluded front and the occluded cyclone.

Godson[7] questioned the very existence of the occluded front in many mature cyclones. He expressed the opinion that as cyclones mature, warm air at upper

levels is drawn far north of the surface warm sector. This trough of warm air aloft is preceded by the upper warm front and followed by an upper cold front. This structure, commonly referred to as a trowal, is reflected at the surface by a pressure trough beneath the locus of the intersection of the upper warm and cold fronts. Depending on the case, the surface trough may or may not possess frontal characteristics; but it is the trough of warm air aloft ('trowal') that has dynamic significance. According to Godson,[8] this model, without an occluded front, "completely and adequately fits 95% of all occluded frontal waves crossing the west coast of North America."

The importance of a trowal-like structure rather than the occluded front has been emphasized since the 1940's by A. L. Jacobson,* although his paper[9] has not been published. His views resulted from time section analyses of potential temperature at the Seattle office of the U. S. Weather Bureau. He felt that the structure of Pacific coast 'occlusions' could be best specified by locating the upper limit of the sloping zones of intense θ-gradient aloft and the cold edge of the transition zone to the post-frontal cold air mass. He did not find evidence to support the existence of a significant frontal surface extending from the upper fronts to the ground. The upper limit of the sloping θ-gradient zone aloft corresponds to the upper warm and cold fronts of the classical model, while the edge of the cold air mass corresponds more nearly to the classical bent-back occlusion or the secondary cold front.

Further questions have been raised regarding the nature of the warm and cold fronts. These problems must be considered in this study, for the nature of occluded fronts is a corrolary to the nature of fronts in general. Only questions on frontal structure will be reviewed here; the question of frontal analysis problems has been discussed very realistically by Sutcliffe,[5] and a complete review of recent literature pertaining to the analysis question has been presented by Taljaard, et al.[10]

The relation of migrating and modifying air masses, frontogenesis, and frontolysis was re-examined by Godson.[7] He followed Bergeron's premise that air masses and the intervening fronts are the two basic tropospheric models. The modfication of one air mass into another implies the movement of the front relative to the air at some stage. Godson suggested that simultaneous frontolysis of the polar front in one region and frontogenesis in another must accompany the transition of southward moving polar air into tropical air. Vertical motion was included as an air mass conversion process, while Bjerknes and Palmén[3] had earlier preferred not to label as polar, tropical air which had been appreciably cooled due to ascent ahead of the polar front. Godson also suggested that the existence of a partially modified polar air mass necessitates the addition of an interpolar front to separate the warm polar air masses from the cold polar air masses.

---

* Present affiliation: Meteorologist-in-Charge, U. S. Weather Bureau, Great Falls, Montana.

Perhaps one of the most serious questions about frontal zones is whether or not they are continuous from one level to the next. When a frontal zone is located on the 500-mb chart, is it an extension of the zone located on the surface chart, or is it a separate upper level hyperbaroclinic zone? Palmen[6] joined the frontal zones at the lower and upper levels with a 'principal' frontal surface. Reed[11] mentions that the likelihood of different mechanisms producing lower and upper level fronts would rule out any necessary spatial connection between these fronts. The relation of the upper fronts to the tropopause is discussed by Reed and Danielsen.[12] On the basis of data from 'Project Jet Stream,' Endlich and McLean[13] distinguished between the 'jet front' extending from the tropopause region to below 500 mb and a separate, lower-level polar front. Hence, the jet front may correspond to the intense baroclinity observed by Bjerknes and Palmen[3] in the tropical air above the polar front. Another interesting investigation of the interaction of upper and lower frontal structures is presented by Newton,[14] who deals with the formation of the upper front to the west of a trough and its migration around to the east side of the trough to join with and intensify the lower-level polar front.

Mathematical models can treat fronts as zero-order of first-order discontinuities in temperature; or, in the absence of discontinuities, a region of large baroclinity may be considered. Since the mathematics of zero-order discontinuities is the simplest, this type of model was constructed first, to be followed by consideration of the first-order models. Baroclinic theory can explain cyclogenesis rather well without reverting to discontinuities at all.[15] In nature, some surfaces of nearly zero-order discontinuities in temperature have been found. Hyper-baroclinic zones bounded by nearly first-order discontinuity surfaces on one or both sides are common. However, it is not necessarily true that these discontinuity surfaces are more important to cyclogenesis than the broader, less intense baroclinic zones.

It has been suggested by Sutcliffe[5] that the broad baroclinic zones are likely to be more important than the narrow intense frontal zones. Reed[11] agrees with the possible over-riding importance of the broad zone relative to the narrow zone. Danielsen and McClain[16] conclude that the thermal field of cyclonic disturbances in cross sections can be viewed as domes of rapidly moving cold air. The leading and trailing edges of these domes are baroclinic regions in which frontal zones may or may not be found. With data from aircraft flights in the vicinity of fronts, Sawyer[17] found the broad baroclinic zones to average 600 miles in width with an 8°C temperature change, while the narrower intense zone averages 130 miles in width with a contrast of 5°C. He concludes that zones narrower than fifty miles are unusual in the free atmosphere.

From a review of the literature, it appears that conditions in nature range from the zero-order front to the broad baroclinic zones with no distinct bounding surfaces. Nature is not restricted to a certain number of frontal zones, and upper

and lower hyper-baroclinic zones are not necessarily connected in space. The larger scale of motions may be explained without frontal concepts, but on the meso-scale very sharp and important fronts exist.

2.2 Cloud and Precipitation Models

The classical occlusion cloud and precipitation model was developed by Bergeron and is presented in detail in Godske, et al.[2] Bergeron distinguished between a warm- and a cold-type occlusion model. The warm-type occlusion model has prefrontal weather similar to the warm front model with the shield of cirrus followed by altostratus and then nimbostratus. The cloud tops lower as the occlusion approaches. The cold-type occlusion has deeper clouds and more intense precipitation immediately ahead of the occlusion.

The cyclone model proposed in 1887 by Abercromby (see Ref. [2], p. 623) contains the essential features of the classical occlusion weather models. Brooks[18] described the weather features in a cyclone without reference to fronts. Boucher[19] presented a model of the precipitation structure of New England cyclones derived from vertically-directed radar observations. This model, obtained by averaging data from many cyclones, implies the classical prefrontal lowering and thickening of the clouds followed by postfrontal stratocumulus.

A cloud model for cyclones derived from satellite cloud observations is presented by Boucher and Newcomb.[20] Characteristic gross features which indicate the stage of development of the system are discussed. The progressive development of the cloud systems implies that a single cloud model can be expected to represent only systems at a certain stage of development. A model for radar precipitation echo distribution around an occluded cyclone is given by Nagle and Serebreny.[21] The model is based on data from a network of PPI radars off the west coast of the United States. The cloud and precipitation bands or 'spokes' revolving about the cyclone are prominent features of the models derived from both satellite and PPI-radar data.

Few cloud and precipitation models have been prepared for occluded frontal systems from direct information on both the thermal and cloud structures. The study of Sawyer[17] based on aircraft observations in frontal regions is, therefore, of particular significance. He found that a dry zone was very common in the vicinity of fronts, occurring in the transition zone one-half of the time. In the remaining cases, the dry zone was located either in the warm or cold air masses. He found indications of the formation of precipitation in transition zones and a large variation in cloud structure from front to front. The clouds were principally in the warm air masses in nine cases, and they were partially in the warm air and partially in the transition zone in seven cases. Hoecker[22] and Hall[23] reported on

the study of precipitation mechanisms in Pacific coast storms. They emphasized the complex multilayered cloud systems and the action of higher crystal-producing clouds in seeding the lower clouds. Conover and Wollaston[24] also emphasized the separation of upper cloud regimes from the lower clouds in a cyclonic storm. The upper clouds apparently formed over the cold front. After moving ahead of the cold front the upper clouds seeded the lower clouds and sometimes developed into showers or squall lines. The advanced portion of the upper clouds would at times become entirely separated from the clouds over the cold front. Austin and Blackmer[25] demonstrated the variability in cold front precipitation and Sansom[26] contrasted the weather associated with ana- and kata- type cold fronts.

It is apparent that cloud and precipitation models derived from various types of observations of occlusions are in general agreement. Also, systems in different stages of development will have different cloud and precipitation structures, and there is substantial variability even among systems at the same stage of development. The manner in which these cloud and precipitation models can be utilized depends on the variability of nature from the model patterns, and this variability has not been adequately determined.

2.3 Use of Models

The preceding review has continually referred to 'models.' It is well to consider carefully the meaning and purpose of these constructions. The idea, as expressed by Hertz (see Ref. [2], p. 3), a teacher of V. Bjerknes, is to obtain a mental image of nature which will lead our thought processes to the image corresponding to conditions in nature at a later time. In a sense, this is a transformation from nature to the abstract, a projection in the abstract to a future time and a transformation back to nature. In meteorological problems we can make an image of only a simplified version of nature; we can project only imperfectly, and the reverse transformation to nature is incapable of reproducing more than a skeleton structure.

A partial solution to the modeling problem[2] is to consider two types of models – the 'dynamic model,' which can be projected mathematically, and the 'synoptic model,' which is qualitative and portrays conditions in nature more closely than can the dynamic model. The goal is to extend the dynamic models to merge with the synoptic models. The synoptic model must be made as simple as possible without losing those features which will lead to the correct forecast of nature. Until the dynamic and synoptic models merge, no model is final; all are prototypes. The most frequent criticism made of the classical models is that they do not describe nature accurately. Is it that the models do not describe nature or that the models are applied where they do not describe nature?

Dynamic models and dynamic principles are tools to be used in conjunction with observations in the development and improvement of synoptic models. The dynamic tools serve two purposes: to assist in deciding how to simplify nature without losing its essential features, and to lead to the eventual merger of the two types of models.

To summarize, a synoptic model should be:

(1) a simplification of nature, retaining those features which are essential for a forecast of nature;

(2) based on dynamic principles and models; and

(3) treated as a prototype, in a state of continuous change and improvement, until the merger with the dynamic models is completed.

Bergeron's philosophy[4] regarding synoptic models at the time he consolidated his occlusion models is summarized in the following quotation ". . . there are only two main kinds of tropospheric structures or 'models': Air Masses and Fronts. All other models can be regarded as special cases of the above-mentioned ones, taking into account that both kinds of main models may become laminar, that a horizontal temperature gradient may also exist within an air mass – though an evenly distributed one, not exceeding a certain limit – and that a frontal surface may become diffuse, quasi-horizontal or deformed. All these secondary models will act dynamically and thermodynamically in principle like the main models, and the study can thus for the sake of brevity be restricted to the latter." Such a view as this implies rather severe assumptions regarding nature or a modification of the concept of models stated by Hertz and discussed by Godske.[2]

Sutcliffe[5] emphases the failure, in practice, to restrict the use of models to those cases in which they apply. For instance, the Bergeron model for an active, intense occlusion cannot be applied to a weak or inactive system. He further discusses the failure to restrict models to a unique definition. Having defined a front on the basis of the thermal field, one cannot assume that fronts fitting this definition will have similar weather. A serious danger is seen by Sutcliffe in the use of models in place of a careful examination of all the data.

Sutcliffe points out the value of models as tools for describing the complex atmosphere, particularly in the communication of ideas. When nature is adequately described by a model, then the model sequence of events can often be used to great advantage in forecasting. It is not that models are inaccurate; it is their improper use and over use that Sutcliffe criticizes.

3. COLLECTION, REDUCTION, AND USEFULNESS OF THE DATA

3.1 Radar Program

A vertically-directed APQ-39 radar was used to investigate the precipitation structure of storms, particularly occlusions, in western Washington. This radar operates at 1.87 cm and detects only precipitation. The radar echoes for over 100 fronts were recorded on 35-mm film in a time-height display during a twenty-three month period. The radar data were transferred to time sections for comparison with hourly surface observations, precipitation rates, isotherms, and fronts. Synoptic surface and constant pressure charts were used extensively in preparing the frontal analyses.

The radar data depict the precipitation patterns in a time section (Figure 7, p. 43). The location in time and height, the relative concentration and (qualitatively) the intensity of the precipitation can be determined. The information is qualitative in the sense that the set has not been calibrated. While it may appear unfortunate that quantitative data are not obtained (for the purpose of comparing precipitation regimes of a large number of storms) the qualitative data are sufficient and considerably easier to obtain. Microscale cloud and precipitation physics problems cannot be studied, but the mesoscale and synoptic features are well depicted and easily studied.

Attenuation is of little importance because the targets are all within 30,000 feet. Heavy precipitation up to 15,000 or 20,000 feet will obscure higher weak echoes, but with Seattle's predominantly light precipitation, this situation is rare. Computations (based on radar equations, Ref [27] and cloud properties, Ref [28]) show that the power return would be attenuated about 10% by 10,000 feet of thick strato-cumulus with light to moderate precipitation and 42% by 20,000 feet of cumulus congestus with moderate precipitation rates. These percentages correspond to about a 7% and 28% deviation, respectively, between true and apparent precipitation concentrations.

The echoes are interpreted as indicating precipitation rather than clouds. Quantitative estimates as well as experience showed that heavy strato-cumulus as well as ice clouds are not recorded, but drizzle and thick precipitating cirrus decks are detected.

A subjective echo classification system has been developed to assist in the correlation of precipitation features and synoptic structures.[29] The radar film is divided into periods during which the overall echo patterns vary little. These periods range from fifteen minutes to several hours in length. Each period is classified as to extent of echoes (L, M, or H), degree of convectivity (1, 2, or 3), and characteristics (B, S, etc.). Table 1 lists the meaning of these indicators.

The subjective classification of the data in Figure 7 is indicated in Figure B-2 between the time scale and the 1000-mb level. Unfortunately some weak echoes appearing in the original film do not appear on the prints in Figure 7.

TABLE 1. List of echo-type indicators

Indicator	Meaning
0	No precipitation echoes are present
1	At least 70% of the precipitation echoes are of the stable type.
2	Between 15% and 70% of the precipitation echoes are of the stable type.
3	At least 85% of the precipitation echoes are of the convective type.
L	Precipitation echoes are observed at or below 8,000 feet.
M	Precipitation echoes are observed between 8,000 feet and 18,000 feet.
H	Precipitation echoes are observed at or above 18,000 feet.
L-, M-, or H-	Precipitation echoes are observed within the appropriate height interval, but less than one-half of the time.
X	Film is temporarily unreliable due to mechanical difficulties.
A	An angel appeared within the film interval.
G	Generating cells or levels are indicated
B	Precipitation echoes are arranged in layers or semi-horizontal bands or a band not reaching the ground.
S	Precipitation echoes are sloping, or non-horizontal streaks appear, possibly within main bodies of echoes.
W	Precipitation echoes appear in air with above freezing temperatures and no apparent precipitation or seeding is occurring from below freezing temperature regions.
T	Precipitation echoes occur simultaneously with hail, lightning, or thunder as determined from surface observations.

Convectivity is judged on the basis of variability and the texture of the echo edges. Erratic variations and sharp echo boundaries imply large variations in atmospheric motions and/or humidity. However, the most convective situations have a percentage of 'stable'-appearing echo boundaries where the convection has been capped and the clouds have been spread out horizontally. Periods of stable echoes without any imbedded convection either at the top or at the base of the layer are rare. Regions of rapid evaporation are revealed clearly by the 'stalactite'

structure of the echoes due to the small scale convection cells established by the evaporative cooling.[30]

The interpretation of the precipitation structures in terms of physical processes is obvious in some cases and impossible in others. A stable precipitation producing layer with or without evaporation at its base is clearly defined, as are convective protrusions from the tops of stable layers. Isolated showers are also apparent. The rate of lowering of a precipitation base or top depends on horizontal advection, vertical advection, precipitation fall velocity, and growth or evaporation. Only in exceptional situations – which allow assumptions as to the horizontal variations, growth rates, and terminal velocities – can the individual factors be evaluated with vertical radar and radiosonde data alone.

The majority of precipitation records contain a large amount of variability implying a considerable horizontal inhomogeneity in the precipitation field. Reasons for this variability are discussed at length in Section 6.2. The effects of topography, horizontal moisture and stability irregularities, mesoscale circulations, and glaciation induced by natural seeding from higher clouds all combine to produce the observed variability in the precipitation structure. The topography of the region is shown in Figure 1. The task of interpreting many of these fluctuations in terms of specific processes is impossible. PPI (quasi-horizontal section) or RHI (vertical cross section) radars are needed to deduce horizontal variations which would permit the proper interpretation of THI (time section)-echo slopes.

3.2 Serial Ascent Program

Frequent radiosonde observations were taken during special periods to determine the mesoscale thermal, moisture, and wind structure of occlusions for which the precipitation structure was continually recorded by vertically-directed radar. The serial ascent program was designed to clarify complexities which arose during comparison of radar data with synoptic observations. The synoptic data were frequently ambiguous with regard to the location and structure of fronts. The changes in precipitation structure were not found to correspond well with apparent frontal location. It appeared as though the mesoscale structure of fronts was much more complex than the classical models suggest.

Serial ascents were conducted during five periods, and the detailed but preliminary analyses of the selected storms (based on continuous radar records and short-interval serial ascents) were published in five volumes,[31,32,33,34,35] which will hereafter be referred to as the analysis reports. The frontal systems in the first and last cases were not occluded, and these two cases will not be presented in this report. The remaining three cases include the five occlusions to be presented and discussed in Section 4. The series of soundings include the routine and special soundings taken by the Weather Bureau at the

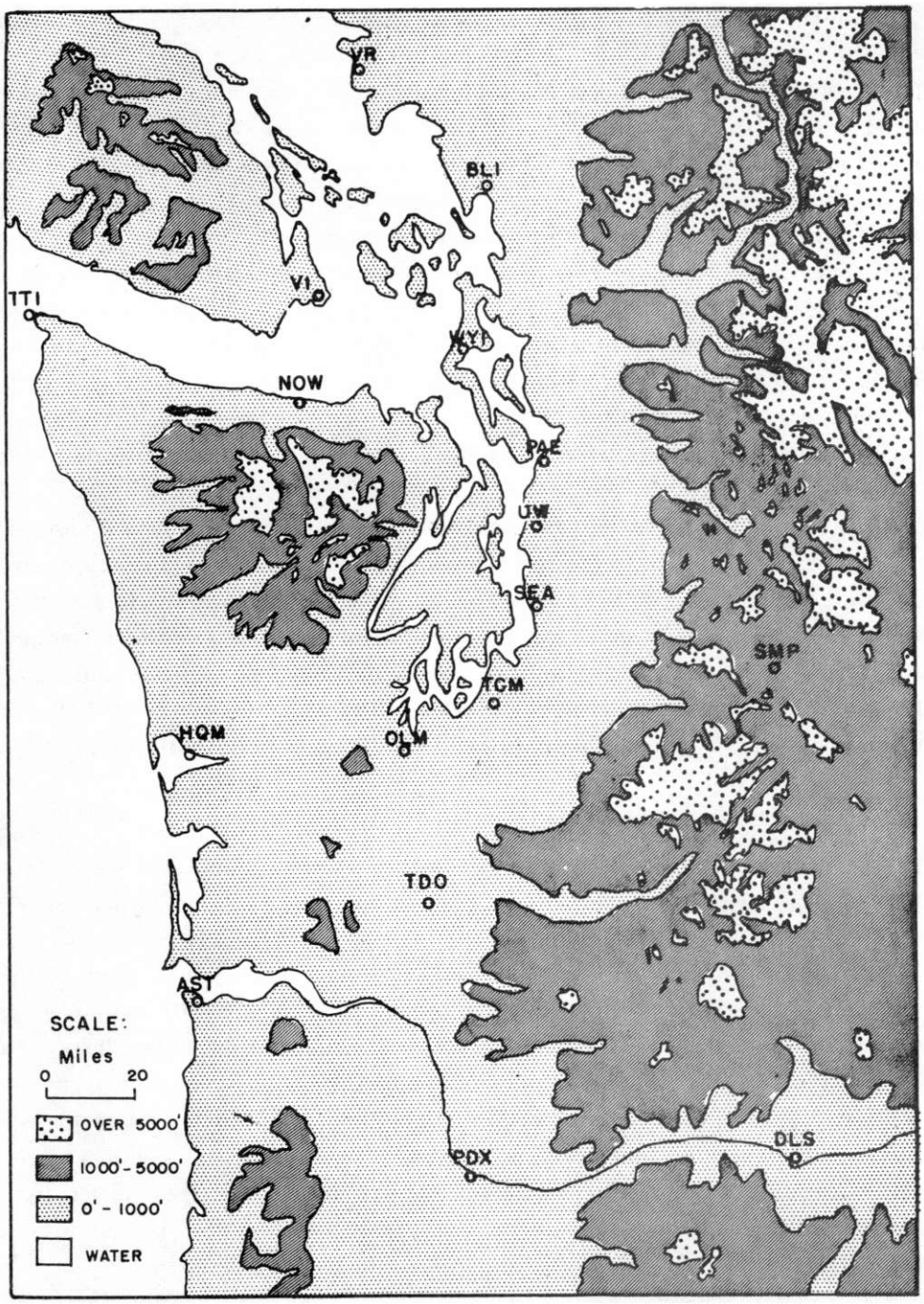

Figure 1. Topographical Map of Western Washington with Locations of Selected Stations: University of Washington (UW), Seattle-Tacoma Airport (SEA), Paine Field, Everett (PAE), McChord Field, Tacoma (TCM)

Seattle-Tacoma Airport (SEA), fifteen miles south of the University of Washington (UW). The SEA soundings were at least six hours apart, but the supplementary soundings taken at UW were as frequent as once per hour.

The data from soundings taken at the University of Washington are entered on punched cards at 30-second intervals of balloon ascent time. For soundings taken at SEA, the temperature and humidity at each level given in the data blocks on the Adiabatic Chart, WBAN-31, and all the time-elevation-azimuth, and pressure-time data on the Winds Aloft Computation Sheet, WBAN-20, are entered on punched cards. The following parameters have been computed at each 30-second interval for UW soundings and at 1-minute intervals for SEA data: pressure (p), relative humidity and saturated vapor pressure with respect to water (Rh, e_s) and ice (Rhi, e_{si}), actual vapor pressure (e), actual and saturated mixing ratio (m, m_s), centigrade, Kelvin, dew-point, virtual, and potential temperatures, (TC, TK, TD, TV, θ), horizontal winds ($\vec{V}_H$), geopotential heights (z), static energy (σ), balloon ascent rates for two, eight, and sixteen minute averages (WB2, WB8, WB16). The following quantities are listed for each sounding in the analysis reports: p, Rh, TC, TD, z, $\vec{V}_H$.

The saturated vapor pressures, e_s and e_{si}, were computed using formulas from List.[36] The quantities e and m were defined as $Rh \times e_s/100$ and $Rh \times m_s/100$, while Rhi was defined as $100 \times e/e_{si}$. The static energy is computed from the equation

$$\sigma \equiv gz + c_{pd}(TC + 73.16) + L_0 m$$

and will be discussed in detail at the end of this chapter. The balloon ascent rates and their deviations were obtained directly from the heights. It is hoped that these data will be used at a future time to infer information on eddy vertical velocities of either the air or the balloon once it is determined how to distinguish between the two factors.[37, 38]

For each of the seventeen 50-mb deep layers between 1000 and 150 mb, the following quantities were computed: temperature and height at the base of the layer (TCB, ZB), the 50-mb average* values of TC, θ, σ, Rh, Rhi, m, m_s, $m_d \equiv m_s - m$, $\vec{V}_H$, WE8, and WE16. Additional values computed for each 50-mb layer include: actual lapse rate, γ, pseudo-adiabatic lapse rate, γ_s, the dry and moist lapse rate deficits, $S_d \equiv \gamma_d - \gamma$, $S_s \equiv \gamma_s - \gamma$, the condensate production in the layer per 10 cm/sec vertical velocity, PRC, and the advective temperature change

---

*Averages were defined by the equation: $\overline{\chi} \equiv \dfrac{\int \chi \, d\left(p^{0.288}\right)}{\int d\left(p^{0.288}\right)}$

as estimated from the hodograph, ADV. Equation (A-9) from Appendix A was used to compute ADV.

The condensation rate per unit area, unit pressure thickness, and unit vertical velocity is

$$PRC = - \frac{1}{w\ \delta A\ (-\delta p)} \frac{d}{dt} \left(\rho_{sv}\ \delta A\ \delta z \right),$$

where ρ_{sv} is the density of the saturated vapor. Since the mass of the dry air is conserved and $m_s = \rho_{sv}/\rho_d$,

$$PRC = \frac{\rho_d}{w} \frac{d m_s}{dt} \frac{\delta z}{\delta p} + \frac{m_s}{w\ \delta A\ \delta p} \frac{d}{dt} (\rho_d\ \delta A\ \delta z)$$

$$= - \frac{1}{g} \frac{d m_s}{dz} .$$

The variation of saturated mixing ratio with height for the pseudo-adiabatic process can be written (see Ref. [39], p. 51)

$$\frac{d m_s}{dz} = \left(\frac{1+m_s}{L} \right) \left(c_{pm} \gamma_s - g \right) = \frac{c_{pm}(1+m_s)}{L} (\gamma_s - \gamma_d)$$

$$\therefore \quad PRC = \frac{c_{pm}(1+m_s)}{gL} (\gamma_d - \gamma_s) .$$

This equation was used to compute condensation rates for the 50-mb layers (δp = -50 mb) in units of hundredths of an inch of water per hour per 10 cm/sec vertical velocity. These values could then be used to compare precipitation rates and vertical velocities.

The synoptic surface, 850-mb, 700-mb, 500-mb, and 250-mb charts for the appropriate area and period have been plotted and analyzed along with the hourly charts for the region around western Washington. The soundings, hodographs, Rossby diagrams, time sections, and traces of surface pressure, 500-mb height, surface, 850-mb, 700-mb, and 500-mb temperatures have all been prepared. Except for the hodographs and Rossby diagrams, these charts have all been published in the analysis reports along with prints of the radar film covering the serial ascent periods. Sketches of the radar echoes on the time sections have been published in the final report[40] on the Radar Data Studies Project.

The time sections have been analyzed for: temperature, fronts, radar echoes, clouds, static energy, relative humidity with respect to ice, vertical motion, advective temperature change as estimated from hodograph, wind speed, and wind direction. The static energy, cloud, front, and vertical velocity analyses on the time sections for five frontal systems will be presented and discussed in Section 4. Appendix B contains the surface charts, 500-mb charts, and time sections for these same systems, which were originally published in the analysis reports.

3.3 Single-station Vertical Velocities

A series of radiosonde observations from a single station provides sufficient information to deduce the vertical-motion field on a time section subject to certain approximations and limitations. The technique involves a variation of the 'adiabatic method' and has been applied to compute large-scale vertical velocities from soundings at synoptic intervals.[41] With the short-sounding interval during the serial ascents, mesoscale vertical motions can be computed. Many difficulties arise in the application of this technique, but with the use of elaborate procedures made possible and practical by the use of the IBM 709, these difficulties can be minimized. The remaining problems can be treated qualitatively.

The principal features of the mesoscale vertical motions can be determined, but uncertainty does remain in the magnitude of the individual values. By computing the uncertainty of each velocity, one is able to perform an analysis of the vertical-motion field giving greater weight to the more reliable values while correcting qualitatively for those factors which cannot be computed. So little is known about mesoscale vertical-motion patterns that even qualitatively correct patterns are of great value.

3.3.1 FORMULATION OF EQUATION

The vertical velocity can be expressed by the following equation:

$$
\begin{aligned}
w = \Bigg\{ & \underbrace{-\frac{\partial T}{\partial t}}_{(1)} + \underbrace{\mathrm{ADV}}_{(2)} \underbrace{\frac{\vec{V}\cdot\vec{V}_g}{V^2}}_{(2')} + \underbrace{\mathrm{ACC}}_{(3)} + \underbrace{\frac{TV}{g}\frac{\partial}{\partial z}\left(\frac{\partial V}{\partial t} + \vec{V}\cdot\vec{\nabla}_z V\right)}_{(4)} \\
& + \underbrace{\frac{f}{g}\frac{\partial T}{\partial z}\vec{V}_H\cdot\vec{V}_g\times\vec{k}}_{(5)} - \underbrace{\frac{TV}{g}\left[\vec{t}\left(\frac{\partial^2}{\partial z^2} K_m \frac{\partial \vec{V}_H}{\partial z}\right)\right.}_{(6)} \\
& \left. + \vec{n}\cdot\frac{\partial\phi}{\partial z}\frac{\partial}{\partial z}\left(K_m\frac{\partial\vec{V}_H}{\partial z}\right)\right] + \underbrace{\left.\frac{dT}{dt}\right|_D}_{(7)}\Bigg\}\underbrace{\left\{\Gamma - \gamma\right\}^{-1}}_{(8)} \qquad (1)
\end{aligned}
$$

This equation results from an expansion of dT/dt in which $-\vec{V}\cdot\vec{\nabla}_z T$ is eliminated by using the thermal wind equation. Equation (1) is a combination of equations (A-1), (A-5), (A-7), and (A-9) of Appendix A. This appendix, which is summarized below, describes the techniques used to compute the vertical velocity and its reliability.

The vertical velocities to be computed will be averages over 50 mb and several hours. The uncertainties in the numerator and denominator of Eq. (1) will be on the order of 0.4°C/hour and 0.5°C/km, respectively, and any of the terms (1) through (7), which when properly averaged will remain less than 0.2°C/hour, can be neglected. The meaning and method of computing the terms in Equation (1) will now be discussed.

Term (1), the local temperature change, was computed from temperatures observed by three consecutive soundings using the three-point finite difference derivative (see Equation A-11).

Term (2), the advective temperature change if the ageostrophic wind is constant with height, is modified by the factor (2'), which contains the effect of a change with height of the ageostrophic wind direction. Lacking adequate knowledge of the geostrophic wind, (2') was taken to be unity in the computations. The effect of this simplification can be treated qualitatively in the analysis by observing that the advective temperature change will be overestimated (underestimated) in a trough (ridge) for gradient flow. Under supergeostrophic decelerating flow, the advective temperature change will be overestimated. For subgeostrophic, accelerating flow, important near fronts, the value of $\frac{\vec{V}\cdot\vec{V}_g}{V^2}$ will deviate little from unity, the value assumed.

Terms (3) and (4) contain the effects of a vertical variation in the speed acceleration. Term (3) includes accelerations resulting from vertical displacements into regions of different velocities. Term (4) includes that portion $\frac{\partial}{\partial z}\frac{dV}{dt}$ associated with horizontal displacements. This quantity cannot be evaluated entirely, due to the horizontal advection term, and has been omitted. On an order-of-magnitude basis this term appears to be negligible at all times while term (3) can be very important in regions of large shear.

Term (5) represents the difference between $\vec{V}\cdot\vec{\nabla}_z T$ and $\vec{V}\cdot\vec{\nabla}_p T$. For geostrophic flow this term vanishes, and for reasonable ageostrophic components the term is negligibly small. Since the ageostrophic wind cannot be adequately evaluated, this term is neglected entirely.

Term (6) represents the contribution of viscous forces to the variation of the ageostrophic wind with height. This quantity can be expected to be important wherever large wind shears and rapid eddy diffusion of momentum are found. Unfortunately, slight inaccuracies in wind observations produce relatively large

inaccuracies in this term. Even more difficult is the specification of the coefficient of eddy momentum flux as a function of height. This term has been omitted in the computations, invalidating the vertical motions computed for the lowest few thousand feet. At higher levels the effects of viscosity in varying the ageostrophic wind with height must be considered qualitatively. Only in special cases would one expect this effect to be important at high levels.

Term (7) contains the effect of diabatic processes (processes not including either adiabatic or pseudo-adiabatic ascent) in changing temperature. When compared with the residual uncertainty in the numerator, the diabatic effects, other than evaporational cooling, are negligible. Evaporational cooling can be very important, but it is difficult to include automatically during data processing. This effect must be included qualitatively wherever it occurs.

Factor (8), the denominator, represents the cooling at a level per unit vertical displacement of parcels through the level. The term Γ is the adiabatic lapse rate, pseudo-adiabatic where necessary. The pseudo-adiabatic lapse rate was used if three conditions were met: the relative humidity with respect to ice was at least 90%, the lapse rate was absolutely stable, and the vertical velocity was positive when the pseudo-adiabatic process was assumed. The critical humidity is somewhat arbitrary and is based on the fact that the humidity observations usually underestimate high relative-humidity values but by an undeterminable amount. The 90%-for-ice criteria appears to be satisfactory, but infallibility cannot be expected. If the pseudo-adiabatic process were specified while the stability were conditional or less, then the denominator would be negative and the vertical motion would probably be of the wrong sign. While pseudo-adiabatic descent can occur, until the available liquid and solid water content has been evaporated, all descent has been specified as dry adiabatic. In those few cases in which pseudo-adiabatic descent was occurring, the specification of the dry process will only cause an error in the magnitude of the subsidence.

With the approximations and assumptions indicated above, Equation (1) reduces to

$$w = \frac{-\frac{\partial T}{\partial t} + ADV + ACC}{\Gamma - \gamma} \quad . \tag{2}$$

When using this equation, qualitative corrections should be included for omission of the factor (2') and the viscosity and diabatic terms (6) and (7) in Equation (1). The viscosity term is nearly impossible to handle satisfactorily, even qualitatively. Aloft this term should be negligible except where the viscous forces appear to vary rapidly with height. In the lowest 3,000 feet and where evaporational cooling is strong. Equation (2) is of little value since qualitative corrections are inadequate.

3.3.2 COMPUTATION OF VERTICAL VELOCITIES

Equation (2) is a differential equation in w but the acceleration term, ACC, is often negligible. The differential equation can be solved approximately as a first order differential equation with constant (averaged) coefficients. The solution can then be written

$$w_1 = w_o \, e^{\alpha} + \beta (e^{\alpha} - 1) , \tag{3}$$

where the coefficients are the average values between the levels and are defined by

$$\alpha \equiv - \frac{\Delta z \left(\frac{TV}{g} \frac{\partial^2 V}{\partial z^2} - \Gamma + \gamma \right)}{\frac{TV}{g} \frac{\partial V}{\partial z}}$$

$$\beta \equiv \frac{- \frac{\partial T}{\partial t} + ADV}{\frac{TV}{g} \frac{\partial^2 V}{\partial z^2} - \Gamma + \gamma} .$$

Unfortunately Eq. (3) is not sufficiently stable with respect to observational uncertainties in the coefficients α and β. We cannot merely specify boundary conditions and integrate throughout the troposphere without introducing excessive errors due to observational errors in the coefficients.

To overcome the difficulties imposed by the instability of Eq. (3) for successive integrations, the acceleration term in Eq. (2) was disregarded while a first approximation to the vertical velocity field was computed from the simple expression

$$w = \frac{- \frac{\partial T}{\partial t} + ADV}{\Gamma - \gamma} \tag{4}$$

Equation (4) is solved for each 50-mb layer from 1000 to 150 mb. The quantities on the right side have been averaged over the 50-mb thickness for each sounding and $\partial T / \partial t$ is the three-point finite difference derivative centered at sounding time but utilizing data from the preceding and following soundings. The pseudo-adiabatic lapse rate is used for Γ only if the relative humidity with respect to ice equals or exceeds 90%, γ is absolutely stable, and a positive w is obtained. Once the w-values have been checked for reliability and replaced by

vertical interpolation where necessary, a horizontal smoothing is performed. A three-point running-mean is computed using the values from three consecutive soundings at the same level. This horizontal smoothing is consistent with the horizontal smoothing inherent in the computation of the local temperature change.

With the running-mean averages of the velocities from Eq. (4) as boundary conditions for each 50-mb layer, Eq. (3) is used to integrate between the 50-mb layers to see if the approximate vertical-motion field is consistent with the more complete equation. For example, with approximate w -values at 550mb and 450 mb, one can integrate up and down 50 mb to obtain two values, w_U and w_D, for the 500-mb level. These values can then be compared with the first approximation at 500 mb, w_0 . A second approximation to the 500-mb vertical velocity, w_1, can be defined as

$$w_1 = \frac{w_0 + \frac{w_U + w_D}{2}}{2} \tag{5}$$

A set of second approximations can be computed and used as boundary conditions for computation of the third approximation, etc. Hopefully, after a certain number of repetitions of this procedure, the successive approximations will converge to values consistent with Eq. (2).

In practice, convergence did not occur; rather the successive approximations became unstable. This failure is due in part to the approximations invoked in the derivation of Equations (2) and (3). Errors due to either the approximations or inaccurate observations could prevent convergence. Perhaps a better numerical solution of Eq. (2) could be developed which would reduce the instability.

The use of Eq. (3) to correct the approximate values obtained from Eq. (4) was not without value even if it was only a qualified success. By scanning the integrated values as compared to the approximate values, one could readily distinguish between those regions in which the acceleration effect was negligible and where it was important. Where it was important, one could estimate both the sign and, roughly, the magnitude of the error in the original estimate. It was thus possible to correct the analysis based on vertical velocities from Eq. (4) to include, 'semi-quantitatively,' the effect of the acceleration term. Without this correction unrealistically large vertical gradients of w had been indicated, implying large values of horizontal divergence.

3.3.3 COMPUTATION OF UNCERTAINTY OF VERTICAL VELOCITIES

The uncertainty of the vertical velocity depends upon the uncertainty of the observations and, to a large extent, upon the magnitude of the various terms in Eq. (4).

Having specified the observational uncertainty under average conditions, the uncertainty of each vertical velocity value can be determined. Whenever the uncertainty in a value is found to exceed both 3 cm/sec and the magnitude of that velocity, that velocity is disregarded and a new velocity and uncertainty are computed by vertical interpolation between the nearest reliable levels. If the value at the lowest or highest level is unreliable, the velocity is set to zero and the uncertainty is set to 3 cm/sec.

The uncertainty corresponding to the running-mean vertical velocity is also computed. The quality of the resulting vertical velocity is then evaluated depending on the magnitude of the uncertainty relative to the magnitude of the velocity. The criteria are as follows:

Good: $\delta\bar{w} < |\bar{w}| / 2$

Fair: $|\bar{w}| / 2 \leq \delta\bar{w} \leq |\bar{w}|$

Close: $|\bar{w}| < \delta\bar{w} \leq 3$ cm/sec

Bad: $\delta\bar{w} > |\bar{w}|$ and $\delta\bar{w} > 3$ cm/sec

Table 2 lists the percent of vertical velocities in certain classes, by layers, on the basis of forty-six soundings. This table indicates the reliability of the mean vertical velocities (Col. 1 - 4); and for those values which are not 'Bad,' the frequency of vertical interpolations (Col. 5), saturation* with conditional instability (Col. 6), saturation with subsidence (Col. 7), and significant inconsistency between values given by Eq. (4) and Eq. (3) (Col. 8).

It can be seen that the least reliability is in the region from 600 mb to 400 mb but that the maximum percentage of bad values is 22%. Enough reliable values are available for a satisfactory analysis. The values which showed significant inconsistencies when the acceleration term was included could be semi-quantitatively corrected to the extent of making a positive contribution to the analysis. Where vertical interpolation had been performed and where bad quality values were computed, the resulting analysis must be interpreted as representing a larger averaging interval, just as analyses of upper air charts in regions of relatively sparse data represent more averaging. Table 2 does not include data on uncertainties due to viscous stresses and evaporation. Were these factors to be considered, the values up to 850 mb would be of poorer quality than Table 2 indicates.

* Saturation is defined as a relative humidity with respect to ice of at least 90%.

TABLE 2. Percent of vertical velocities in certain classes. The 'Bad' values were excluded in the computation of the percentages in columns (5) through (8).

Layer (mb)	Quality of $\overline{w}$				Vert. Int.	Sat. Unst.	Sat. Neg.	Acc. Incon.
	Good	Fair	Close	Bad				
	1	2	3	4	5	6	7	8
950-900	65	20	9	7	9	5	0	28
900-850	78	11	0	11	12	12	0	10
850-800	76	17	7	0	15	15	4	22
800-750	59	24	11	7	12	21	5	16
750-700	52	30	9	9	7	19	0	33
700-650	52	39	7	2	7	18	9	36
650-600	63	17	9	11	10	5	7	29
600-550	33	26	20	22	17	6	22	25
550-500	35	30	13	22	17	11	11	8
500-450	43	37	7	13	12	7	12	38
450-400	15	52	11	22	17	22	19	22
400-350	39	41	2	17	29	11	18	32
350-300	39	39	4	17	18	8	5	34
300-250	52	22	17	9	2	0	2	31
250-200	63	26	9	2	4	0	0	11
AVERAGE	51	29	9	11	13	11	8	25

3. 3. 4 DISCUSSION

The rather elaborate techniques devised to objectively compute the vertical motions, select the proper adiabatic lapse rate, compute the uncertainties, correct unreliable values before performing the horizontal smoothing, and list the quality of the result performed very satisfactorily. That the single-station vertical velocity computations are capable of depicting roughly the characteristics of the mesoscale vertical motions is sufficient to justify the elaborate computation techniques. The number of manipulations necessary to arrive at these properly averaged quantities makes it virtually essential that computers be utilized. Round-off and human errors would be compounded if such computations were performed manually.

This procedure does not produce vertical velocities for either the first or last soundings in a series, for the local temperature change is unknown there. The horizontal averaging cannot be performed for either the first or last two soundings. Variation in the sounding frequency will affect only the interval over which the vertical velocities have been averaged. However, for soundings at much shorter or longer intervals than a few hours, a difference may occur in the relative magnitude of the terms in Eq. (1). The technique discussed herein is designed for sounding intervals of a few hours.

A consistency check was made to see that the precipitation to be expected (from the PRC values and the analyzed w-field) agreed with the observed precipitation. The agreement was inconclusive. The effects of cloud storage, entrainment, and evaporation can account for the deficit of precipitation observed at the ground over the precipitation computed to have formed. In fact, the uncertainties in this consistency check were too large for this test to prove or disprove the vertical-velocity fields, but the comparison did show that the vertical velocities were plausible.

Subjectivity must be introduced in the final analysis of the field, for it is at this stage that qualitative allowance is made for acceleration consistency, the factor $\left(\frac{\vec{V}\cdot\vec{V}_g}{V^2}\right)$, evaporational cooling, viscous stresses, and the relative reliability of the computed velocities. There appears to be no substitute for a careful but subjective analysis considering those factors which cannot be treated by the computer. Independent indications of vertical motions, such as the nature of the radar echoes and the observed precipitation rate, were also used in the subjective analysis.

All factors considered, it appears that the principal features of the vertical-velocity analyses are correct. Large cells of rising and sinking motion are well supported while the details of their shape and magnitudes are somewhat uncertain. It is believed that the errors in magnitude are biased neither toward large nor small values. Regions with analyzed velocities of 20 cm/sec are not uncommon, but it must be remembered that while large-scale vertical velocities rarely exceed 10 cm/sec, mesoscale vertical motion on the order of meters/second can be expected in stormy regions. The need for horizontal smoothing (consistent with the local temperature-change computations) unavoidably destroys the large horizontal gradients in the vertical velocity which are present in nature.

The predominant feature of the vertical-motion fields to be presented in Section 4 is the multiplicity of cells of ascent and descent associated with frontal systems. The concepts of lifting in one air mass and subsidence in another and of a simple variation of w throughout the troposphere with peak values at a middle-tropospheric level of non-divergence may be valid on the large scale but not on the mesoscale. The complexity of frontal-precipitation patterns observed by the radar support the mesoscale vertical-velocity fields which indicate large variations in w with certain complex, but recurring, patterns.

Ideally, a study of mesoscale vertical motions would involve simultaneous serial ascents from several locations in a closely spaced (about thirty miles) pattern. A direct evaluation of the mesoscale ageostrophic winds and horizontal temperature advections would then be possible. Such a program would improve the reliability and accuracy of the vertical velocities, but it is doubtful that simple vertical-motion fields would be found.

3.4 Static Energy

The static energy will be defined as the quantity, σ , where

$$\sigma = gz + c_{pd}T + L_0 m \quad . \tag{6}$$

This quantity was introduced by Kiefer[42] and is discussed briefly by Beers[43]. The static energy expresses the energy of a unit mass of air at rest. The terms in σ are: gravitational potential energy, enthalpy of the dry air, and 'latent heat potential energy' (that portion of the water vapor enthalpy which will be given to the parcel during pseudo-adiabatic condensation). The static energy will be shown to be quasi-conservative for condensation and evaporation processes as well as vertical displacements. The quantity will vary slowly under the influence of diabatic processes. Potential (or convective) instability is indicated by a decrease of σ with height.

The equation of motion, neglecting friction, can be operated on by $\left[\vec{V}\right]$ giving

$$\frac{d}{dt}\frac{V^2}{2} = -\frac{1}{\rho}\vec{V}\cdot\vec{\nabla}p - wg = -\frac{1}{\rho}\frac{dp}{dt} + \frac{1}{\rho}\frac{\partial p}{\partial t} - \frac{d}{dt}(gz) \quad . \tag{7}$$

The thermodynamic energy equation can be written

$$\frac{dq}{dt} - \frac{L}{1+m}\frac{dm}{dt} = c_{pm}\frac{dT}{dt} - \frac{1}{\rho}\frac{dp}{dt} \quad . \tag{8}$$

Except for the dq/dt term, Eq. (8) is the pseudo-adiabatic energy equation (Ref. 39 , p. 31) which can be derived from either an energy or entropy balance condition. Hence, dq/dt must include all diabatic effects omitted in the pseudo-adiabatic model.

Elimination of dp/dt between Eq. (7) and Eq. (8) leaves

$$\frac{d}{dt}\left(\frac{V^2}{2} + gz\right) = \frac{1}{\rho}\frac{\partial p}{\partial t} + \frac{dq}{dt} - \frac{L}{1+m}\frac{dm}{dt} - c_{pm}\frac{dT}{dt} \quad . \tag{9}$$

To an excellent approximation,*

$$c_{pm} = c_{pd}(1 + 0.8\,m) = 1.005\,(1 + 0.8\,m)\ \mathrm{j/g/^\circ K} \quad ,$$

*The constants in this section are valid when the energy is in joules.

and

$$L = \left[2500 - 2.4\,T\ (°C)\right] \equiv \left[L_0 - 2.4\,T\ (°C)\right]\ j/g\ .$$

Therefore,

$$-\frac{L}{1+m}\frac{dm}{dt} = -\frac{d}{dt}(L_0 m) + \frac{L_0 m + 2.4\,T\ (°C)}{L_0(1+m)}\frac{d}{dt}(L_0 m)\ ,$$

and

$$-c_{pm}\frac{dT}{dt} = -\frac{d}{dt}(c_{pd}T) - 0.8\,c_{pd}m\frac{dT}{dt}\ .$$

Equation (9) can be rewritten using Eq. (6) as

$$\frac{d}{dt}\left(\frac{V^2}{2} + \sigma\right) - \frac{dq}{dt} = \psi\ , \tag{10}$$

where ψ consists of several small terms, namely

$$\psi \equiv \frac{1}{\rho}\frac{\partial p}{\partial t} - 0.8\,c_{pd}\,m\frac{dT}{dt} + \frac{L_0 m + 2.4\,T\ (°C)}{L_0(1+m)}\frac{d}{dt}(L_0 m)\ .$$

An example will be given to illustrate the probable magnitude of ψ as compared to the observational uncertainty of σ. Consider the ascent of saturated air from 900 mb at 7°C to 500 mb at 20 cm/sec with a local pressure change of -1 mb/hr.

$$\psi\,\Delta t = \frac{1}{\rho}\frac{\widetilde{\partial p}}{\partial t}\frac{\Delta z}{w} - 0.8\,c_{pd}\,\overline{m}\,\Delta T + \frac{L_0\overline{m} + 2.4\,\overline{T}\ (°C)}{1+\overline{m}}\Delta\overline{m}$$

$$\doteq \left[\left(\frac{1}{10^{-3}}\ \frac{-10^3}{3600}\ \frac{4.5\times10^5}{20}\right)\times10^{-7} - (0.8)(0.004)(-30) + (8.7 - 14.4)(0.006)\right]\ j/g$$

$$\doteq -0.625 + 0.096 - 0.034 \doteq -0.56\ .$$

This energy corresponds to a 0.56°C temperature change in a 6.25-hr period. The local pressure change dominates ψ and, for periods of many hours, the mean value in the vicinity of the parcel will usually be lower than the 1 mb/hr used in the example. The average value of ψ for a 6-hr period in a cyclonic region would be on the order of ± 0.4 j/g/6-hrs.

Therefore, upon integrating Eq. (10),

$$\sigma - \sigma_o = - \frac{V^2 - V_o^2}{2} + \Delta q \pm 0.4 \left(\frac{\text{j/g}}{\text{6-hr}} \right) \Delta t \quad . \tag{11}$$

The kinetic energy change term will be on the order of 0.4 j/g for $\Delta t \approx 6$ hours except near the jet stream where it can be 1 or 2 j/g. For long periods the diabatic term, Δq, can become dominant on the right side of Eq. (11). For periods on the order of six hours, the entire change in static energy can be expected to be on the order of $\pm$ 0.8 j/g.

The uncertainty in the observation of σ is

$$(\delta \sigma)^2 = \left(g\, \delta z + c_{pd}\, \delta T \right)^2 + \left(\frac{L_0 m_s\, \delta Rh}{100} \right)^2$$

$$\approx (0.4)^2 + \left[0.25\, m_s (\text{g/kg}) \right]^2$$

Hence, $\delta \sigma$ will range from about 0.7 j/g at lower levels to 0.5 j/g above 500 mb.

It can be concluded that for periods of about a day the static energy is conserved to within the uncertainty of its observation except in regions of very strong winds ($V \approx 100$ knots). For many tropospheric problems, σ may be treated as a conservative quantity, for jet stream studies the quantity $(V^2/2 + gz + c_p T)$ is very nearly conserved, and for long term problems, the change in static energy very nearly equals the diabatic heat added.

While not differing significantly in conservativeness from the pseudo-wet-bulb potential temperature or the equivalent potential temperature, σ is more easily interpreted physically. The computation of σ by numerical computers is straightforward, and a slide rule has been prepared which allows rapid hand computation of Eq. (6). The scales, as sketched in Figure 2, are designed so that when the slide is positioned with the temperature opposite the height of the parcel, its static energy may be read opposite the proper mixing ratio. It is the ease of interpretation of conditions and processes in terms of static energy that makes this function very useful in dealing with tropospheric processes involving condensation and evaporation.

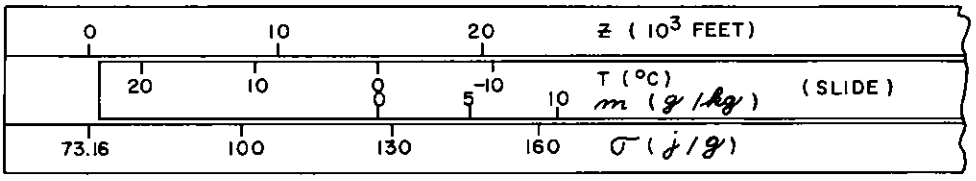

Figure 2. Sketch of the Slide Rule for Computing Static Energy

The effects on a parcel of conversions between height, moisture content, and temperature are made explicit in the terms of static energy function, and the influence of vertical motions and condensation (or evaporation) on baroclinity is readily interpreted. The contribution to σ of the various terms can be examined with the relation*

$$\sigma(j/g) \doteq 3z\ (10^3\ \text{ft}) + T\ (°C) + 2.5\ m\ (g/kg) + 73.2 \tag{12}$$

The horizontal temperature graident, so important in baroclinic theories,** can be compared with the conservative σ-field, the moisture gradients, and the contour patterns by the relations:

$$\vec{\nabla}\sigma = \left(\frac{c_p T}{\theta}\right) \vec{\nabla}\theta + L\vec{\nabla}m + g\,\vec{\nabla}_p z \tag{13a}$$

and

$$\vec{\nabla}_p\,[\sigma(j/g)] \doteq 3\,\vec{\nabla}_p\,[z\ (10^3\ \text{ft})] + 2.5\,\vec{\nabla}_p\,[m\ (g/kg)]\ . \tag{13b}$$

The static energy field can be used to distinguish between stable zones separating different air masses and subsidence-produced stable zones. The former will have strong gradients of static energy, and the latter will have a moisture gradient opposing the stable lapse rate and little σ-gradient. For such considerations the following relation is convenient:

---

*Energy bases are arbitrary, but it has been suggested[42] that an enthalpy base of zero at 200°K is most convenient and this procedure will be adopted.

**The relation of $\vec{N}$, the baroclinity vector (see Ref. [44], p. 106), to the static energy is

$$\vec{N} \equiv \vec{\nabla}\frac{1}{\rho} \times \vec{\nabla}p = \vec{\nabla}T \times c_p\vec{\nabla}(\ln\theta) = \vec{\nabla}\ln T \times (\vec{\nabla}\sigma - L_0\vec{\nabla}m - g\,\vec{\nabla}_p z)\ .$$

$$\frac{\partial \sigma}{\partial z}\left(\frac{j/g}{10^3\ ft}\right) \doteq 3 + \frac{\partial T}{\partial z}\left(\frac{°C}{10^3\ ft}\right) + 2.5\ \frac{\partial m}{\partial z}\left(\frac{g/kg}{10^3\ ft}\right) \tag{14}$$

The diabatic processes are important in establishing the large scale static energy structure of the atmosphere according to the relation

$$\frac{d\sigma}{dt} \doteq \frac{dq}{dt} \qquad \text{(for long time periods).} \tag{15}$$

Air masses warmed from below become unstable and, with thorough mixing, become nearly homogeneous in σ. Other air masses are cooled aloft and become horizontally stratified but with substantial σ-gradients. In either case, air masses are bounded by sloping zones of relatively intense σ-gradients. Radiation and mixing, over a period of time, can produce large σ-gradients within a subsidence zone. Since static energy is well conserved for periods on the order of a day, it can be used to good advantage in investigations of mesoscale mixing processes.

3.5 Effects of Mixing on the Static Energy Field

Since the total energy is not changed by mixing, the static energy, σ_m, of a mixture of M_1 grams of air at σ_1 and M_2 grams at σ_2, is the mass-weighted mean, namely

$$\sigma_m = \frac{M_1\,\sigma_1 + M_2\,\sigma_2}{M_1 + M_2}\ .$$

The diffusion of static energy can be expressed in terms of an eddy exchange coefficient, K, when σ is conserved. If the usual approximation is made that the eddy exchange coefficients of enthalpy and water vapor are identical, then this common coefficient will be identical to the K used for σ-diffusion.

Consider a surface of constant σ with a unit normal, $\vec{n}$, directed toward increasing values of σ and let n be the distance coordinate in the direction $\vec{n}$. If V_n and V_{sn} are the components of the (mean) wind and surface speeds, respectively, in the $\vec{n}$-direction, then

$$\frac{D\sigma}{Dt} \equiv \frac{\partial \sigma}{\partial t} + V_n\,\frac{\partial \sigma}{\partial n} = \frac{\partial}{\partial n}\left(K\,\frac{\partial \sigma}{\partial n}\right) \tag{16}$$

and

$$\frac{\delta\sigma}{\delta t} = \frac{\partial\sigma}{\partial t} + V_{sn}\frac{\partial\sigma}{\partial n} = 0 ; \quad \frac{\partial\sigma}{\partial t} = - V_{sn}\frac{\partial\sigma}{\partial n} , \tag{17}$$

where D/Dt is the total derivative following the mean wind and $\delta/\delta t$ is the total derivative following the surface of constant σ. Equation (16) is based on the K-theory of eddy diffusion which defines K by the condition that the eddy flux of a conservative quantity equals (-K) times the graident of that quantity.

From Equations (16) and (17) the relative velocity of the surface and the fluid, $V_r = V_{sn} - V_n$, can be expressed as

$$V_r = - \frac{1}{\frac{\partial\sigma}{\partial n}} \frac{\partial}{\partial n}\left(K \frac{\partial\sigma}{\partial n}\right) . \tag{18}$$

The rate of change of the gradient of σ following a σ-surface can be expressed, using Eq. (17), as

$$\frac{\delta}{\delta t}\left(\frac{\partial\sigma}{\partial n}\right) = \frac{\partial}{\partial t}\left(\frac{\partial\sigma}{\partial n}\right) + V_{sn}\frac{\partial}{\partial n}\left(-\frac{1}{V_{sn}}\frac{\partial\sigma}{\partial t}\right)$$

Hence,

$$\frac{\delta}{\delta t}\left(\frac{\partial\sigma}{\partial n}\right) = -\frac{\partial\sigma}{\partial n}\frac{\partial V_{sn}}{\partial n} ; \quad \frac{\partial}{\partial t}\left(\frac{\partial\sigma}{\partial n}\right) = -\frac{\partial}{\partial n}\left(V_{sn}\frac{\partial\sigma}{\partial n}\right) \tag{19}$$

From Eq. (18), one can see that σ-surfaces propagate through the fluid toward lower values of $K\frac{\partial\sigma}{\partial n}$. It can be seen from Eq. (19) that the σ-gradient increases at a σ-surface whenever $\frac{\partial V_{sn}}{\partial n}$ is negative, which can be due to divergence on a σ-surface and/or mixing effects. Consider a few examples of the effect that mixing can have on the formation (and dissolution) of $\vec{\nabla}\sigma$-zones* (see Figure 3).

Example 1: The release of potential instability from a quasi-horizontal layer. The potential instability can be initially established by subsidence aloft and the influx of moisture and possible heat from the surface. A moist surface mixing zone is capped by a 'subsidence inversion' preventing deeper mixing but allowing

* The expression '$\vec{\nabla}\sigma$-zone' will be used to mean 'a zone of relatively intense σ-gradient.'

potential instability to develop. This situation may occur in a warm subtropical high or within a subsiding and spreading cold dome. A similar situation can develop behind either an upper cold front or a warm-type occlusion. The potential instability may be released by the large-scale lifting associated with the approach of an active front or a depression.

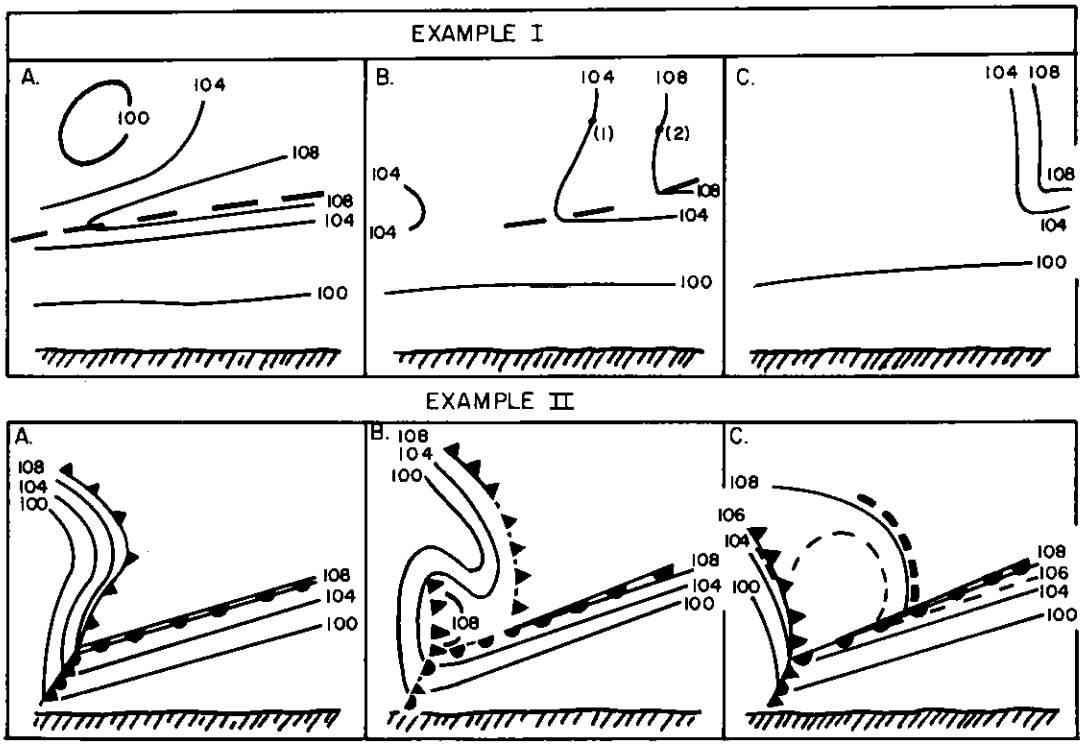

Figure 3. The σ-Field: A - Before, B - During, C - After Mixing in Two Cases

Figure 3 illustrates the changes that can occur in the σ-field as large-scale lifting (low-level convergences) raises and destabilizes the potentially unstable zone. Rapid mixing (large K) is found above the level at which the instability is formed. The very large K and, hence, large $K \frac{\partial \sigma}{\partial n}$ in the mixing zone, tends to propagate the σ-surfaces through the fluid toward regions of smaller $K \frac{\partial \sigma}{\partial n}$. Thus, large-scale lifting of the stable zone and the potentially unstable zone will result in mixing and the erosion of stable air at the base of the mixing zone.

The vertical convection and mixing will produce vertical surfaces within the mixing zone which will propagate toward lower values of $K \frac{\partial \sigma}{\partial n}$. From the

equations it can be seen that even in the absence of divergence on the σ-surfaces, the gradient of σ will increase wherever

$$\frac{\partial}{\partial n}\left[\frac{\frac{\partial}{\partial n}\left(K\,\frac{\partial \sigma}{\partial n}\right)}{\frac{\partial \sigma}{\partial n}}\right] = \frac{\partial}{\partial n}\left[K\,\frac{\partial}{\partial n}\,\ln\left(K\,\frac{\partial \sigma}{\partial n}\right)\right] > 0 \ .$$

At points (1) and (2) in Example I (B), K is increasing very rapidly toward lower σ-values so that $\frac{\partial}{\partial n}\ln\left(K\,\frac{\partial \sigma}{\partial n}\right) < 0$ at both points. Since K can be expected to be much larger at (1) than (2), $\frac{\partial}{\partial n}\left[K\,\frac{\partial}{\partial n}\,\ln\left(K\,\frac{\partial \sigma}{\partial n}\right)\right] > 0$. The σ-gradient is increasing with time between the 104 and 108 σ-surfaces.

Thus, a steep $\vec{\nabla}\sigma$-zone is formed at the edge of the mixing region. This zone will be advected with the fluid as either a drying or cooling zone depending on the vertical motion within the region which has been mixed. Such a mechanism can produce mesoscale baroclinic zones whenever potential instability is released from a quasi-horizontal layer.

Example II: The release of potential instability developed by air from behind a cold front at high levels descending and advancing ahead of the lower-level front. The cold front at high levels can precede the cold front at lower levels as long as the upper-level cooling does not reduce the stability to less than the neutral condition. The original frontal models with zero-order temperature discontinuities could only slope toward the cold air mass. Real fronts and frontal models with first order discontinuities can slope in either direction, but toward the warm air only until the stability is reduced to neutral in the transition or 'cooling' zone.

The low-level convergence ahead of the surface front can release the newly formed potential instability resulting in strong mixing ahead of the lower-level front. As the instability is being released, the σ-surfaces will propagate outward from the mixing region. As in Example I, a sloping $\vec{\nabla}\sigma$-zone will form on either side of the mixed region. The extent of the baroclinity in the σ-gradient zone depends in part upon the total σ-gradient and in part upon the moisture gradient across the $\vec{\nabla}\sigma$-zone. Continued rising motion in the mixed region can cause considerable cooling to occur with passage of the forward zone.

The above mechanism can account for pre-cold frontal cooling or drying just as can the mechanism in Example I. This mechanism can also reduce a cold-type occlusion to a weak warm-type occlusion or an upper cold front.

The serial ascent cases, which will be discussed next, provide excellent verification of the occurrence and importance of the processes depicted in these two examples. In fact, these case studies lead to the use of σ-surfaces to describe the effects of mixing on fronts.

4. CASE STUDIES

Five frontal systems which passed Seattle during three different time periods will be discussed. The serial ascent radiosonde data are combined with the vertically directed radar information to determine the mesoscale features of these systems for which synoptic-scale analyses have been prepared. The synoptic charts, radiosonde data, and radar records, as well as the time sections with winds, isotherms, fronts, and clouds for these periods, are presented in Volumes II, III, and IV of the serial ascent analysis reports.[32, 33, 34] Some additional remarks on these cases are included in the final report of the Radar Data Studies Project.[40] These reports contain much information and data pertaining to the case studies. Unless the information and data are essential to understanding the following discussion, they will not be repeated. The vertical velocity and static energy data had not been prepared or analyzed at the time of publication of the earlier reports.

Time sections through the five frontal systems are presented in Figures 4, 5 and 6. The front, cloud, vertical velocity, and static energy analyses are portrayed throughout the troposphere. The frontal positions are those presented in the earlier reports and are based primarily on the synoptic scale analyses with particular attention given to the thermal field. Appendix B contains the earlier time sections which include the plotted winds and the analyzed thermal field for these cases. The surface and 500-mb charts for eleven periods during these case studies are also presented in Appendix B.

The vertical velocities in Figures 4, 5, and 6 were computed using the single-station method as discussed in detail in Section 3.3 and Appendix A. While the magnitudes of the vertical velocity are uncertain, the general patterns are well established. The values at a point are normally based on three soundings and averaged over a 50-mb thickness. Hence, very small features, such as may show up in the data from a single sounding, have been smoothed out of the vertical-velocity field. The σ-analysis is also based on averages over 50-mb layers.

4.1 Case I: 1, 2 February 1961

Case I is a moderately well marked occlusion with warm, cold, and occluded fronts located readily on the synoptic charts (Figures B-4 and B-5) except in the lowest layers where there was some uncertainty as to the relation of the occluded front and the secondary cold front. The occluded front apparently evolved within a previously nonfrontal trough when this trough came into a position extending northward from the peak of a developing open wave.

Convective activity preceding the system is seen in Figures 4 and B-1 to be suppressed by the lowering of the stable warm frontal zone. Due to the infrequent sounding interval during this period, the vertical velocities apply to a longer term mean. Hence, the convection occurred in a region of slow mean ascent bounded by slow descent. In the cases which follow, convection also occurs in regions with infrequent soundings, and the vertical velocities are also averages over periods greater than the convection interval.

While rising motion and clouds are present above the warm front, neither the cloud base nor the w-isotachs are oriented along the frontal surface. This situation occurs frequently so that the assumption that the base of a cloud shield coincides with the warm frontal surface is unrealistic.

The cell of strong rising motion at 21Z 1 February is based on surface precipitation rates. This pre-frontal surge of heavy precipitation was evident from western Washington to the Queen Charlotte Islands. The feature was oriented parallel to and occurred six to ten hours in advance of the surface front.

Notice in Figure 4 that a zone of descending motion extends from the cold air mass, above the elevated cold front* and forward over the ascending air in the warm sector. This subsidence zone separates the middle-level ascent and middle-level clouds in the warm sector from the cirrus deck in the upper troposphere. The ascending motion associated with the high-level cirrus is centered above the cold front with values in excess of 30 cm/sec and extends forward over the warm sector with diminishing magnitudes. Convection broke out within the warm sector upon the appearance of the subsiding and intermittently dry air, a sequence discussed by Wexler and Atlas.[45]

One of the most prominent features of the vertical-motion field is the large cell of strongly rising motion which is located at middle levels after the beginning of the cooling. This zone is too large both in extent and in the magnitude of the values to be discounted as an observational error. Clouds and saturation are evident in the upper portion of this zone; while at lower levels and to either side of the maximum ascent, dry air is present. Apparently air which subsided further in the cold air mass was lifted rapidly in the transition zone behind the cold front and reached saturation again only at the higher levels in the region of strongest ascent. Subsidence is shown to occur further in the cold air after 09Z 2 February.

Notice that strong rising motion surrounds the occluded front and that final clearing did not occur at any level until after the cooling had begun. The radar echoes combined with the frequent soundings demonstrate conclusively that the cold front, defined as the warm edge of the transition or frontal zone, precedes the general clearing by one or more hours at various levels.

---

* The term 'elevated cold front' will refer to a cold front connected with an occluded front and supposedly reaching the surface further south. An 'upper cold front' will be restricted to sharp upper-level cooling not associated with a surface front.

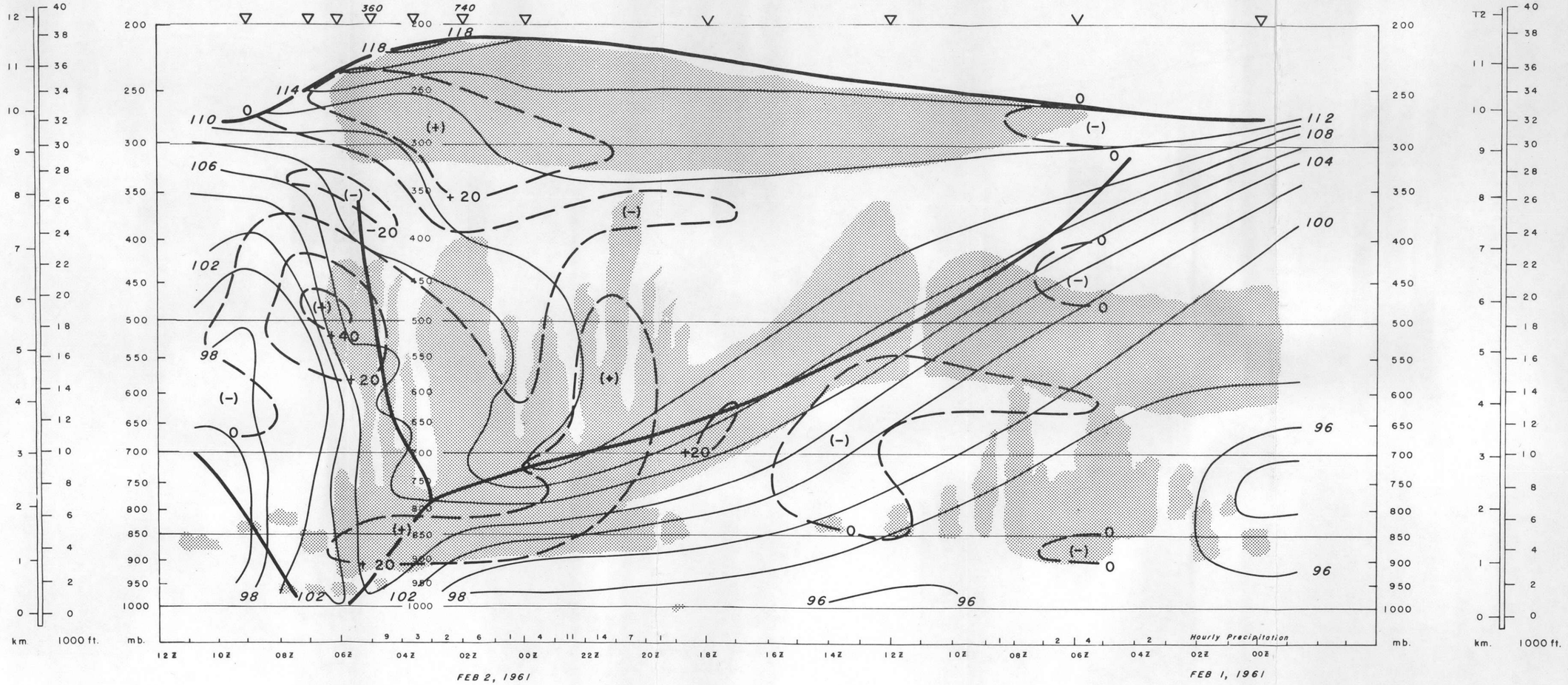

Figure 4. Time Section for Case I. Thin lines are static energy (j/g), heavy lines are frontal or tropopause discontinuities, and dashed lines are vertical velocity (cm/sec) with (+) or (-) indicating centers of vertical motion cells. Cloud areas are stippled, and precipitation rates (10^{-2} in./h) are entered along the time scale. Times of soundings and rawinsondes are indicated at 200 mb by the symbols ∇ and ∨ respectively.

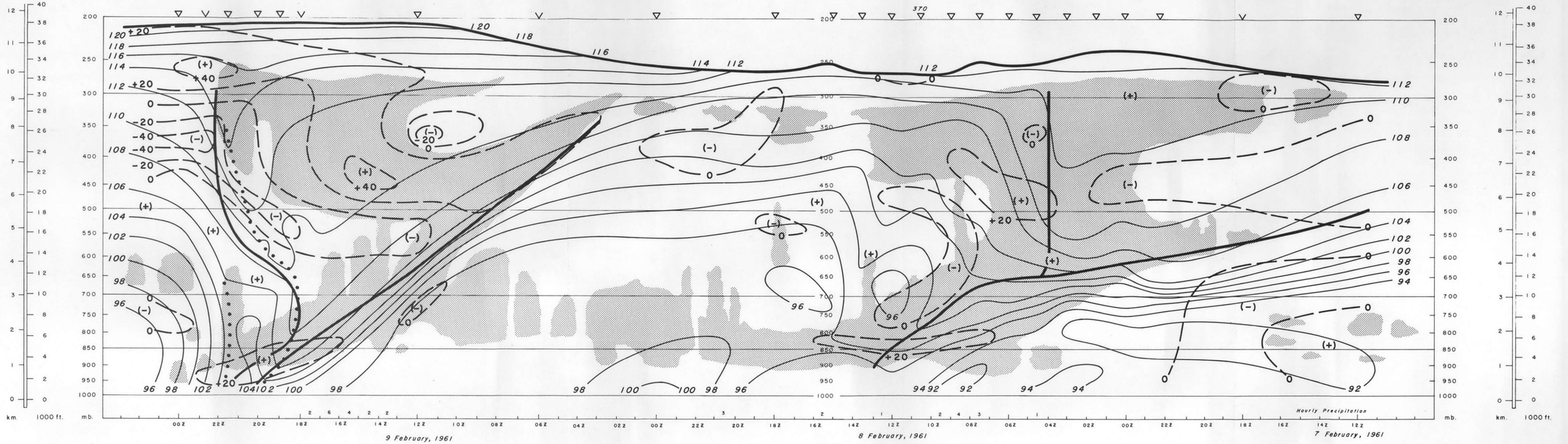

Figure 5. Time Section for Case IIA (Right) and IIB (Left). The symbols are as in Figure 4.

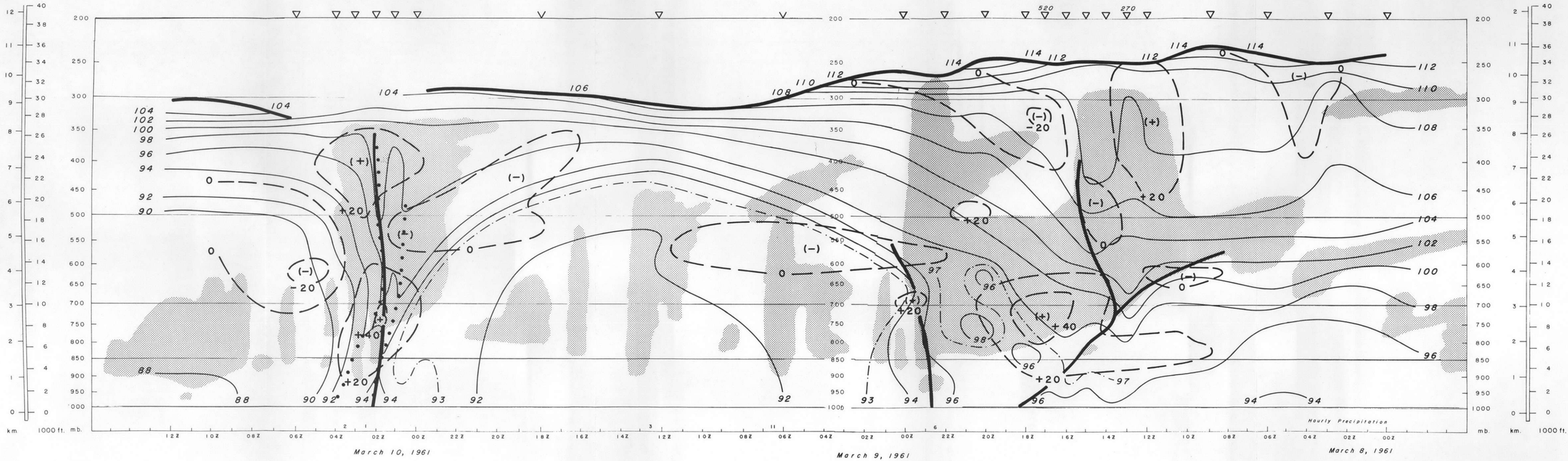

Figure 6. Time Section for Case IIIA (Right) and IIIB (Left). The symbols are as in Figure 4.

The σ-field in this case shows a broad $\vec{\nabla}\sigma$-zone* lowering in the warm frontal region as the occlusion approaches. This zone narrows and becomes very intense by 00Z 2 February. With passage of the pre-frontal surge and the appearance of dry, subsiding air and convection at middle levels, this quasi-horizontal $\vec{\nabla}\sigma$-zone erodes away until, by 05Z 2 February, all σ-surfaces are nearly vertical. In terms of static energy, the transition from warm to cold air masses began gradually with the pre-frontal surge but was very intense behind the front at 06Z with a slight break and a secondary intensification at 09Z.

Considerable potential instability, as indicated by a decrease of static energy with height, is found ahead of both the cold front and the secondary zone (at 09Z). It is not apparent from the data whether the pre-frontal mixing is the result of the release of potential instability which was originally in the warm air (see Section 3.5, Example 1), or by the release of potential instability formed by air overrunning the cold front and subsiding into the warm sector (see Section 3.5, Example II).

The release of potential instability could have produced the region of small $\vec{\nabla}\sigma$ between the primary and secondary zones of intense σ-gradient. Potential instability is present in the transition zone behind the cold front, and low-level rising motions can release convection which will split the σ-field into pre-frontal, primary, and secondary zones of various thicknesses with vertical σ-surfaces and different intensities of σ-gradient. Yet, the primary $\vec{\nabla}\sigma$-zone is so dominant in this case that a very sharp front appears on the synoptic scale.

4.2 Case II: 7-10 February 1961

4.2.1 CASE IIA

Two consecutive frontal systems are included in this case, an old decaying occlusion – IIA, and a recently developed system – IIB. The first storm occluded off the coast of Japan and traveled across the Pacific without any major reinforcement. Surface warm frontal history was poor in that the original surface warm front present during the occlusion stage had dissolved long before the occlusion reached North America (Figures B-6 and B-7).

When this frontal system reached Washington, a subsidence inversion, portions of the elevated warm front, and a vertical elevated cold front could be identified. The occluded front extended with a warm-type occlusion slope from 600 mb to 900 mb but was diffuse in the lowest levels (Figures 5, B-2 and B-8). The precipitation rates and wind speeds at all levels were unusually light. No measurable precipitation fell until several hours after passage of the elevated cold front.

* The term '$\vec{\nabla}\sigma$-zone' is used to mean 'a zone of relatively intense σ-gradient.'

The warm frontal cloud shield in Figure 5 is divided into two main layers: a high cirrus shield immediately beneath the tropopause and a separate middle-level shield associated with the warm front. About four hours before passage of the elevated cold front, these layers join into an essentially solid cloud mass extending from 650 mb to 280 mb. Except for the continual lowering of the base, little change in cloud structure occurs even with passage of the elevated cold front until clearing at middle levels begins after 06Z 2 February. The occluded front (warm-type slope) is surrounded by clouds whose tops lower with the occluded front and remain about 5,000 feet above the frontal surface. Convection breaks out intermittently within the middle level, dry air and considerable cirrus remain above this zone. However, the radar echoes show essentially stable-type precipitation within the cloud mass surrounding the occluded front.

The vertical-velocity field indicates subsidence both in the dry air beneath the warm front and in the clear air between the upper cirrus deck and the middle-level warm frontal shield. Ascent is indicated within the cirrus shield decreasing in magnitude with increasing distance ahead of the elevated cold front. Subsidence beneath the tropopause is indicated further ahead of the cold front where the cirrus is in patches. These conditions are similar to conditions in Case I and suggest that the cirrus shield beneath the tropopause forms ahead of the cold front, is advected out in advance of the system and dissipates, giving the shield-like appearance.

As in Case I, strong rising motion is indicated in the transition zone immediately behind the cold front and around the occluded front. Subsidence occurs in the cold air further back in the transition zone. A small region of subsidence is located immediately behind the elevated cold front. The vertical velocity computations show a relatively large amount of rising motion behind this frontal system (a feature which is supported by the cloud and moisture fields).

The σ-field near the warm frontal zone consists of a very intense quasi-horizontal $\vec{\nabla}\,\sigma$-zone above which there is little σ-gradient. Beneath this zone some potential instability exists in the dry air. The release of this instability probably would intensify the $\vec{\nabla}\,\sigma$-zone further.

The cold front marks the reversal of the slope of the σ-surfaces, and the transition zone is fairly complex in the σ-field. We see that zones of potential instability are located above the occluded front and that rising motion below the occluded front is tending to release potential instability. Hence, the transition from warm to cold air masses consists of a broad sloping $\vec{\nabla}\,\sigma$-zone with imbedded subzones of more intense σ-gradients. The intermittent release of potential instability above the occluded front gives a mixture of subsidence and ascent in the transition zone behind the cold front.

Notice that the intense warm frontal $\vec{\nabla}\sigma$-zone is continually eroded after passage of the elevated cold front until, by 12Z 8 February, only a minor $\vec{\nabla}\sigma$-zone remains.* The warm-type occluded front coincides with the top of this quasi-horizontal zone and becomes indistinct as the zone becomes eroded away. It is possible that at the height of development of this frontal system off the coast of Japan a concentrated sloping $\vec{\nabla}\sigma$-zone extended to the surface. After crossing the Pacific without any major reintensification, the sporadic post-frontal convection within the transition zone has produced a broad sloping zone with multiple minor subzones. After crossing the Rocky Mountains this front lost its identity. The mixing or erosion process weakened an intense occluded frontal zone until it could no longer be identified on the synoptic scale.

A large amount of evaporative cooling was observed beneath the cloud mass prior to passage of the elevated cold front. The thermal field as seen in Figure B-2 shows considerable cooling ahead of the occlusion which tends to mask the position of the fronts. Table 3 shows the relative humidity, ADV, and the local rates of change of humidity, temperature, and static energy for the layer 750 mb to 700 mb.

TABLE 3. Change of moisture, temperature, and static energy due to evaporation, Case IIA. The values are averages for the layer 750 mb to 700 mb. Notice that:

$$\frac{1}{c_p}\frac{\partial\sigma}{\partial t}\left(\frac{°C}{hr}\right) \doteq \frac{\partial\sigma}{\partial t}\left(\frac{j/g}{hr}\right) .$$

TIME		Rh	$\frac{\partial Rh}{\partial t}$	$\frac{\partial T}{\partial t}$	ADV	$\frac{\partial\sigma}{\partial t}$
Day (Feb. 1961)	Hour (Z)	%	%/hr	°C/hr	°C/hr	j/g / hr
7	2230	20	10	-0.39	0.31	0.43
8	0000	38	4	-0.30	-0.18	-0.02
8	0130	32	11	-1.18	-0.27	-0.78
8	0300	72	19	-0.60	0.33	0.59
8	0430	89	8	0.96	1.34	1.88
8	0600	95	2	0.30	1.39	0.60

The radar records in conjunction with the humidities suggest that the evaporation ceased about 0330Z 8 February. The cooling by evaporation appears, from the difference between local and advective temperature changes, to be about 0.9°C/hour at 0300Z. The fact that the static energy changes were less (algebraically) than ADV at 0130Z and 0600Z implies ascending motion at these times. This

* For a more complete discussion of this 'erosion' process, see Section 3.5.

example illustrates the effect evaporation can have on the density field in the vicinity of fronts.

4.2.2 CASE IIB

The second frontal system in this case, IIB, originated as a wave on front IIA and intensified very rapidly off the coast of Oregon. This rapid intensification may be due in part to a second cold front which formed in a trough northwest of the primary. The secondary moved southeastward and either died or merged with the stationary front trailing back from IIA. The center of the low passed within 100 miles of Seattle so that this case study exhibits the conditions present as an intensifying cyclone begins to occlude (Figures B-8, B-9, and B-10).

The convection following the frontal system in Case IIA is shown in Figure 5 to be suppressed by the lowering of the distinct warm frontal zone in Case IIB. The warm frontal cloud shield merges with the lower-level convection at 11Z 9 February. The cells of ascent and descent at higher levels above the warm front are more intense than the corresponding features in Cases I and IIA.

No pilot reports are available to substantiate the separation of the high cirrus from the warm frontal cloud shield between 08Z and 12Z 9 February. The cloud analysis is based on the fact that Cases I and IIA have such a cloud structure coinciding with a region of subsidence. The existence of the corresponding subsidence region in this case is well substantiated and the cloud analysis is felt to be justified. The observed precipitation rates are consistent with the cloud analysis and the mean vertical velocities (see Section 3.3.4).

The clearing ahead of the cold front is substantiated by soundings at and following 1830Z. Prior to this time neither soundings nor pilot reports were available in the region of middle-level clearing. The cloud analysis from 700 mb to 500 mb between 1200Z and 1830Z 9 February is based upon two considerations: (1) the radar echoes show evidence of convection; (2) the vertical-velocity computations indicate subsidence. Figure 7 contains prints of the radar echoes for Case IIB. The radar echoes ahead of the occlusion are similar to those found in Case I where the existence of convection imbedded in dry air ahead of a cold front is well established. This process of the release of potential instability in dry air ahead of an upper-level trough has been studied with vertically directed radar by Wexler and Atlas.[45]

The region of descent extending from high levels behind the cold front to middle levels ahead of the front is similar to but more intense than the corresponding feature in Case I. Moderate or strong ascent again surrounds the occluded (or occluding) front. Rising motion persists behind the cold front below 500 mb for five hours and is followed by subsidence further back in the cold air. The post-cold front ascent with a peak of 15 cm/sec is only one-third as intense as that found in

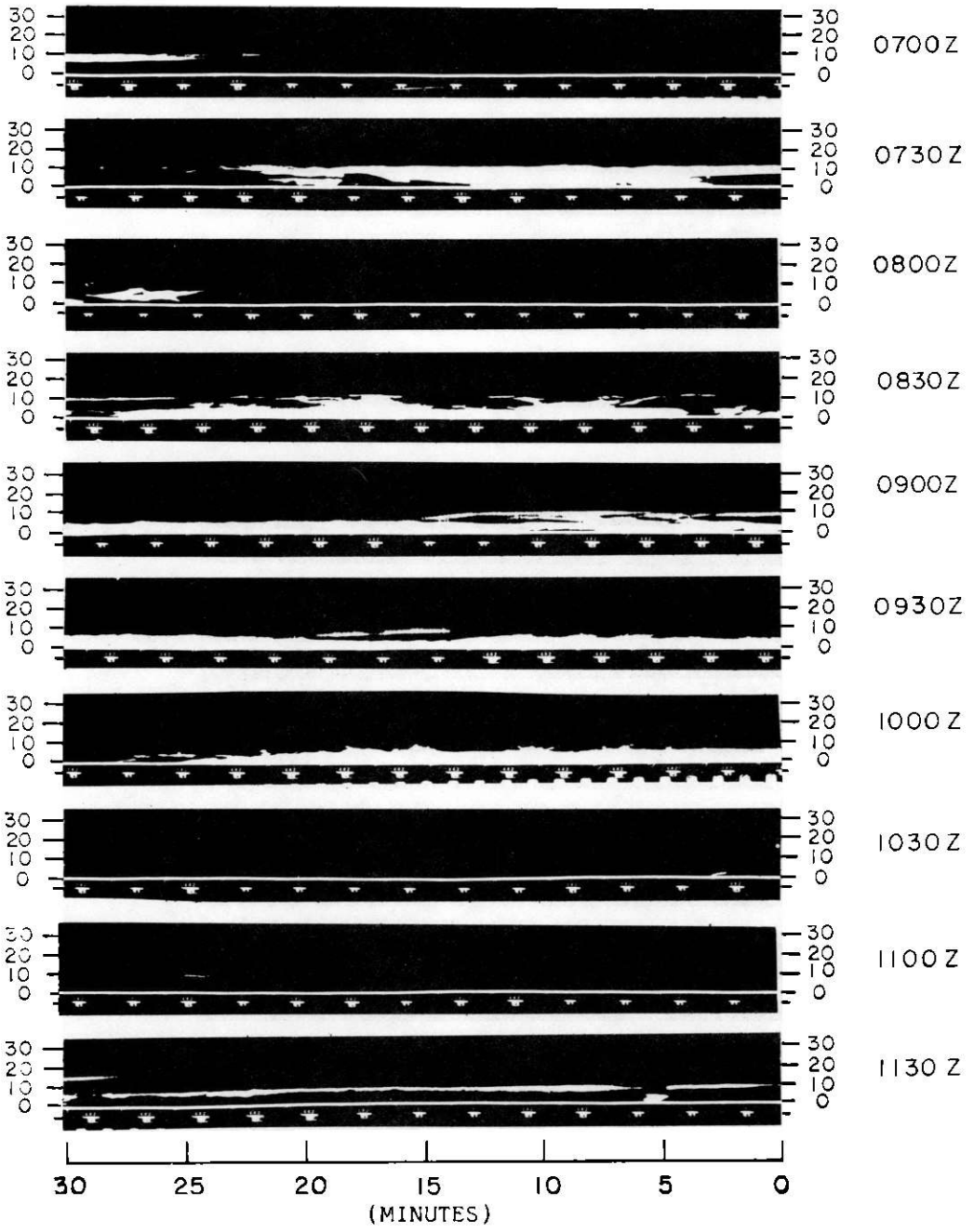

Figure 7. Radar Echoes for Case IIB, 9 February 1961. Height scale at end in 1000's of feet, time scale below. Part I.

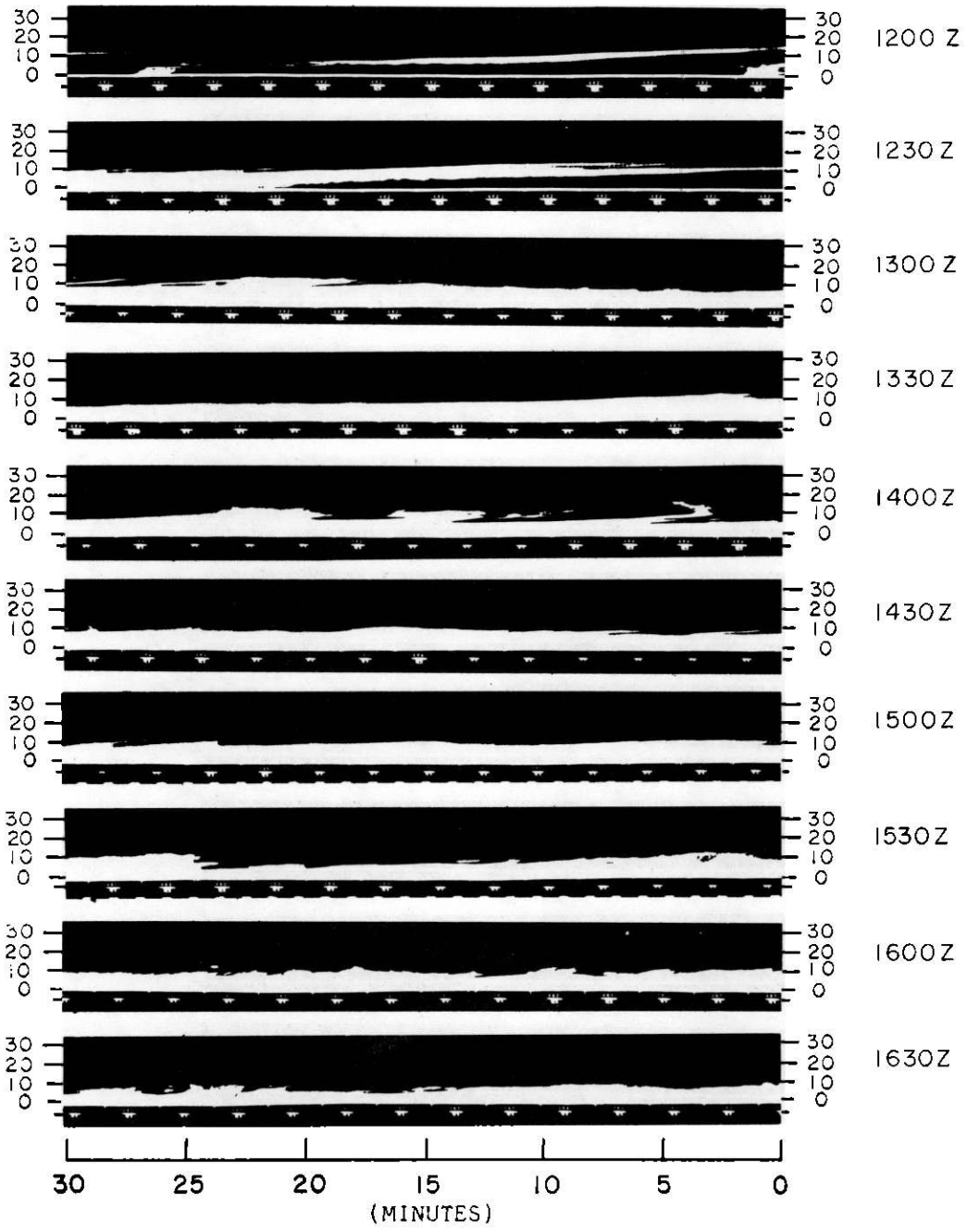

Figure 7. Part II

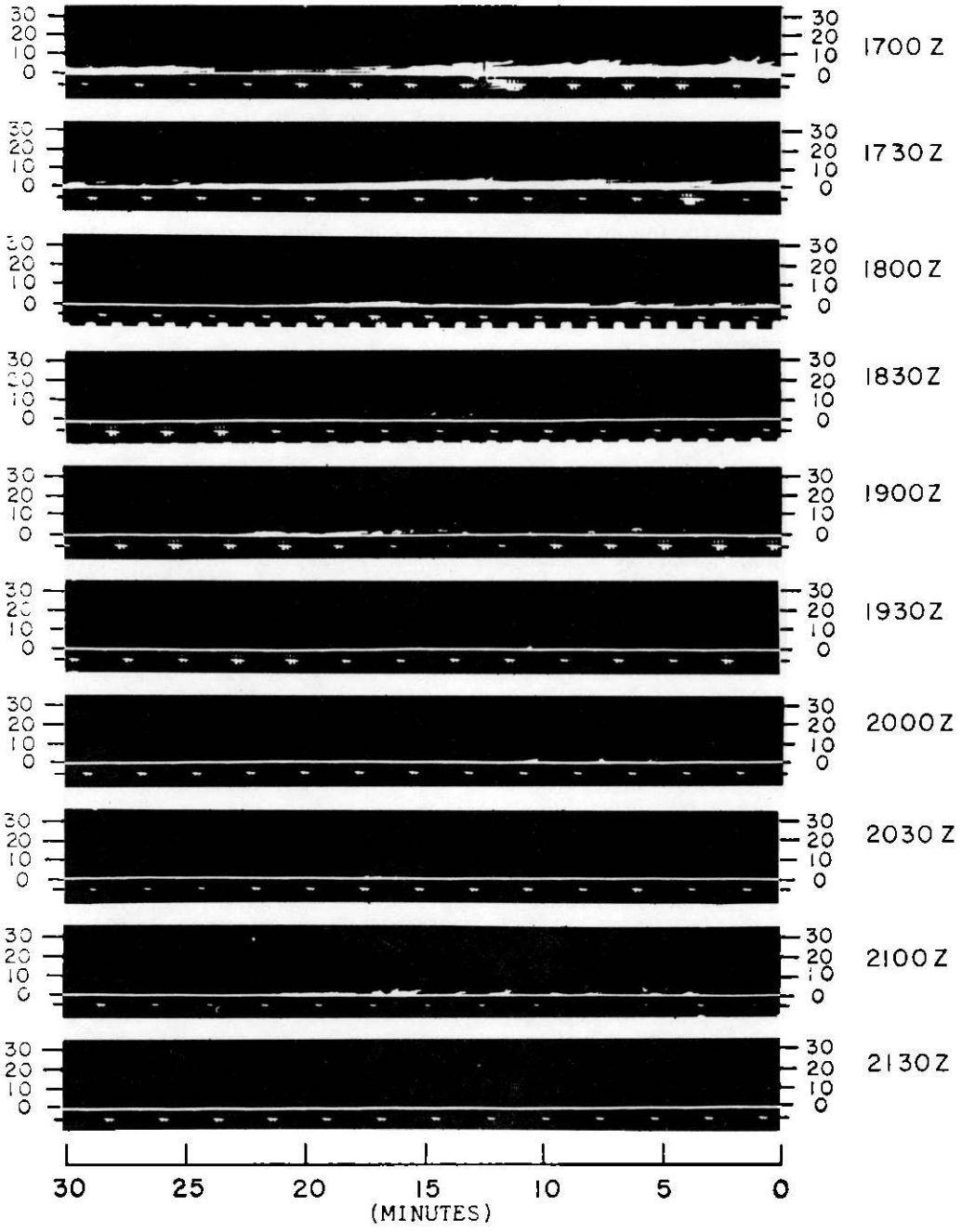

Figure 7. Part III

Case I. The fact that clearing occurs at some levels prior to subsidence can again be explained by the arrival of unsaturated air which had subsided further back in the cold air mass.

The serial ascent data present an interesting sequence of subsidence, clearing, baroclinity, static energy change, and cooling associated with the cold front from 600 mb to 400 mb. Table 4 contains the 50-mb averages of the relative humidity with respect to ice (Rhi), the static energy (σ) , the temperature (T) , and the wind direction (D) and speed (S) for soundings in this region. Table 5 contains the detailed winds, a portion of which are plotted in Figure B-2 in Appendix B. These winds are computed from one minute-averaged winds, $\vec{V}_1$, using the running mean formula,

$$\vec{V}(t) = \left[\vec{V}_1(t-1) + 2\,\vec{V}_1(t) + V_1(t+1)\right] / 4$$

where the '1' indicates one minute from time t.

TABLE 4. Sequence of 50-mb average: humidity, static energy, temperature and wind with a katafront, Case IIB

	Layer (mb)	9 Feb. 1961				10 Feb. 1961
		1900 Z	2000Z	2130Z	2245Z	0000Z
Rhi (%)	600-550	58	56	21	MSG	69
	550-500	69	70	0		37
	500-450	89	81	36		12
	450-400	96	71	70		0
σ (j/g)	600-550	110.6	109.8	107.7	MSG	102.8
	550-500	110.0	111.1	108.6		104.8
	500-450	111.1	112.5	111.4		106.8
	450-400	111.5	112.7	113.7		108.9
T (°C)	600-550	-10.5	-10.8	-10.7	MSG	-16.8
	550-500	-16.7	-15.9	-15.1		-19.9
	500-450	-22.5	-21.1	-20.7		-24.1
	450-400	-29.1	-27.6	-26.7		-29.6
D-S (deg. knot)	600-550	235 65	233 95	234 83	240 56	243 56
	550-500	234 66	228 80	240 100	240 83	240 78
	500-450	236 77	225 81	239 108	241 106	240 109
	450-400	236 86	234 87	236 110	237 126	241 126

TABLE 5. Detailed winds in the vicinity of a katafront, Case IIB. Units are: P(mb), D(deg), and S(knots).

9 Feb. 1961												10 Feb. 1961		
1900Z			2000Z			2130Z			2245Z			0000Z		
P	D	S	P	D	S	P	D	S	P	D	S	P	D	S
602	233	63	612	234	74	602	231	73	605	243	49	617	247	39
590	235	64	599	235	83	594	230	77	590	241	54	596	246	43
577	236	65	587	234	93	582	232	80	575	240	56	575	243	59
563	236	65	573	233	99	571	234	84	559	239	58	554	241	65
549	235	65	561	232	100	560	236	88	544	238	68	534	241	64
535	234	64	551	231	95	547	239	92	549	239	76	514	240	89
520	233	65	541	230	85	534	240	97	515	240	85	493	239	112
508	233	67	528	229	78	519	240	102	501	241	95	473	240	108
497	234	71	518	228	75	504	240	106	487	242	101	453	241	109
483	235	75	507	225	76	488	239	108	474	241	105	435	242	121
469	237	79	496	223	77	474	239	109	459	240	114	417	241	132
456	237	82	483	223	80	459	238	108	446	238	121	400	240	136
443	237	84	470	224	82	444	237	108	433	238	123			
431	237	86	457	227	83	429	236	111	420	237	126			
417	236	87	443	231	84	413	236	111	410	237	131			
405	236	89	429	233	86	397	236	111	400	237	137			
394	235	91	418	236	86									
			408	236	90									
			400	236	97									

Subsidence and clearing (Figure 5) preceded the elevated cold front, and the static energy surfaces dip and break sharply upward along the dotted line* ahead of the front. The baroclinity, as inferred from the hodograph, is also very intense in the sloping region of intense σ-gradient following this σ-front. The analyzed position of the cold front is based on the beginning of cooling (Figure B-2) and does not correspond with changes in vertical motion, cloudiness, static energy or even baroclinity! The position of the σ-front undoubtedly is the border of the air-mass transition zone and the major change in baroclinity, but the subsidence is sufficient to temporarily delay cooling.

The splitting of a frontal zone by mixing (see Section 3.5) is well illustrated in this case. A very definite but narrow vertical $\vec{\nabla}\sigma$-zone is located behind (to the left of) the σ-front from the surface to 700 mb. The second dotted line near 22Z delineates the leading edge of a second $\vec{\nabla}\sigma$-zone which is separated from the first

*This dotted line ahead of the cold front will be referred to as the σ-front, for it is at this point that the σ-field changes abruptly.

zone below 700 mb by a narrow homogeneous region.* Potential instability is present in the first $\vec{\nabla}\sigma$-zone from 850 to 700 mb. Ascent and some cloudiness is also indicated in this region.

Such a situation is ideally suited to the separation of a frontal zone and the production of either a secondary cold front or a pre-frontal mesoscale line, possibly similar to the squall line presented by Newton.[46] At some later time, if the first narrow $\vec{\nabla}\sigma$-zone moves away from the secondary zone and becomes diffuse, the primary synoptic front may shift back to what is now the secondary zone. There is no physical factor preventing the secondary zone from overtaking the primary warm front and occluding. Upon completion of this hypothetical process, the σ-field would look remarkably similar to that observed in Case I. It appears plausible, then, that the pre-frontal surge in Case I formed from a splitting of the primary front at an earlier time. Possibly it had overrun the lower level front and had been separated by convection from the rest of the transition zone.

4.3 Case III: 8-10 March 1961

4.3.1 CASE IIIA

In this case just as in Case II, there are two frontal systems, IIIA, an old system which occluded off the coast of Japan, and IIIB, a newly developed structure which formed off the west coast of the United States. Case IIIA had an extremely long and interesting lifetime over a period of twenty-six days. Figure 8 shows the position of this frontal system at 00Z from 27 February 1961 to 24 March 1961. These positions are based on the National Meteorological Center surface analyses.

The front originated in a trough in Siberia and was analyzed as a cold front at 00Z 27 February. The system occluded as it moved into the Pacific and had poor warm-front continuity east of 180° longitude. When the system passed Seattle it was an old, slowly moving occlusion, but upon crossing the Rocky Mountains, it was again analyzed with an open warm sector. As the system moved across the United States, its amplitude decreased and its speed increased until it became a rapidly moving open wave. About 30°E longitude, the front overtook the decaying system ahead of it. Rapid development and occlusion followed. Frontal continuity is consistent with the interpretation of the resulting frontal system as an intensification of the overtaking front. The occlusion then moved through northern Europe and across Russia, dying not far from its birthplace twenty-six days earlier.

---

* In the preliminary analysis (Figure B-2) the region between these two $\vec{\nabla}\sigma$-zones was interpreted as a narrow warm sector. The subsequent σ-analysis revealed that the front had occluded up to about 850 mb but that the majority of the lower level cooling followed the passage of the secondary cold front.

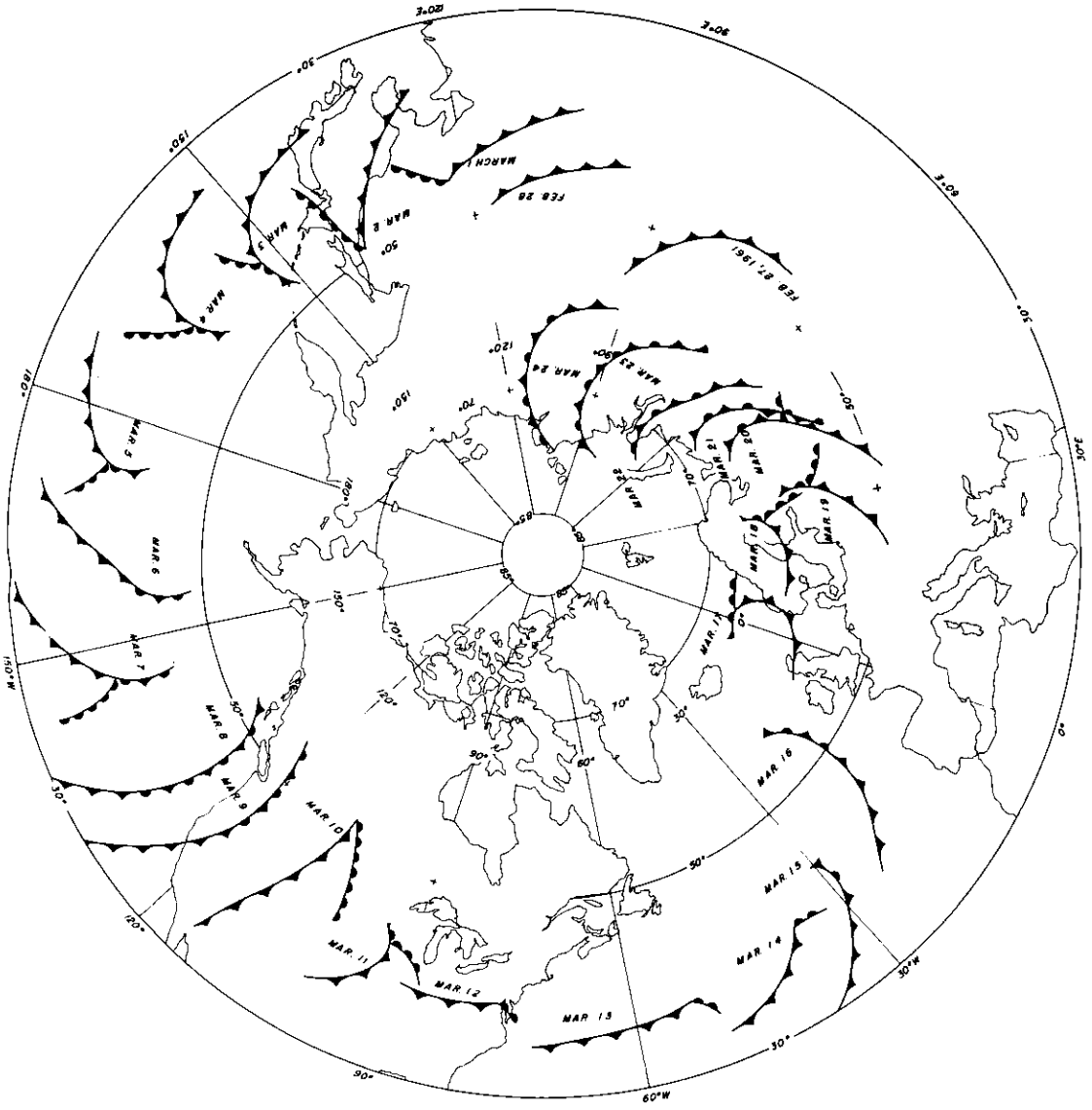

Figure 8. Life History of Front in Case IIIA

One cannot state that the structure depicted in Figures 8, B-11, and B-12 is continuous on the mesoscale. However, on the synoptic scale the feature is both important and continuous over the twenty-six day period, even though major modifications and regenerations did occur. It is interesting to examine the mesoscale structure of the system as it passed Seattle and to speculate as to what characteristics of the structure are responsible for its excellent temporal continuity on the synoptic scale.

The warm front (Figure 6) is poorly organized with multiple stable zones and cloud layers. The pre-system convection below 650 mb was replaced by very dry air about 22Z 7 March. The low-level dry air persisted and no measurable surface precipitation occurred until the arrival of the secondary cold front twenty-four hours later. As in Case IIA, considerable evaporative cooling occurred, complicating the thermal structure in advance of the occlusion. The σ-field was unaffected by this cooling. In fact, the static energy rose during the period of most intense evaporation. In this case an occluded front located on the basis of the thermal field would coincide with the onset of evaporative cooling rather than the change of air mass and static energy.

The warm-sector vertical motions were weak with this old system. As in the other cases, rising motion was present in advance of the elevated cold front at high levels, decreasing in magnitude with increasing distance from the front. The separation of the cirrus beneath the tropopause from warm frontal clouds is again evident. However, subsidence appears to have separated the advance cirrus shield from the clouds and rising motion immediately ahead of the elevated cold front.

A region of descent is again found in the upper troposphere behind the elevated cold front extending downward across the elevated cold front into the warm sector. The subsidence in the warm sector contradicts the cloud analysis but not the radar records. The radar records show tops varying from 10,000 to 15,000 feet from 09Z to 12Z and a sharp drop in echo tops from 20,000 to 14,000 feet at 13Z. It appears that while the mean vertical velocity is downward there are imbedded regions of ascent. The cloud free regions were probably limited in extent, and they are not indicated in the cloud analysis. Computations indicate subsidence near 500 mb at 14Z because cold advection is indicated by the hodograph on three consecutive soundings. Table 6 lists both the detailed winds and the (apparent) advective temperature change, ADV, for the region involved.

Rather strong rising motion surrounding occluded fronts is seen in Figure 6 as well as in Figures 4 and 5. The computed vertical velocities, the clouds, and the precipitation all attest to the fact that below 500 mb the air was rising between the occlusion and the secondary cold front in Case IIIA. The shower with the secondary cold front produced the first measurable surface precipitation amounts of the storm. Substantial clearing, showers, and some middle-level subsidence followed the secondary cold front.

TABLE 6. Detailed winds and advective temperature changes at middle levels in Case IIIA. ADV-values are the 50-mb averages for the three layers between 600 mb and 450 mb

TIME (8 March 1961)												
13Z				14Z				15Z				
P	D	S	ADV	P	D	S	ADV	P	D	S	ADV
601	196	48		602	207	54		598	207	67	
587	197	48	0.41	587	208	54	-0.14	583	208	69	0.40
571	197	50		571	207	54		569	208	69	
556	198	51		557	207	54		555	208	68	
542	199	52		544	206	55		541	208	64	
529	198	54	-0.84	531	207	55	-0.35	526	206	60	-1.93
515	197	54		519	207	55		512	203	55	
504	195	54		508	206	53		499	199	51	
490	191	57		497	204	50		486	195	49	
476	188	58	-1.08	484	200	48	-2.17	474	191	48	-1.55
462	187	57		474	196	48		462	189	48	
450	188	57		461	192	50		451	189	50	
				450	191	54					

Having examined the structure of this frontal system as it passed Seattle, it is interesting to investigate its structure as revealed by the surface observations at the picket ships fourteen hours earlier. Figure 9 shows the three-hourly surface observations from the three picket ships and the surface analysis coinciding with frontal passage at the picket ships. The three-hourly observations were obtained from photostatic copies of the observation log, WBAN 11B. The occlusion passage was just prior to 21Z at SO, 00Z at SP, and 03Z at SQ. There are indications of a secondary feature just prior to 06Z at SO, 06Z at SP, and 09Z at SQ.

The occlusion had a very pronounced surface structure at this time, but within fourteen hours the occluded structure was very weak below 800 mb. Figure 8 shows that the occluded front did not appear east of the Rocky Mountains. This case illustrates rapid frontolysis of an occlusion without destruction of the synoptic front at upper levels.

The σ-field in Case IIIA (Figure 6) indicates a poorly organized, quasi-horizontal warm frontal zone and undulating σ-surfaces in the warm sector. There is a definite dip in the σ-surfaces at the elevated cold front, a feature also present in Case IIB. The isotherm analysis in Figure B-3 shows clearly a warm peak at the cold front above 550 mb. Below 550 mb, evaporative cooling resulted in the peak σ-values corresponding to peak mixing ratio values rather than a peak in the thermal field.

The transition zone following the cold front consists of a broad zone of sloping (in time) σ-surfaces with moderate or weak gradients. Within the transition zone a mixing zone extending to 600 mb is preceded by the primary front and followed by

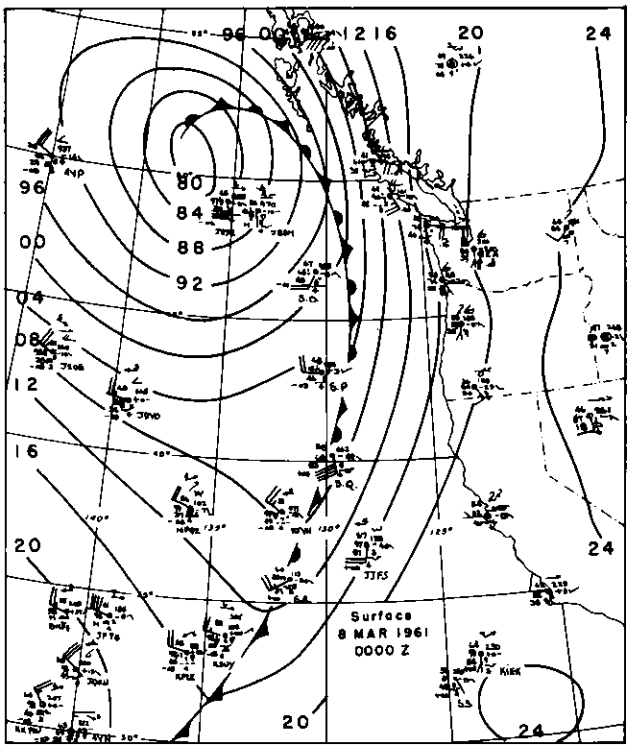

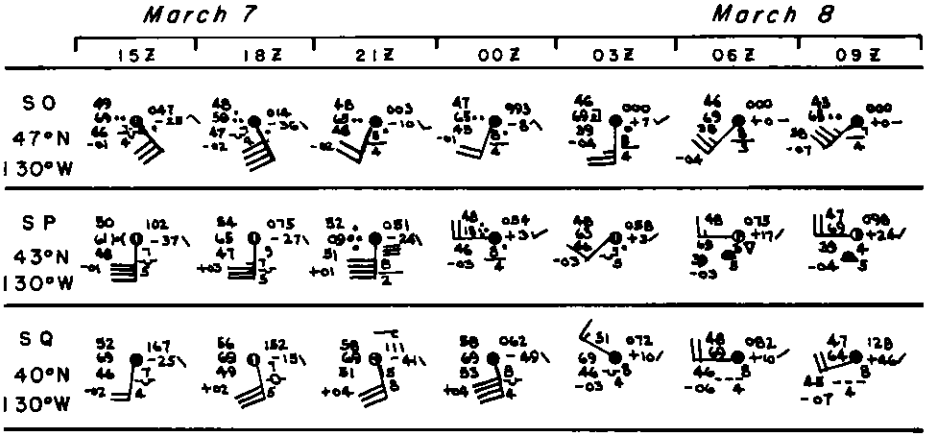

Figure 9. Surface Chart and Three-hourly Surface Observations Coinciding with the Passage of Front IIIA at the Picket Ships

the secondary cold front, each of which has an associated $\vec{\nabla}\sigma$-zone. It is rather surprising that a frontal system with twenty-six-day continuity on the synoptic scale and a sharp surface front as it passed the picket ships would have such a poorly organized transition zone on the mesoscale at Seattle. Apparently the mesoscale features can change rapidly without disrupting synotpic scale patterns.

4.3.2 CASE IIIB

The second frontal system in Case III, and the last system to be presented, is the most unusual of the set. A cyclone had developed off the coast of Japan on the front trailing back from Case IIIA. The system occluded and the wave portion propagated out of the parent cyclone discarding its occluded portion. The resulting open wave traveled rapidly across the Pacific and redeveloped about 600 miles off the coast of Oregon.

The baroclinic zone with the preceding system, Case IIIA, was essentially split by the circulation of this redeveloping wave (Figures B-13 and B-14). The structure that formed was described in the preliminary report as an occlusion extending to 350 mb. The 'occlusion' term was used since the true warm sector remained far to the south. On the other hand, the splitting of the baroclinic field left a semi-barotropic quasi-warm sector. One may prefer to describe this structure as an open wave on an 'interpolar' front[7] above about 700 mb. Figure 10 is the 500-mb chart which shows the structure of the 'occlusion' and the quasi-warm sector particularly well. Let us now examine the mesoscale structure of this odd type of frontal system.

The cloud system was deep (to 27,000 feet) and narrow (nine hours at high levels and about six hours at middle levels). The surface precipitation was light (0.02 in.) and occurred in measurable amounts only after frontal passage. Clearing with imbedded showers occurred in the cold air but not until a few hours after cooling had begun. Considerable turbulence (from pilot reports) coincided with the cooling, suggesting strong convection in the transition zone.

The vertical-motion pattern shows subsidence at middle levels ahead of and behind the front and strong rising motion centered about the front. Large, intense cells of ascent were located at high and low elevations and were connected by a narrow zone with small magnitudes at middle levels. The subsidence at 550 mb just ahead of the front is associated with strong cold advection. Perhaps this is the result of small-scale motions, on a scaler smaller than is used in the cloud analyses. Subsidence at this point is neither contradicted nor confirmed by either the relative humidity values (90% for ice, 72% for water) nor the radar echoes, which cease below this level. The fact that the large ascent rates were accompanied by such small precipitation rates can be attributed to evaporation in the unusually dry air at low levels. Pre-frontal ceilings remained above 7000 feet.

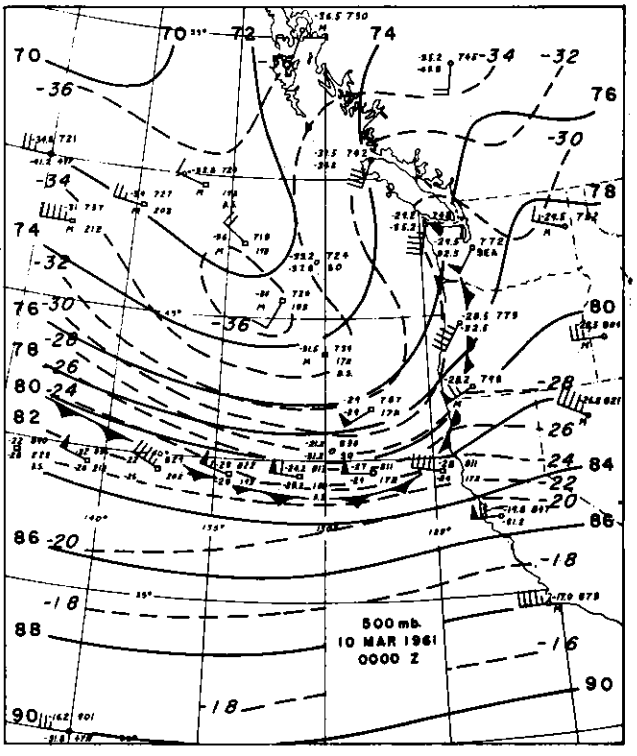

Figure 10. 500-mb Chart, 00Z 10 March 1961.

The σ-field is remarkable in this case. A narrow $\vec{\nabla}\sigma$-zone does arc downward similar to a warm frontal zone. Notice that the range of σ-values is from 93 to 96, the same as the range of the $\vec{\nabla}\sigma$-zone associated with the preceding secondary cold front (in Case IIIA). While it seems inconceivable that this zone is a direct continuation or extension of the secondary cold front, it does demonstrate that this zone is a continuation of the coldest portion of the transition zone in Case IIIA. The warmer portion of the transition zone in Case IIIA remained south of Seattle as is evident from Figure 10.

The double structure of the σ-field near the front was established by a careful analysis of the data. The data are contained in three soundings with consistent 500-mb heights so this pattern cannot be dismissed as an observational error. It is interesting to note that a large amount of turbulence was reported by pilots in the interval between the two downward peaks in σ.

The following explanation is suggested to account for this most interesting double dip in the σ-surfaces. As the front at 600 mb advanced ahead of the lower-level front, a small amount of potential instability was formed in the subsiding air in the transition zone. This potential instability was subsequently released by the

ascending air associated with the low-level convergence. Strong mixing followed, and free and forced convection within the transition zone split this zone. The forced convection advected the σ-surfaces upward forming the upward peak in the σ-surfaces between the dips. This feature corresponds to the pre-frontal cooling and subsequent warming indicated at many levels in Figure B-3.

This last case is an excellent example of the ability of a σ-analysis to clarify the structure of the atmosphere. The large extent to which mesoscale features can alter circulations in a storm is also demonstrated. The uniformity of the cold air masses and the sharpness of the change in slope of the σ-surfaces show that these surfaces are useful indicators of air masses and transition zones. The complexity of the σ-field in the mesoscale demonstrates that a front located with synoptic data cannot be expected to bound a single mesoscale hyperbaroclinic zone.

4.4 Similarities Observed Among the Cases

In spite of the fact that these five frontal systems differ greatly in their state of development and configuration, certain features were observed in more than one case. Such features, which may possibly be present in many frontal systems, will now be summarized.

The younger occlusions, Cases I, IIB, and IIIB, have significant but somewhat divided frontal zones extending nearly vertically to the surface. Case I has some horizontal σ-gradient ahead of the elevated cold front, strong gradients immediately behind the cold front, and a secondary zone of large gradient farther in the cold air. Case IIB has a distinct division of the (mesoscale) frontal zone below 650 mb, and the analysis of Case IIIB contains two closely spaced first-order discontinuities in the σ-field. The older occlusions, Cases IIA and IIIA, have a different type of occluded frontal structure. In these latter cases, the occluded frontal zone is a quasi-horizontal extension of the warm frontal zone which, upon passage of the elevated cold front, is progressively eroded away without ever reaching the surface. The cold frontal boundary is much less pronounced in the older systems, but a broader transition zone with substantial total static energy change is present. The action of convection in splitting or eroding the frontal zones is implied in the static energy analyses of all the cases.

While the vertical-velocity fields in these cases are much more complex than earlier frontal models implied, they are in reasonable agreement with the observational study of Sansom[26] and the models of Eliassen.[47] In these latter models the axis of zero vertical motion is in the center of the transition zone (rather than along the frontal surface) with ascent in the warmer (transition) air and descent in the cooler air. In the case studies ascent is found surrounding the occlusion and in the transition zone immediately behind the elevated cold fronts. Cases I and IIB and, to some extent Cases IIA and IIIA, have a zone of subsidence extending from higher

levels behind the cold front down to 600 mb ahead of the front. These observations support Sansom's conclusion[26] that the katafront feature coincides with rapid occlusion of the cyclone. The magnitudes of these mesoscale vertical motions are generally larger in the younger occlusions with peak values in excess of 40 cm/sec.

The lowering of the stable,warm frontal region is effective in suppressing the convection in the cold air preceding the frontal systems in Cases I, IIB, and IIIB. The warm frontal stable zones generally have a smaller slope than the corresponding cloud and vertical motion fields. This fact, along with observed discrepancies in the post-frontal clearing and the frontal boundaries, demonstrates than an accurate knowledge of cloud boundaries will not allow accurate placement of frontal surfaces and vice versa. The separation of the warm frontal clouds from the higher level cirrus clouds, and the similar separation of corresponding regions of ascent, can be seen in Cases I, IIA, IIB and, to a lesser extent, in Case IIIA. This feature may occur more frequently than surface observations would indicate.

5. CERTAIN ASPECTS OF OCCLUSION STRUCTURE

It is the purpose of this section to present conclusions about the mesoscale structure of occluded frontal systems based upon the limited number of serial ascent cases and a review of the literature. Only the mesoscale fields of temperature, static energy, and vertical motions will be considered. Certain limitations, problems, and capabilities of synoptic analysis will then be discussed in view of the mesoscale structure of frontal systems, but no major revisions appear to be necessary in conventional analysis techniques.

5.1 Mesoscale Structure

5.1.1 TEMPERATURE AND STATIC ENERGY

The warm frontal zones, characterized by high static stability, large static-energy gradients, and a veering of the wind with height, are usually comprised of multiple mesoscale stable zones. The individual subzones may be the result of recent classical frontogenesis, the remnants of a former cold front which is returning northward, or the result of subsidence or evaporational cooling. Rarely does one find a single surface extending from near the ground to the middle troposphere which continuously (on the mesoscale) bounds the warm edge of a single stable zone. An analysis of the static energy (or a similarly conservative quantity) field in the vicinity of these stable zones is very helpful in delineating and interpreting individual subzones. Figure 11 is a sketch which illustrates the frontal zone terminology used in this section.

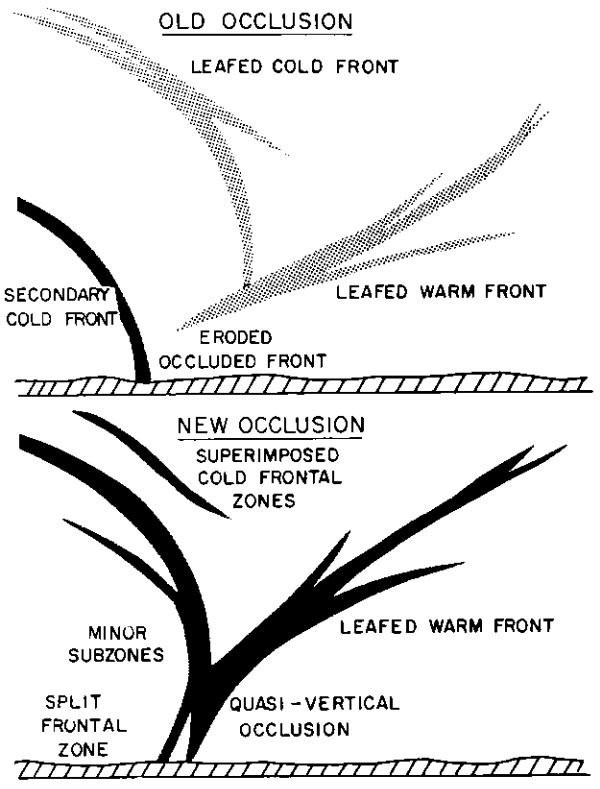

Figure 41. Schematic Diagram to Illustrate Frontal Zone Terminology. The darker zones are the more intense.

In certain older warm-type occlusions, such as Cases IIA and IIIA in Section 4, the warm frontal zone is broad and has a small time-section slope. Upon passage of the elevated cold front, this broad stable zone is progressively eroded away and never extends to the lowest levels. The occluded front in such case is the remnants of the warm frontal zone and is apparently of limited significance. If sharp features are present at the surface in such cases, they are likely to be secondary cold fronts, such as are observed in Cases IIIA and to a lesser extent (or in an earlier stage of development) in Cases I and IIB. The models of Godson and Jacobson (see Section 2. 1) are perhaps as useful as the classical model in representing older occlusions.

Some of the more recently formed and active occlusions (Cases I, IIB, and IIIB in Section 4) extend nearly vertically to the surface but are rather unstable in the sense that the frontal zone is often split (see Section 4. 4). In the case studies, secondary cold fronts and even pre-frontal rain bands were associated with subzones which were separated from the frontal zones. The squall line presented by Newton[46] could be the result of a split in the frontal zone associated with a cold front. The

relative influence of convection and larger scale circulations in splitting these frontal zones remains to be determined.

Unfortunately the detailed structure of occluded frontal zones can not be determined from synoptic data. Contrary to what Godson[8] implies, it is impossible in most cases to distinguish between a warm-type occlusion which extends to the surface and a diffuse occluded structure with a secondary cold front on the basis of synoptic data.

It should also be emphasized that the slope of an occlusion does not depend, as classical theory states, on the relative coolness of the displaced and the displacing air masses. The slope of an occluded front (with a continuous temperature field as is nearly always found in nature) is given by the standard equation:[8]

$$\left(\frac{dz}{ds}\right)_F = \frac{\left(\frac{\partial T}{\partial s}\right)_B - \left(\frac{\partial T}{\partial s}\right)_A}{\gamma_B - \gamma_A}$$

Here $(dz/ds)_F$ is the frontal slope and the subscripts A and B refer to ahead of and behind the occlusion respectively. s is the distance normal to − and positive ahead of − the front. For an occlusion,

$$\left(\frac{\partial T}{\partial s}\right)_B > 0 ; \quad \left(\frac{\partial T}{\partial s}\right) < 0 ;$$

$$\therefore \left(\frac{\partial T}{\partial s}\right)_B - \left(\frac{\partial T}{\partial s}\right)_A > 0 .$$

The occlusion slopes toward the more stable (smaller γ) surroundings. Neither the temperature nor the stability of the air masses far from the front has any necessary connection to the frontal slope. With a front imbedded in a broad baroclinig region separating air masses, it is particularly unrealistic to use air mass characteristics to deduce frontal slope. Correlations of occlusion slope to air mass types may or may not be statistically significant when a large sample is used. However, there is certainly no one-to-one correspondence.

From the relation of occlusion slope to the stabilities on either side of it, one can see that occlusion slopes can change rapidly in magnitude and/or sign. The change can occur as air having different stability is drawn into the circulation ahead of or behind the occlusion or as the vertical motion alters the stability difference across the occluded front.

The mesoscale thermal and static energy structure of cold fronts appears, from the case studies in Section 4 and a review of the literature, to vary in both

intensity and configuration. Contrasting Cases I and IIB with Cases IIA and IIIA, one notices substantial air mass differences in all cases. but in the latter cases the transition behind the elevated cold front takes place over a relatively broad and disorganized zone. The intense zones in Cases I and IIB appear to be so nearly vertical that splitting, such as has occurred in the occluded frontal zones, could occur in the cold frontal zones in the near future and result in a diffuse frontal structure.

The work of Danielsen and McClain, [16], Saucier, [48] (Figs. 6.13de), Reed, [11] Sawyer, [17] Endlich and McLean, [13] and Danielsen [49] leaves little doubt that multiple subzones are either leafed together or superimposed (See Figure 11) in the vicinity of cold fronts as well as warm fronts. The superimposed model of Endlich and McLean with a 'jet front' lying above a 'polar front' or the corresponding situation discussed by McIntyre [50] is the natural consequence of the ability of nature to form any number of 'air masses' and 'frontal zones.' A mesoscale analysis will distinguish the subzones which are combined in a synoptic frontal analysis.

To summarize, the thermal structure of fronts is characterized by multiple, narrow hyperbaroclinic zones which form, combine, split, and decay within the broader baroclinic zones separating relatively barotropic air masses. The duration of many of the individual subzones may be far less than that of the broad zone and the synoptic fronts.

5.1.2 VERTICAL MOTION

Mesoscale vertical motion patterns have rarely been obtained using even indirect means. The values computed using the serial ascent data are sufficiently reliable to depict general patterns, but the magnitudes and cell boundaries can be deduced only approximately. The patterns are far more complex than the classical frontal models implied but are in reasonable agreement with the recent models of Eliassen. [47] These models indicate a direct circulation in the frontal zone with ascent in the warmer portion and descent in the cooler portion of the transition zone. As Sawyer [17] observed, frontal zones in the free atmosphere have a considerable width so that Eliassen's models imply ascent for some time after passage of the cold frontal surface.

The warm frontal vertical motions are not found to be well correlated to the position or orientation of the warm frontal zone. Often a region of subsidence has been found to separate the ascent and clouds near the warm front from a higher region of ascent and cirrus extending from around 400 mb to the tropopause (see Section 4.4). In these cases no evidence is present to suggest that a second warm frontal zone is associated with the higher region of ascent and cloudiness.

The occluded fronts in the case studies are consistently surrounded by rising air. This vertical-motion field may contribute signficantly to the release of

potential instability and a corresponding splitting of the nearly vertical occluded frontal zones and the erosion of the quasi-horizontal warm-type occlusions. This vertical-motion field would also tend to keep the quasi-horizontal surface aloft and intensify the low-level horizontal air-mass contrast through horizontal convergence. This factor could be significant in the formation of secondary cold fronts.

The vertical motions about the cold fronts vary considerably with the intensity of the fronts. The more intense elevated cold fronts are followed immediately by ascending motion. Descent occurs in the colder portion of the transition zone with comparatively lower magnitudes, but perhaps over larger areas. A zone of subsidence extends from high levels behind the cold front downward and forward to about 600 mb ahead of the cold front. This katafront feature varies greatly in intensity in the cases studied; it is particularly well organized in Case IIB.

These conclusions regarding mesoscale vertical motions are based on limited data, but the patterns do indicate recurring and very interesting features.

5.2 Implications of Mesoscale Structures in Synoptic Analysis

Throughout this section it will be assumed that a 'synoptic front' is located using synoptic data and conventional procedures.[48] The preceding discussion of mesoscale structure raises the question of the significance of a synoptic analysis of fronts. Certainly synoptic data do not permit resolution of detailed mesoscale structures such as those present in Cases IIB and IIIB. The synoptic data can, however, locate the broader baroclinic zone and approximately locate the principal, intense hyperbaroclinic subzone.

A realization of the complexity of the mesoscale structure explains much of the apparent ambiguity as to the height of the frontal surface on a sounding. The soundings depict the small-scale features in the vertical, but the synoptic spacing of soundings in the horizontal and in time allows resolution of only the larger-scale features in the latter dimensions. The cloud patterns have been shown by these case studies, as well as by Sawyer,[17] to be unreliable indicators of frontal position. The middle-level clouds are best suited to denoted frontal position, but even at these levels clearing can either precede or follow the front. Further studies may provide grounds for obtaining accurate frontal positions from cloud data in certain situations.

At the present time, however, the analyst must smooth out complexities in the data to obtain a smooth frontal analysis consistent with the synoptic scale of the observations. The importance of the mesoscale hyperbaroclinic zones can then be emphasized in a synoptic analysis by a concentration of the isotherms into a frontal zone on a constant-pressure chart or the corresponding concentration of potential temperature (or equivalent-potential temperature or static energy) isolines

into a frontal zone on a cross section. Such a 'de-smoothing' process is justifiable even if it is unable to accurately portray the mesoscale hyperbaroclinic zones. This analysis will provide an approximate and smoothed location of the principal hyperbaroclinic subzones.

There has been neither observational nor theoretical justification presented in the literature to justify the specification of a fixed number of air masses or frontal zones in the atmosphere. On the contrary, evidence suggests that the structure, number, and even the meaningfulness of air masses vary from region to region and season to season. As discussed extensively by Godson,[7] even the number of operationally useful frontal zones varies with region and season. The literature is misleading when distinction is not made between those models designed only to approximate nature as closely as possible and those models which are formulated in view of the needs and the operational limitations of a particular weather service.[5]

A more serious analysis problem arises when the warm frontal structure becomes too diffuse to adequately distinguish the point of occlusion – the point beyond which a cold front becomes an occluded front. The mesoscale studies suggest that frontal zones have complex structures on the mesoscale so that fronts based on synoptic data are necessarily artificial constructions. When a criterion is established to designate the degree of organization required for the inclusion of a warm front in the analysis, a corresponding criterion must be arbitrarily established to distinguish between a cold front and an occluded front. The criterion would probably consist of a critical magnitude of either the horizontal thermal or thickness gradient along the front. An occlusion would have gradients exceeding the critical value. With such an objective criterion, one would undoubtedly find the formation of occlusions in the absence of identifiable warm fronts as well as the conversion of segments of occluded fronts back into cold fronts.

It is obvious that the mesoscale structures inferred from the limited number of serial ascents need extensive additional investigation. The extent to which these structures exist in other locations is yet to be established. The full implications of such mesoscale phenomena will not be realized until many observational as well as theoretical investigations have been assessed. Many of the preceding conclusions, however, are based on overwhelming observational evidence gathered by preceding studies as well as the serial ascent cases.

6. CLOUD AND PRECIPITATION STRUCTURE OF OCCLUSIONS

One of the basic goals of frontal theory has always been to establish the relationship between frontal location and cloud and precipitation features. Forecasters

attempt to utilize fronts as coordinates to which the weather can be related so that upon forecasting frontal movements and developments the future cloud and precipitation features can be deduced. Numerical forecasts of pressure fields from which future frontal positions can be estimated are reasonably satisfactory. Inference of weather even from a given pressure field remains extremely difficult.

Front-weather relationships have recently been investigated using soundings, aircraft, radar, and satellites. The ability of vertically directed radar to provide a convenient time section of the precipitation structure of storms makes it well suited for front-weather studies. The detailed weather features of the serial ascent cases have been presented and discussed in earlier sections. It is the purpose of this section to present the results of a study of many frontal systems using the continuous radar data but only standard radiosonde observations.

6.1 Frequency of Occurrence of Common Features

The radar data were classified both subjectively and objectively and compared with the relative position of the occluded front to the radar. The radar data from about thirty of the more clearly defined occlusions were examined to determine the best precipitation model for the sample. The region around the front was divided into squares, 100 nautical miles on a side. The data in each block were then statistically analyzed.

Figure 12 presents the results of the analysis of the radar echo-front relationship using the APQ-39 vertically-directed radar (1.87-cm wave length). The surface occluded front and the peak of the surface warm sector were used as coordinates. See Table 1 for the definition of the echo classes 1, 2, L, M, etc. One can see from these results that precipitation echoes of some type are observed nearly 90% of the time up to 200 miles ahead of occlusions and about 70% of the time for 150 miles behind the occlusions. Stable echoes are found less than one third of the time within the region extending from about 200 miles ahead of to about 250 miles behind the occluded front. Semi-convective echoes are fairly common ahead of the occlusion up to 200 miles north* of the surface warm sector. Beyond 100 miles north of the surface warm sector, these echoes are common behind the occlusion as well. Convective echoes are relatively scarce except immediately behind the occlusion just north of the warm sector.

Low echoes were found to be common for 200 miles ahead of the occlusion and behind the occlusion at some distance from the surface warm sector. Middle echoes are most common far ahead of the occlusion and least common more than 100 miles behind the front. High echoes occur generally less than one-third of the time.

---

* North in this sense means 'along the occlusion away from the warm sector' and can be interpreted literally only when the occlusion is oriented north-south.

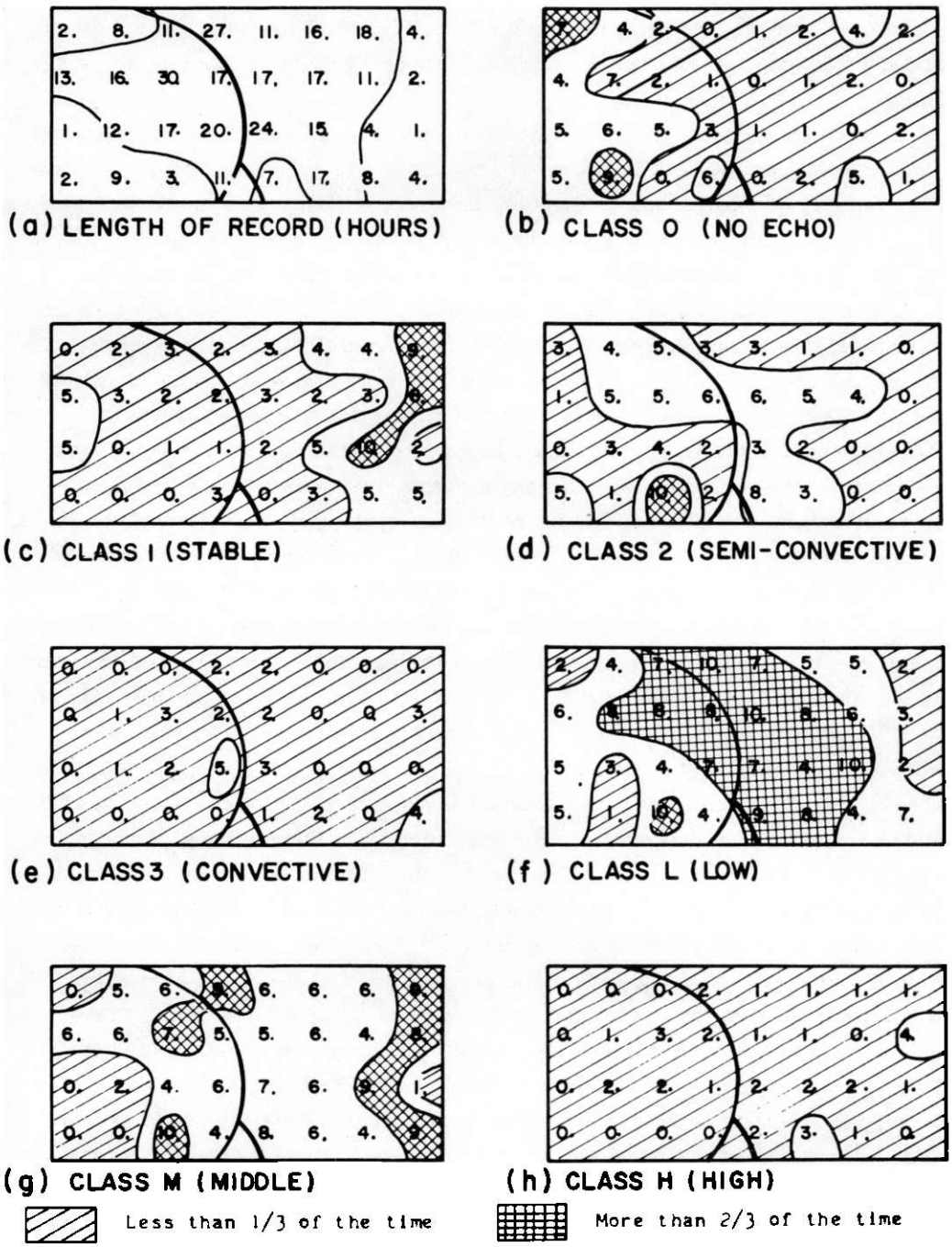

Figure 12. Average Relation of Radar Echoes to Frontal Position. The data point spacing is 100 nautical miles.

It can be seen that the classical occlusion-precipitation model is as good as any model. However, frequencies above 50% in Figure 12 are rare except for the occurrence of some low and middle echoes [Figure 12 (f, g)] in the vicinity of the occlusion.

Figure 13 shows clearly the variability of both the frontal slope and the precipitation regimes in a sample of twenty-four occlusions. The frontal analyses were based primarily on twelve-hourly constant pressure-chart analyses and with twelve-hourly radiosonde and six-hourly rawinsonde data on the time sections. The serial ascent cases presented in Chapter IV demonstrate that frontal analyses based on conventional data are subject to uncertainties. Even after allowance is made for analysis uncertainties, the tremendous variability in both the frontal configuration and the precipitation regimes in this sample makes the construction of a 'model' relationship between occlusions and precipitation appear useless.

Upon observing the large variability in the precipitation structure (and also the cloud structure) of occlusions, an examination was made of each individual storm to determine the reasons for its particular cloud and precipitation structure. Such factors as the source, stage of development, and direction of movement of the front, as well as topographical effects, were examined to see if the type of cloud and precipitation structure could be correlated with these factors in addition to frontal position. These attempts to reduce the variability by subclassifying the fronts were surprisingly unsuccessful. Fronts with similar histories and tracks would often have as much difference in cloud and precipitation structure as between two fronts chosen at random.

These statements are not to be taken as a suggestion that there exists a sort of randomness in cloud and precipitation structure. On the contrary, most of the features have a good explanation. The fact is, though, that a number of factors (not restricted to large scale or topographic factors) contribute significantly to the cloud and precipitation structure of occlusions. These factors will be discussed later in this section. Now, however, the probability of observing a particular cloud and precipitation feature with a single occlusion will be evaluated. This procedure will demonstrate the significance of cloud and precipitation models.

Figure 14 represents a time section through a typical occlusion divided into fourteen regions. The number and shapes of the regions were chosen to permit the most accurate description of the more commonly observed weather features. Each region contains a list of cloud and precipitation features commonly observed in that region. This scheme permits the principal cloud and precipitation features of most occlusions to be expressed as a set of features, one for each region.

Table 7 lists the set of features for each of the twenty-four fronts appearing in Figure 13. The underlined numbers in Figure 14 are the relative frequencies of the features in this sample with the following exception. Fronts 47, 49, 56, 75,

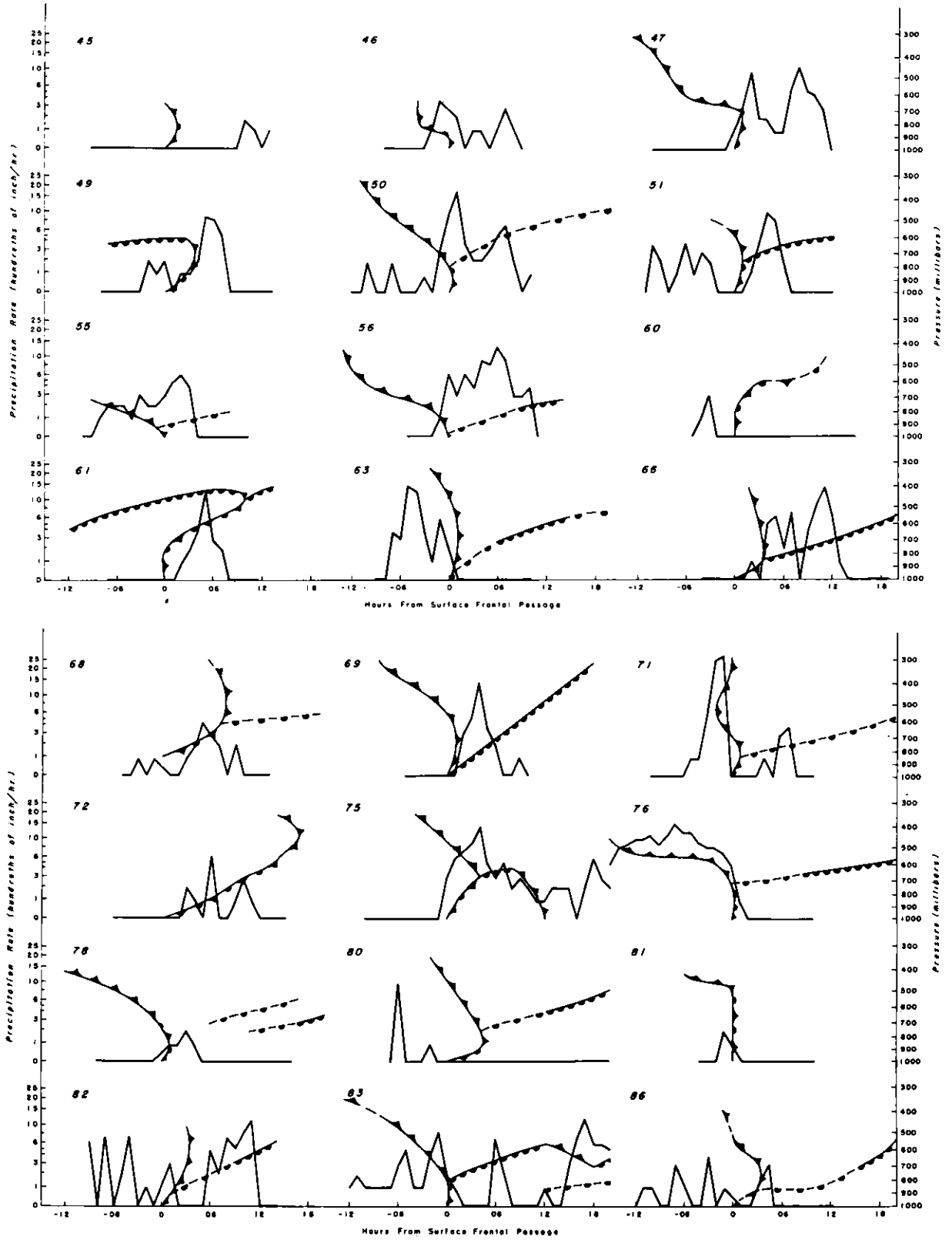

Figure 13. The Variation in Frontal Configurations and Precipitation Rates for Twenty-four Occlusions

TABLE 7. Sets of cloud and precipitation features observed with twenty-four occlusions. 'I' indicates indeterminable and 'N' – not in list of common features. 'N *' indicates not in list of common features because of pre-system complexities.

Front	Region													
	1	2	3	4	5	6	7	8	9	10	11	12	13	14
45	b	a	a	I	I	a	a	a	a	a	a	I	c	b
46	I	I	I	I	I	I	b	a	b	a	a	c	a	a
47	N*	N*	N*	N*	a	a	a	a	a	a	a	c	c	b
49	N*	N*	N*	N*	b	a	a	a	a	b	a	b	a	a
50	b	c	b	I	a	I	a	a	b	a	a	a	a	a
51	b	b	a	a	b	a	b	a	b	b	b	a	a	a
55	b	b	a	a	b	a	a	c	a	a	a	I	I	I
56	N*	N*	N*	N*	N*	a	a	a	a	a	a	I	c	b
60	b	c	b	b	a	c	c	c	I	c	c	b	a	a
61	b	c	b	a	b	N	a	a	a	b	a	b	c	b
63	b	c	b	a	b	b	a	c	b	c	c	a	a	a
66	b	a	a	a	b	b	a	a	a	a	a	c	c	b
68	b	b	b	a	b	b	a	c	a	a	a	b	c	b
69	b	a	a	a	b	a	a	c	a	b	a	c	c	b
71	b	c	c	a	b	I	a	a	I	a	a	c	b	a
72	b	b	a	b	a	c	c	b	b	b	a	b	b	a
75	N*	N*	N*	N*	N*	N*	N*	N*	a	a	a	b	c	b
76	b	a	a	N	N	N	c	c	a	b	b	b	b	a
78	b	c	b	a	b	a	a	a	a	b	a	c	a	a
80	b	b	a	a	b	c	a	c	a	b	c	c	b	c
81	b	a	a	b	a	b	c	c	a	b	c	b	a	a
82	b	b	a	a	b	a	a	a	a	a	a	c	b	a
83	N*	N*	N*	N*	N*	I	a	a	a	a	c	c	b	a
86	a	c	b	b	a	b	c	c	a	b	c	b	b	a

Totals and percentages excluding the I and N* cases

Class	Region													
	1	2	3	4	5	6	7	8	9	10	11	12	13	14
a #	1	5	10	11	6	9	16	13	17	12	16	3	8	14
%	6	28	56	69	32	47	70	57	77	50	67	14	35	61
b #	17	6	7	4	12	5	2	1	5	10	2	9	7	8
%	94	33	39	25	63	26	9	4	23	42	8	43	30	35
c #	00	7	1	00	00	3	5	9	00	2	6	9	8	1
%	00	39	6	00	00	16	22	39	00	8	25	43	35	4
N #	0	0	0	1	1	2	0	0	0	0	0	0	0	0
%	0	0	0	6	5	11	0	0	0	0	0	0	0	0
Total	18	18	18	16	19	19	23	23	22	24	24	21	23	23

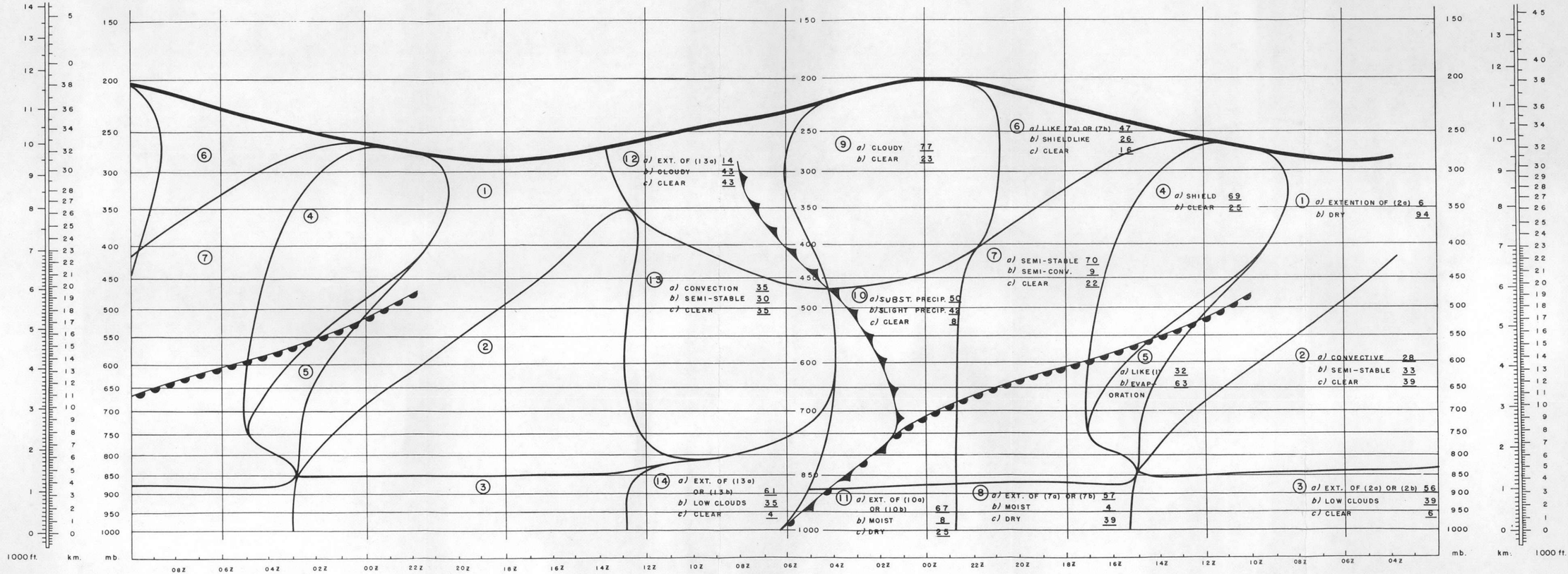

Figure 14. Common Occlusion Cloud and Precipitation Features Represented on a Time Section. Each of the fourteen regions usually has one of the features indicated. The underlined numbers are the percent occurrence.

and 83 were too close to the preceding front or to a decayed system to allow classification of the features in regions 1 through 4, or 5, or 7. These cases have been ignored in the unclassifiable regions. Hence, the underlined numbers in the first seven regions apply only to that 80% of the occlusions which have no major prefrontal complications.

Table 7 and Figure 14 serve two purposes: (1) they provide a summary of the common cloud and precipitation features observed with occluded frontal systems; (2) they indicate the approximate frequency of occurrence of such features. Using the frequencies as probabilities, it is possible to compute the probability of observing any combination of these features which one may wish to propose as a 'model' of the occlusion cloud and precipitation structure.

The following is a brief description of each of the features entered on Figure 14. These are, for the most part, gross features, determined only after a careful examination of synoptic charts and soundings to locate the front on the time section. The radar records, surface observations, and pilot reports were utilized in the cloud analysis.

1. (a) Extension of (2a)

   Convective buildups in (2a) extending to the shield, (4b), before being suppressed.

   (b) Dry

   This dry air may have subsided in the past or may currently be subsiding. The lower boundary of this region is often a subsidence inversion which, when inclined, has the appearance of a warm front in the thermal field on either a time section or a constant pressure chart.

2. (a) Convective

   These showers are commonly referred to as cold air mass showers. The vertical extent of the convection is often progressively suppressed with the approach of either the subsidence inversion (1b) or the cloud shield (4a).

   (b) Semi-stable

   The clouds are either altostratus, nimbostratus, or altocumulus of limited vertical extent.

   (c) Clear

   Cloudfree and usually rather dry with the possible exception of a few fair weather cumulus.

3. (a) Extension of (2a) or (2b)

   The clouds or showers from region (2) extend into region (3).

   (b) Low clouds

   Stratus or stratocumulus in the mixing zone often capped by an inversion. If these clouds exceed 7,000 feet, then (3a) is proper classification.

(c) Clear

The air is cloudfree except for fog or scattered fair weather cumulus.

4. (a) Shield

This class includes the classical cirrus-altostratus sequence or a thickening and lowering cirrus deck. The clouds may be stable or semi-stable.

(b) Clear

Cloudfree except for some thin cirrus or cirrus filaments.

5. (a) Like (1)

Either an extension of dry air or convective buildups depending on conditions in (1).

(b) Evaporation

Whenever both the (1b) and (4a) classifications occur, a zone of evaporating virga with cooling and overturning will separate the two. If the precipitation from the shield is sufficiently strong, mammata clouds and 'stalactites'[30] will be observed.

6. (a) Like (7a) or (7b)

There is no difference between (7) and at least the lowest third of (6).

(b) Shield-like

A thickening and lowering cirrus deck moves in. It may either be the first shield in the storm or a separate additional shield depending on conditions in (4).

(c) Clear

Cloudfree except possibly for some thick cirrus or cirrus filaments.

7. (a) Semi-stable

The cloud forms may be stable or with limited vertical development. The precipitation is often banded and may be in class '1' or '2' in the subjective classification scheme (Table 1).

(b) Semi-convective

Showers and/or convective buildups are observed. Echoes will be in class '2' or '3' and the precipitation rate may be pulsating. There must be direct evidence of the convection, not just fluctuating precipitation rates.

(c) Clear

Cloudfree except for fair weather cumulus or scattered stratus.

8. (a) Extension of (7a) or (7b)

If (7a) or (7b) conditions extend into (8), this classification will be used regardless of the relative humidity. Heavy or moderate surface precipitation will be considered as such an extension regardless of the height of the cloud bases.

(b) Moist

The air is moist but not just an extension of (7a) or (7c). This case includes a moist surface mixing zone separated from (7) by a stable cap.

(c) Dry

The air is relatively dry and able to evaporate a substantial portion of the precipitation falling from (7).

9. (a) Cloudy

The region has substantial amounts of either stable or convective type clouds in a separate layer or continuous with (10).

(b) Clear

Essentially cloudfree but may contain scattered cirrus or some penetration of clouds from (10).

10. (a) Substantial precipitation*

This classification is designed to include active precipitation producing conditions with either free or forced convection.

(b) Slight precipitation

Little precipitation is being produced. Clouds may be either broken or layered, stable or convective.

(c) Clear

Cloudfree except for fair weather cumulus or scattered stratus.

11. (a), (b), and (c)

Identical to (8a), (8b), and (8c) except relative to (10) rather than (7).

12. (a) Extension of (13a)

Convective buildups immediately behind the cold front extend into this region.

(b) Cloudy

This classification is exclusive of (13a) but does include two different cases: the continuation of pre-frontal conditions (9a) and the advection of cirrus from convective buildups upwind. These two cases are difficult to distinguish with the present data.

(c) Clear

Cloudfree except for scattered cirrus.

13. (a) Convection

Convective buildups closely following the cold front.

---

* The extent of precipitation, that is, the selection of (10a) or (10b), is based on radar echo amounts rather than surface precipitation rates.

(b) Semi-stable

Either stable or semi-stable precipitation and/or cloudiness behind the cold front. These conditions may either be a continuation of conditions in (10) or they may have begun just behind the cold front.

(c) Clear

Cloudfree except for fair weather cumulus or scattered stratus.

14. (a) Extension of (13a)

If the convection in (13) extends into (14) in the form of either rain showers at the surface or bases of the convective buildups below 4,000 feet, this classification will apply.

(b) Low clouds

These clouds must be separate from the middle or higher clouds but may extend to 8,000 feet. This classification is intended to include situations where clouds lie beneath a middle level dry or subsidence zone.

(c) Clear

Cloudfree except for fog or fair weather cumulus.

The frequency of occurrence of many of these features can be expected to vary with season and in different climates. For instance, the ratio of pre-frontal to post-frontal cloudiness will be much larger in winter than summer in Seattle; and conditions in the lowest regions, (3), (8), (11), and (14), will be different in maritime than in continental climates. The frequency values themselves are based on a limited sample and are somewhat uncertain. It is believed, however, that the principal implications of Figure 14 are independent of the exact values of these frequencies.

Consider the probability of a frontal system having a particular set of features. The following probability notation will be used. If A and B are events: (A)(B) means A and B both occur, (A+B) means A and/or B occur, p(A) means the probability of event A occurring, and $p(A)_B$ means the probability of A given that event B has occurred. The correlated probabilities, $p(A)_B$ will be estimated from Table 7 in the following examples.* These examples will vary in the extent to which a particular structure is specified. Remember that these probabilities apply only to occlusions with no pre-system complexities. The probabilities listed are higher than if one were to consider an arbitrary occlusion.

Example I - a broadly defined structure.

$I \equiv$ (1b) (2a + 2c) (4a) (7a) (10a + 10b) (13c) .

$p(A) = p(1b) = 0.94;$

* Recall that: $p(A)(B) = p(A)\, p(B)_A$

$$p(B) \equiv p(A)\, p(2a + 2c)_A = 0.94(0.67);$$

$$p(C) \equiv p(B)\, p(4a)_B = 0.63\ (0.73);$$

$$p(D) \equiv p(C)\, p(7a)_C = 0.46\ (0.91);$$

$$p(E) \equiv p(D)\, p(10a + 10b)_D = 0.42\ (0.94);$$

$$p(F) \equiv p(E)\, p(13c)_E = 0.39\ (0.35)\ .$$

$$\therefore\ p(I) = p(F) = 0.138\ ,$$

or about 14% of the occlusions without pre-frontal complexities have the features defined by I.

Example II – a warm-type occlusion structure as described by Bergeron,[4] supposedly common on the west coast of continents in winter.

$$II \equiv (1b)\ (2a + 2c)\ (4a)\ (6c)\ (7a)\ (9b)\ (10a + 10b)\ (13c)\ (14b + 14c)\ .$$

$$p(II) = (0.94)\ (0.67)\ (0.73)\ (0.16)\ (0.91)\ (0.23)\ (0.94)\ (0.35)\ (1.00) = 0.00508\ .$$

Therefore the frequency of this structure is about 0.5%. Evidently the occlusions in Table 7 tend to have much more upper level cloudiness than was specified by Bergeron[4] for a warm-type occlusion.

Example III – the most probable structure with a feature specified in each region.

$$III \equiv (1b)\ (2c)\ (3b)\ (4a)\ (5b)\ (6a)\ (7a)\ (8a)\ (9a)\ (10a)\ (11a)\ (12b \text{ or } 12c)\ (13c)\ (14b)\ .$$

$$p(III) = (0.94)(0.39)(0.86)(0.94)(1.00)(0.47)(0.80)(0.69)(0.89)(0.66)(0.89)(0.43)\ (0.35)(1.00) = 0.00607\ .$$

About 0.6% of occlusions without pre-frontal complexities have the most probable cloud and precipitation structure with a feature specified in each region.

Figure 15 illustrates the conditions specified in each of the three cases. The examples demonstrate that, while some features commonly occur and the correlations between many of the features are good, any very specific model of occlusion

cloud and precipitation features is seldom observed in nature. On the basis of this study the 'model' presented in Example III is the most probable set of cloud and precipitation features and can be expected once in every 165 cases. One is forced to conclude that such a model represents neither a probable nor a common structure but only an example illustrating possible features. One must examine the factors which influence the occurrence of the individual features in the cloud and precipitation structure of occlusions. By considering the pertinent factors in each case, one may formulate the set of features to be expected in a particular case. This study lends support to the concern expressed by Sutcliffe[5] that the use (or misuse) of models can lead a forecaster to jump to unwarranted conclusions without properly using the available data.

The cloud and precipitation models presented to date[2, 20, 21] provide excellent examples of what nature can do. These models should be treated as examples, and the factors important in these examples should be studied. Models based on the averaged conditions may be invaluable in studies which deal with mean conditions. However, these models are taught to pilots as conditions to be expected in frontal regions, and a knowledge of such 'expected conditions' is required for the issuance of pilot licenses by the Federal Aviation Administration. The fact that the expectancy of such models may be less than 20% and for very specific models, less than 1%, is not mentioned. The preponderance in meteorological literature of models of averages avoids the difficulties and complexities involved in the specification of variability, but it can be extremely misleading.

6.2 Processes and Factors Important in Determining Cloud and Precipitation Features

This study has shown that a large variety exists in the cloud and precipitation structure of occlusions, and suggests that a number of factors have an important influence on weather patterns. Also, the extent of the influence of a particular factor can be expected to vary from storm to storm. It is the purpose of this section to review the factors and processes which are important in determining the cloud and precipitation structure of occlusions. This discussion pertains only to the meso- and synoptic-scales of processes and weather features.

The primary factors which determine cloud formation are the initial moisture content and subsequent vertical displacements. In addition, horizontal advection and its variation with height greatly influence the cloud and precipitation patterns of storms by advection and deformation.[51] Precipitation formation is largely dependent upon the sustained ascent of saturated air while the rate of condensation also depends upon the vertical lapse rate of saturated mixing ratio and, hence, temperature.

EXAMPLE I. A PROBABLE MODEL SPECIFYING CONDITIONS IN SIX REGIONS
FREQUENCY IS 14 %

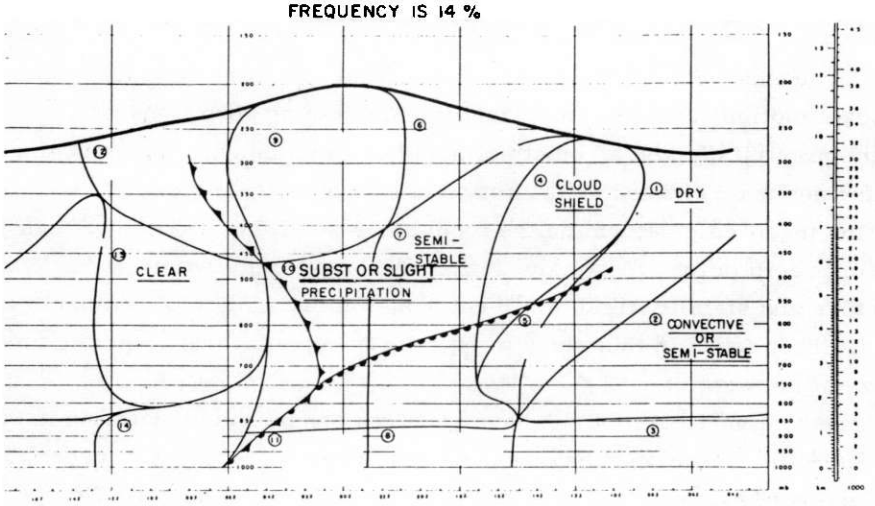

EXAMPLE II. CLASSICAL OCCLUSION MODEL SPECIFYING CONDITIONS IN NINE REGIONS FREQUENCY IS 0.5 %

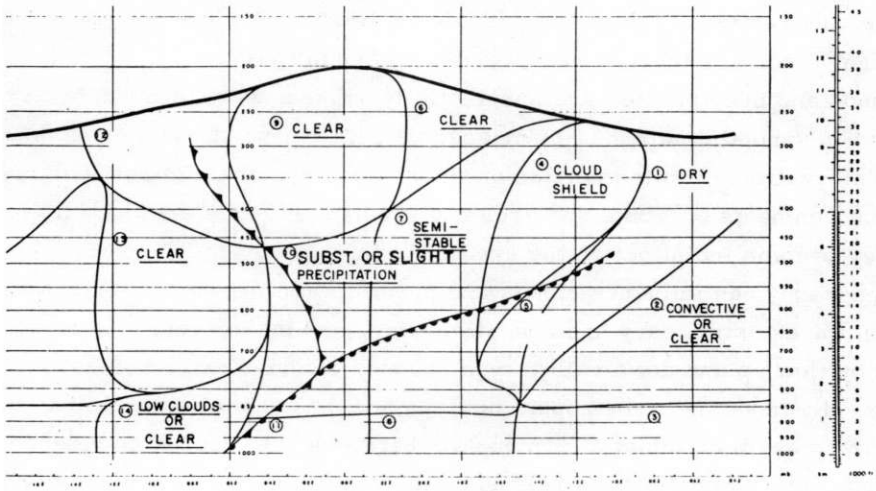

EXAMPLE III. MOST PROBABLE MODEL SPECIFYING CONDITIONS IN ALL FOURTEEN REGIONS. FREQUENCY IS 0.6 %

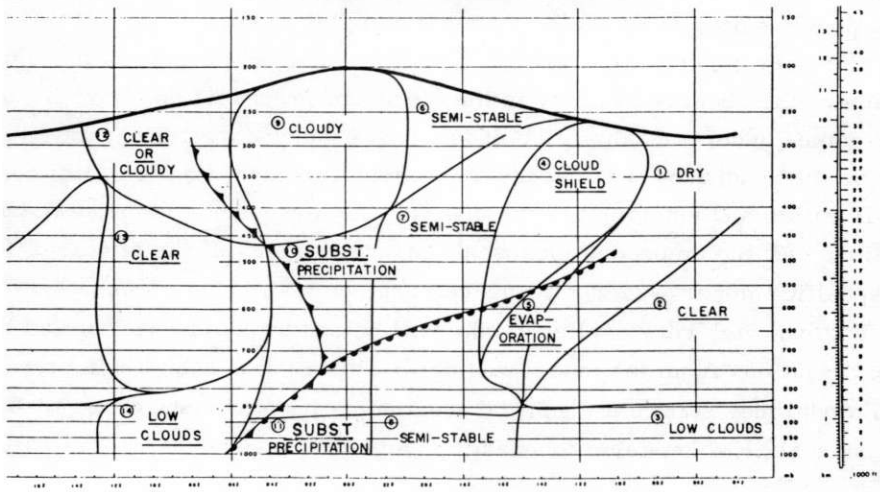

Figure 15. Frequencies of Various 'Models' of the Cloud and Precipitation Structure of Occlusions

The large-scale flow includes small but often sustained vertical motions. Large-scale motions are also important in establishing conditions which lead to clouds and precipitation on a variety of scales. For instance, potential instability may be formed and released by the action of synoptic-scale motions, but circulations on the mesoscale determine the form and size of the resulting clouds and the rate of precipitation. Also, the action of one synoptic feature in establishing the moisture and stability field of air entering the circulation of another synoptic feature has been found in this study to be very important in determining the weather in the downwind system.

Large-scale vertical motions have received considerable attention in recent years. Sutcliffe[52] developed expressions which reveal relations between the thermal and vertical-motion fields in a simple large-scale model. Numerical techniques, based on a more elaborate model, are used routinely to produce analyses and forecasts of large-scale vertical motions in the middle troposphere. However, the patterns of even large-scale vertical motion are neither constant with height[53] nor are they uniquely related to frontal position.

Clouds and precipitation are substantially influenced by mesoscale circulations imbedded in synoptic patterns. A mesoscale cell or line structure can dominate the weather within a limited portion of an occluded cyclone. In particular, it was found that remnants of fronts and cyclones greatly influence the cloud field long after they become indistinct on the synoptic-scale.

Topography can influence clouds and precipitation in many and complex ways. Mountain waves, stationary and non-stationary, and the convergence or divergence induced by flow up and down valleys can produce clearing or cloudiness and instability. By inducing ageostrophic motions and differential advection of cold or dry air over warm or moist air, mountain barriers can lead to the release of instability. Once instability is released, the resulting circulation and vorticity production can, in themselves, induce additional convection (Ref. 54 , p. 154). This study, in a region of complex topography and using mainly single-station data, is poorly suited to evaluate this most complex factor.

After reviewing only the more important factors and processes that influence the weather, the observed variety in the cloud and precipitation structure of occlusions becomes understandable. To understand observed weather features or to predict future conditions it is necessary to first consider: (1) the initial condition of the air within and entering the cyclone, (2) the large-scale horizontal and vertical motions, (3) the embedded mesoscale structures and (4) the effects of topography.

A specific 'model' weather sequence requires a specific combination of producing factors. Any very explicit model will be observed only rarely and the importance of deviations from the model will depend upon the problem being treated. A general model may suffice for general treatments but when concerned with a particular storm, such as in short-term forecasting, any general model is of very limited value.

7. SUMMARY AND CONCLUSIONS

7.1 Usefulness of Techniques

The APQ-39 vertically-directed radar at a wavelength of 1.87 cm provides a continuous THI (time-versus-height) record of the precipitation structure. Few, if any, non-precipitating clouds are detected. Whenever cirrus is observed, it is believed that significant amounts of precipitating crystals are present. The THI data very conveniently depict the major precipitation features of storms. The compactness of the data allows many systems to be examined subjectively to determine the similarities and differences in their precipitation structures.

The vertically-directed radar, even with short-interval radiosonde ascents, is inadequate for studying the microscale physics of precipitation. Additional tools, such as RHI-radar to determine horizontal advection effects and doppler radar to determine precipitation fall velocities, are necessary to observe adequately the complex cloud and precipitation growth mechanisms.

The radiosonde serial-ascent program provided information on the mesoscale structure of fronts. These data establish the fact that the mesoscale structures are too complex to be inferred from the conventional radiosonde network. A single time section will not reveal the spatial structure of a frontal system such as could be determined from simultaneous serial ascents from several stations. The data obtained only indicate some of the types of possible mesoscale features which are located in frontal regions, but these features have important implications in frontal theory and synoptic frontal analysis.

The single-station vertical-velocity computations are necessarily rather laborious, but they are well worth the effort. The simplifications which are required do not destroy the usefulness of the method. Significant vertical-motion patterns can be determined which are very valuable in view of the limited availability of such information. The sensitivity of the equations necessitates several precautions. The most suitable averaging techniques must be used, and the computational errors must be eliminated by use of electronic computers. The uncertainties of each vertical velocity should be computed to allow proper weighting to be given each value in the analysis of the field and to indicate the confidence which can be placed in the resulting patterns. The acceleration term arising from vertical displacements in a shearing fluid should be retained even if only by an approximate technique. This latter factor can be very important, and one should determine those regions in which it is important.

The static energy ($\sigma \equiv gz + c_{pd} + L_0 m$) was found to be very useful in interpreting the serial-ascent data and in qualitatively evaluating the effects of mixing in frontal regions. The static-energy field depicts the stability and potential

instability distribution, regions of large baroclinity or horizontal moisture gradients, and regions in which mixing is likely to be important in frontolysis or frontogenesis. For studies dealing with mesoscale structures and pseudo-adiabatic, as well as mixing processes, the static energy function is an important interpretation aid.

7.2 Structure of Occlusions

The serial-ascent case studies provided information on the mesoscale thermal, static-energy, and vertical-motion fields in a limited number of frontal systems. This information, along with the results of previous investigations as reported in the literature, provides the basis for conclusions on certain mesoscale aspects of frontal structure. These mesoscale features have important implications in the interpretation and use of synoptic analyses but do not suggest radical changes in conventional analysis techniques. The second phase of the study utilizes the radar records from a large number of occlusions for which only synoptic soundings are available. The frequency of occurrence of certain cloud and precipitation features in occlusions has been determined for a reasonably large sample (twenty-four cases) of relatively unambiguous occlusions. The frequencies demonstrate the weaknesses of dealing with average models and the importance of studying individual features and their frequency of occurrence.

7.2.1 MESOSCALE STRUCTURE

Mesoscale analyses of frontal zones indicate that they are normally comprised of multiple subzones* of intense baroclinity or static stability. The subzones are either leafed together or separated by narrow, more homogeneous or barotropic layers. The warm frontal zones are particularly laminated. A warm front, placed at the warm edge of the transition zone, rarely bounds the same mesoscale subzone at both low and middle levels. The static energy function has been used to aid in the interpretation of the mesoscale subzones.

The limited number of serial ascent cases indicates two different types of occluded frontal structures. The newly occluded systems have distinct occluded fronts extending nearly vertically to the surface. These vertical frontal zones have little static stability. The occluded structure in the older systems represents a quasi-horizontal extension of the warm frontal stable zone. Upon passage of the elevated cold front, the warm frontal zone is continually eroded away without ever reaching the lowest levels. Abrupt changes at the surface in these cases occur only with passage of a secondary cold front.

---

* Figure 11 illustrates the meaning of the frontal zone terminology used herein.

The relation of frontal slope to the static stability on either side of the occluded front has two important implications. The slope of the occlusion is not necessarily related to the relative coolness of the preceding and following air masses, particularly where pre- or post-frontal secondary features are present. One can also see that frontal slope can change rapidly under the influence of stability advections, particularly in the lowest layers.

The elevated cold fronts in occluded systems vary both in intensity and in the configuration of the leafed or multiple-layered mesoscale structure. A case with a rather broad and disorganized cold frontal zone was found to maintain synoptic continuity for a period of twenty-six days. This fact suggests that the synoptic structure, rather than the mesoscale details, is responsible for the long-term continuity (on the synoptic scale) of frontal systems.

The steep occluded and cold frontal zones appear to be susceptible to division into minor subzones or diffusion into broad transition zones. In cases in which intense subzones are separated from the principle frontal zones, the separated subzones may produce pre-frontal rain bands, squall lines, post-frontal rain bands, or secondary cold fronts. Of the mechanisms which are capable of dividing steep frontal zones, convective mixing associated with the release of potential instability appears to be of significant importance.

The mesoscale vertical motions in the serial-ascent cases are much more varied, complex, and less well correlated to frontal position than the classical models imply. The observations are more nearly comparable to the recent models of Eliassen[47] which indicate a direct circulation within the frontal zone. Rising motion continues after passage of the cold front in the warmer portion of the transition zone.

A region of subsidence is shown in several cases to separate the warm frontal cloud shield from a higher region of ascent and cirrus above 400 mb. A subsidence region is also found in several cases to extend from high levels behind the cold front forward and downward to about 600 mb ahead of the cold front.

The occluded fronts in the case studies are invariably surrounded by ascending air. This vertical-motion field can prevent a quasi-horizontal warm-type occlusion from intersecting the surface and can be influential in releasing potential instability near the occlusion. The convection can divide the frontal zone into separate minor zones or erode and destroy a quasi-horizontal stable zone such as is found in older occlusions.

7.2.2 IMPLICATIONS OF THE MESOSCALE STRUCTURES IN SYNOPTIC ANALYSIS

The complexities in the mesoscale structures raise the question of the significance of synoptic frontal analysis using conventional techniques. The synoptic

data are unable to resolve the mesoscale details, but these details do complicate the interpretation of observations such as individual soundings. Sounding data must be smoothed in the vertical to correspond with the horizontal and temporal smoothing necessitated by the spacing of synoptic soundings.

The principal features in the mesoscale field can be approximately located by the somewhat arbitrary but useful technique of 'de-smoothing' the data to emphasize the baroclinity in specific zones. The 'de-smoothed' analysis, obtained by concentrating the baroclinity in certain regions, does not accurately depict the mesoscale hyperbaroclinic zones, since such features cannot be resolved with synoptic data.

Since a synoptic frontal analysis is a somewhat artificial construction or simplified model, certain analysis problems must be treated in an arbitrary manner. For instance, in the absence of an 'identifiable' warm front, the analyst must establish a criterion for determining the point of occlusion – the point beyond which a cold front becomes an occluded front. There is no physical reason to rule out either the formation of an occlusion in the absence of an identifiable warm front nor the conversion of a portion of an occlusion back into a cold front. The number of air masses or fronts in the atmosphere varies with season and region. The specification of a fixed number of synoptic fronts between the tropics and the poles is an operational decision, to which nature is not bound.

7.2.3 FREQUENCY OF CLOUD AND PRECIPITATION FEATURES

The relations between: (1) frontal position, structure, and intensity and (2) clouds and precipitation are of fundamental importance in the application of frontal concepts. This study has utilized THI-radar records from twenty-four relatively unambiguous occlusions selected from about one hundred frontal systems to examine the front-weather relationships in occluded cyclones. The results are conclusive but disappointing in that consistent relationships were found to be lacking. A large variation was observed in cloud and precipitation features both within a single storm and between occlusions with similar synoptic features. This variability was not greatly reduced by grouping into classes of storms with similar histories or at similar stages of development.

The classical models of weather in the vicinity of fronts[2] as well as the more recent radar and satellite models[20, 21] appear to be as good as can be formulated on a general basis. If one were to take the average of many cases, these models would be verified. It is extremely important to emphasize, however, that the probability of a particular occlusion having the classical cloud and precipitation structure is very small. The more specific and detailed the model is, the less frequently it will be observed. Computations based on our observations show that even for a broadly defined model the expected frequency is 14%. For a model

specifying conditions fairly explicitly throughout a cross section of the occlusion, the most probable model will occur in only 0.6% of the cases.

The only realistic uses of model relations appear to be: (1) when dealing with the average of many storms, such as in climatological studies or (2) as examples of conditions which occur in nature. Examples showing results of nature's mechanisms are certainly useful, but a particular example, even if it is the most frequent example, cannot be presented as a common situation if it has a frequency of only a few percent. When forced to deal with a particular occlusion, the forecaster or forecast user (such as a pilot) should not assume a model (but rarely found) structure from which deviations are to be predicted on the basis of current observations. The more logical approach is to examine the factors which contribute significantly to the cloud and precipitation features in each section of the storm. Once the data relevant to each factor have been examined, the most probable conditions within the particular storm can be determined.

7.2.4 PROCESSES AND FACTORS IMPORTANT IN DETERMINING CLOUD AND PRECIPITATION FEATURES

The long wave patterns influence the displacement of the synoptic-scale systems but contribute only a minor component to the vertical-motion field. The synoptic features surrounding an occluded cyclone prepare the initial conditions of moisture, stability, and baroclinity of the air entering the circulation of the cyclone. The patterns downstream from the occlusion are responsible for the preservation or destruction of the cloudiness produced in the cyclone. The initial moisture and stability structure of air entering the cyclonic flow is very influential in determining the cloud and precipitation structure of the occlusion and contributes greatly to its variability.

The baroclinic structure of the cyclone, through the thermal wind relation and Sutcliffe's principles, is largely responsible for the synoptic-scale vertical-motion field. These vertical motions contribute to the formation of clouds, and the horizontal advections distribute the clouds. Small-magnitude, large-scale vertical motions are also important in altering the stability field and in releasing potential instability. Precipitation at moderate or heavy rates is dependent upon the higher-magnitude mesoscale vertical motions which the synoptic patterns influence only indirectly.

Clouds and precipitation are greatly influenced by circulations and structures not directly detectable from synoptic observations. Fronts or circulations, either too young or too old and diffuse to be detected in a synoptic analysis, can dominate the cloud and precipitation fields in their area. Cells and lines of clouds and precipitation exist on the mesoscale and propagate somewhat independently of the synoptic scale motions.[55]

The influence of topography on cloud and precipitation formation varies from region to region but is extremely important in all land areas. The influence exerted by topography depends upon the direction, speed, and vertical shear of the flow as well as the stability and moisture structure of the air.

The following factors contribute to the variability of the cloud and precipitation structure of occlusions: the effects of mesoscale circulations, topography, and the moisture and stability structure of the air entering the circulation. The life cycle of the occlusion itself will alter, in time, the weather associated with the cyclone. The importance of such a variety of variable factors eliminates hope of a simple, accurate, and general description of the relation of clouds and precipitation to occlusions.

7.3 Suggestions for Further Research

The results of this study suggest that the general structure of fronts and the associated weather can be formulated only as a framework to which a variety of features can be attached. Models of the particular features need both observational and theoretical investigation to reveal the influence of individual and combined factors. Rather than studying the average structure, the variety and variability of the ways in which nature combines the features should be examined. The successful treatment of such complex systems requires the correlation of the features, on a physical basis, to factors which are more easily observed.

A study of variability requires the collection of a large sample. A large sample of storms can be adequately analyzed and compared only by automated and, at least, semi-objective means. The development of objective analyses is important, for they insure a certain degree of internal consistency and allow large samples to be examined statistically.

The complexity of the structures and the difficulty in observing certain important parameters, such as vertical motions, require the greatest possible combination of observational data including radar and satellite data. The horizontal spacing of soundings which determine the synoptic structure needs six-hourly spacing to maintain adequate continuity for research purposes. Prolonged periods of six-hourly soundings will be extremely useful once researchers are able to reduce the data efficiently.

The mesoscale structure, particularly in the vicinity of frontal systems, must be investigated for a large number of cases. Data from a closely spaced (0030 miles) network of stations releasing radiosondes at hourly intervals would determine the mesoscale thermal, motion, and even vertical-motion patterns. Knowing horizontal gradients, the thermodynamic vertical-motion equation can be solved with accuracy and confidence. Such a program would require electronic data

reduction but would present no serious difficulties. Use of the static energy function as a conservative quantity appears to be very valuable in dealing with precipitating systems.

The successful reproduction of physical processes by numerical experiments provides an effective means of evaluating the effects of certain variables upon subsequent motion. For instance, if one could adequately represent the motion, moisture, and stability fields in a numerical model, the interactions of these fields with various topographic features could be examined. A particular question which deserves attention is what effect do large-scale vertical motions acting on irregular moisture and stability fields have upon the subsequent mesoscale circulations.

No major obstacles remain to the study of frontal structures and processes. Instrumentation, with aircraft, radar, and satellites, has advanced to the point where adequate observations are possible on both the meso- and synoptic-scales. Humidity measurements are the weakest link in observational capabilities. The complexity and variability of conditions in frontal regions require the assimilation of a tremendous amount of data, but electronic devices make proper data processing possible. Current advances in the numerical treatment of non-linear partial differential equations allow theoretical models to be examined and numerical experiments to be performed. We are now in a position to treat the complex but important problems related to frontal structures and processes in a realistic manner.

Appendix A

VERTICAL VELOCITIES COMPUTED FROM SINGLE-STATION DATA

A variation of the 'adiabatic method' of computing vertical velocities has been used with some success in computing large-scale vertical motions using radiosonde data from a single station. The serial-ascent radiosonde data used in this study represent single-station observations on the mesoscale. In this appendix the reliability of the mesoscale vertical motions computed by applying the single-station method to the serial-ascent data will be examined and the appropriate equations will be developed for both the vertical velocities and their uncertainties.

If the adiabatic (or pseudo-adiabatic) temperature change, $dT\big|_A$, is separated from the diabatic change, $dT\big|_D$, then

$$\frac{dT}{dz}\bigg|_A + \frac{dT}{dt}\bigg|_D = \frac{\partial T}{\partial t} + \vec{V}\cdot\vec{\nabla}_z T + w\,\frac{\partial T}{\partial z} \quad .$$

w can be expressed exactly by the equation

$$w = \frac{-\left(\frac{\partial T}{\partial t}\right) - \vec{V}\cdot\vec{\nabla}_z T + \frac{dT}{dt}\Big|_D}{\Gamma - \gamma} \quad , \qquad \text{(A-1)}$$

where

$$\Gamma \equiv - \left.\frac{dT}{dz}\right|_A ; \quad \gamma \equiv - \frac{\partial T}{\partial z} \quad .$$

The serial-ascent data provide measurements of the local temperature change, $\partial T/\partial t$, and the lapse rate, γ . The thermal wind relation allows the advective temperature change, $- \vec{V} \cdot \vec{\nabla}_z T$, to be estimated from the hodograph. Γ is the adiabatic or, if appropriate, the pseudo-adiabatic lapse rate.

In practice $(dT/dt)_D$ is ignored, introducing a negligible error except in cases of strong evaporative cooling. The vertical-velocity equation becomes unreliable for very small values of the denominator, $\Gamma - \gamma$, and becomes indeterminate when Γ equals γ . After examining the implications of using the thermal wind relation to compute the advective temperature change from the hodograph, the questions of reliability and diabatically induced errors will be examined in detail.

1. Evaluation of the Advective Temperature Change

Differentiation with height of the equation of motion will give the complete thermal wind equation and a means of estimating the advective temperature change, $- \vec{V} \cdot \vec{\nabla}_z T$, from the hodograph. An eddy viscosity or 'friction' term will be retained to show its form but will be dropped in the computations since it cannot be evaluated with sufficient accuracy.

The differentiated form of the horizontal equation of motion is

$$\frac{\partial}{\partial z}\left(\frac{d\vec{V}_H}{dt}\right) + f\vec{k} \times \frac{\partial \vec{V}_H}{\partial z} = - g \frac{\partial}{\partial z}(\vec{\nabla}_p z) + \frac{\partial}{\partial z}\left[\frac{\partial}{\partial z}\left(K_m \frac{\partial \vec{V}_H}{\partial z}\right)\right] \qquad (A\text{-}2)$$

where K_m is the eddy diffusivity of momentum. Since for an ideal gas

$$\frac{\partial}{\partial z}\left(\vec{\nabla}_p z\right) = \frac{\partial p}{\partial z} \frac{\partial}{\partial p}\left(\vec{\nabla}_p z\right) = \frac{\vec{\nabla}_z T}{T} + \frac{f}{Tg} \frac{\partial T}{\partial z} \vec{V}_g \times \vec{k} \quad , \qquad (A\text{-}3)$$

the following expression is obtained for the advective temperature change:

$$- \vec{V} \cdot \vec{\nabla}_z T = \frac{T}{g} \vec{V}_H \times \left(\frac{\partial}{\partial z} \frac{d\vec{V}_H}{dt} + f\vec{k} \times \frac{\partial \vec{V}_H}{\partial z}\right) - \frac{T}{g} \vec{V}_H \times \frac{\partial^2}{\partial z^2}\left(K_m \frac{\partial \vec{V}_H}{\partial z}\right)$$

$$+ \frac{f}{g} \frac{\partial T}{\partial z} \vec{V}_H \cdot \vec{V}_g \times \vec{k} .$$

In natural coordinates,

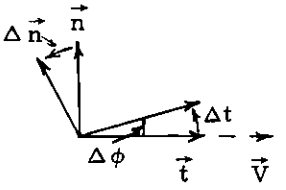

$$d\vec{t} = \vec{n}\, d\phi \; ; \quad d\vec{n} = -\vec{t}\, d\phi \; ;$$

$$\frac{d\vec{V}_H}{dt} = \frac{dV}{dt}\,\vec{t} + V\frac{d\phi}{dt}\,\vec{n} \; ; \quad \frac{\partial \vec{V}_H}{\partial z} = \frac{\partial V}{\partial z}\,\vec{t} + V\frac{\partial \phi}{\partial z}\,\vec{n} \; .$$

From the $\vec{n}$ component of the equation of motion ,

$$V\frac{d\phi}{dt} + \left[f\vec{k}\times\vec{t}\,\left(V - \vec{V}_g\cdot\frac{\vec{V}}{V}\right)\right]\cdot\vec{n} = \vec{n}\cdot\frac{\partial}{\partial z}\,K_m\frac{\partial \vec{V}_H}{\partial z} \; .$$

Hence,

$$\vec{V}_H\cdot\frac{\partial}{\partial z}\left(\frac{d\vec{V}_H}{dt}\right) = \frac{\partial}{\partial z}\left(\vec{V}_H\cdot\frac{d\vec{V}_H}{dt}\right) - \frac{\partial \vec{V}_H}{\partial z}\cdot\frac{d\vec{V}_H}{dt}$$

$$= V\frac{\partial}{\partial z}\left(\frac{dV}{dt}\right) + fV^2\frac{\partial\phi}{\partial z}\left(1 - \frac{\vec{V}\cdot\vec{V}_g}{V^2}\right)$$

$$- V\frac{\partial\phi}{\partial z}\,\vec{n}\cdot\frac{\partial}{\partial z}\left(K_m\frac{\partial \vec{V}_H}{\partial z}\right) \; ,$$

and

$$f\vec{V}_H\cdot\vec{k}\times\frac{\partial \vec{V}_H}{\partial z} = f\vec{k}\cdot\left[V^2\frac{\partial\phi}{\partial z}\,\vec{n}\times\vec{t}\right] = -fV^2\frac{\partial\phi}{\partial z} \; .$$

The advective temperature change can now be written as

$$-\vec{V}\cdot\vec{\nabla}_z T = \frac{T}{g}\left[V\frac{\partial}{\partial z}\left(\frac{dV}{dt}\right) - fV^2\frac{\partial\phi}{\partial z}\left(\frac{\vec{V}\cdot\vec{V}_g}{V^2}\right)\right] + \frac{f}{g}\frac{\partial T}{\partial z}\,\vec{V}_H\cdot\vec{V}_g\times\vec{k}$$

$$- \frac{TV}{g}\left[\vec{t}\cdot\left(\frac{\partial^2}{\partial z^2}\,K_m\frac{\partial \vec{V}_H}{\partial z}\right) + \vec{n}\cdot\frac{\partial\phi}{\partial z}\,\frac{\partial}{\partial z}\left(K_m\frac{\partial \vec{V}_H}{\partial z}\right)\right] . \qquad \text{(A-5)}$$

The last term in the above expression represents the effect of eddy stresses in causing the true wind shear to differ from the geostrophic thermal wind. This effect can be expected to be largest near the surface but can be found wherever

$K_m \partial \vec{V}_H / \partial z$ varies with height. Uncertainties as to the $K_m(z)$ -relation and inaccuracies in measuring the higher order derivatives in the velocity make computed values of this term meaningless. In the remainder of this study, the frictional or eddy stress effects will be included qualitatively only.*

Neglecting only friction and the negligible differences between $\vec{V} \cdot \vec{\nabla}_p T$ and $\vec{V} \cdot \vec{\nabla}_z T$, namely $\frac{f}{g} \frac{\partial T}{\partial z} \vec{V}_H \cdot V_g \times \vec{k}$, the advective temperature change becomes

$$- \vec{V} \cdot \vec{\nabla}_z T = - \frac{fTV^2}{g} \frac{\partial \phi}{\partial z} \left(\frac{\vec{V} \cdot \vec{V}_g}{V^2} \right) + \frac{TV}{g} \frac{\partial}{\partial z} \left(\frac{dV}{dt} \right) . \qquad \text{(A-6)}$$

This equation expresses the effect which the variation of ageostrophic wind with height has on the computation of advective temperature changes. This effect is contained in the term $\frac{TV}{g} \frac{\partial}{\partial z} \left(\frac{dV}{dt} \right)$ and the factor $\frac{\vec{V} \cdot \vec{V}_g}{V^2}$.

The factor, $\frac{\vec{V} \cdot \vec{V}_g}{V^2}$, cannot be computed for the serial-ascent cases and will be assumed to be unity with deviations in magnitude considered qualitatively. During gradient flow this assumption will result in the overestimation (underestimation) of the advective temperature change in a trough (ridge). Under supergeostrophic decelerating flow, the advective temperature change will also be overestimated. For subgeostrophic, accelerating flow, which is often encountered ahead of a front at low levels, $\vec{V}_g \cdot \vec{V} \approx V^2$ and the assumption that $(\vec{V}_g \cdot \vec{V})/V^2 = 1$ is satisfactory.

While the effect in Equation (A-6) of the vertical gradient of the speed acceleration cannot be computed exactly from the serial-ascent data, it can be closely approximated by ACC , where

$$\text{ACC} \equiv \frac{TV}{g} \frac{\partial}{\partial z} \left(w \frac{\partial V}{\partial z} \right) \approx \frac{TV}{g} \frac{\partial}{\partial z} \left(\frac{dV}{dt} \right) . \qquad \text{(A-7)}$$

The horizontal advection and local-change terms which are neglected are usually negligibly small and are probably negatively correlated. The retained term, ACC , can be significant in nature and its retention will prevent the computation of fictitiously large values of $\partial w / \partial z$.

With the above approximations in the acceleration factor and term, Equation (A-6) becomes

---

* It may be possible to use Equations (A-1) and (A-5) to evaluate $K_m(z)$ under ideal conditions, with very accurate wind observations, and with an independent evaluation of the vertical velocity.

$$- \vec{V} \cdot \vec{\nabla}_z T = - \frac{fTV^2}{g} \frac{\partial \phi}{\partial z} + ACC \ . \qquad (A-8)$$

To obtain this equation, friction and the minor difference between $\vec{V} \cdot \vec{\nabla}_z T$ and $\vec{V} \cdot \vec{\nabla}_p T$ as well as the term $\frac{TV}{g} \frac{\partial}{\partial z} \left(\frac{\partial V}{\partial t} + \vec{V} \cdot \vec{\nabla}_z V \right)$ have been neglected and $(\vec{V} \cdot \vec{V}_g) / V^2$ has been taken to be unity. Of these approximations only the neglect of friction appears to be significant. The further neglect of ACC gives the usual approximation to the advective temperature change, namely

$$ADV = - \frac{fTV^2}{g} \frac{\partial \phi}{\partial z} \approx - \vec{V} \cdot \vec{\nabla}_z T \ . \qquad (A-9)$$

This latter equation follows directly from Equation (A-6) if the variation of the ageostrophic wind with height is assumed to be zero.

2. Computation of the Vertical Velocities

The vertical velocities are obtained primarily from the equation

$$w = \frac{- \frac{\partial T}{\partial z} + ADV}{\Gamma - \gamma} \ , \qquad (A-10)$$

which is obtained from Equation (A-1) and Equation (A-9) by omission of the diabatic temperature change, $(dT / dt)_D$. Since ACC involves the vertical derivative of w and of the wind shear, a differential equation must be solved if ACC is to be retained. The resulting differential equation is unsatisfactory because observational errors will introduce progressively larger errors as one integrates further from the boundary condition. To circumvent this difficulty, a first approximation to the w-profile is obtained from Equation (A-10). Using this approximate solution to provide frequent boundary conditions, one can integrate the more complete equation through short thicknesses to see if the first approximations are consistent with the more complete solution. In this manner, the ACC term provides a consistency check on the approximation, Equation (A-10). This procedure will be discussed in detail later in this section.

The principal input for the w-computations using Equation (A-10) is the temperature, adiabatic lapse rate, moist adiabatic lapse rate, and the approximate temperature advection, ADV . The input quantities are 50-mb averages computed

by the IBM 709 from radiosonde data at particular levels.* The vertical averaging serves three important functions: (1) it is consistent with computation of vertical derivatives using finite differences over 50-mb layers; (2) it limits the amount of input and output data to seventeen levels; (3) the data are arranged by constant pressure levels, allowing the local-temperature change in Equation (A-10) to be easily computed. The local-temperature change is obtained by using the three-point finite difference equation,

$$\left.\frac{\partial T}{\partial t}\right|_0 = \frac{T_{+1} - T_0}{t_{+1} - t_0}\,\frac{t_0 - t_{-1}}{t_{+1} - t_{-1}} + \frac{T_0 - T_{-1}}{t_0 - t_{-1}}\,\frac{t_{+1} - t_0}{t_{+1} - t_{-1}} \qquad \text{(A-11)}$$

The subscripts, 0, -1, and +1 refer to the central, preceding, and subsequent soundings, respectively.

The vertical velocity is computed using both the dry and moist adiabatic lapse rates for Γ, giving values of w_{DRY} and w_{SAT}, respectively. w_{SAT} is selected by the computer as being appropriate only if three conditions are met: (1) the relative humidity with respect to ice is at least 90%; (2) the lapse rate, γ, is absolutely stable; (3) w_{SAT} is positive. Unless these conditions are met, w_{DRY} is deemed appropriate. If condition (1) is met, but either (2) or (3) fails, a note to that effect is listed by the computer on the output sheet.

The next step in the computation is the determination of the reliability of each vertical-velocity computation and a re-evaluation of the unreliable values. The formulae used to determine the uncertainty in the vertical velocity will be developed in a final section of this appendix. If the computed uncertainty is found to exceed both 3 cm/sec and the magnitude of the velocity itself, this vertical velocity is deemed unreliable. A new value is computed by vertical interpolation between the nearest reliable vertical velocities. Assuming independence in the uncertainties of the values between which the interpolation is made, a new uncertainty is computed for the interpolated vertical velocity. If the lowest (1000-950 mb) or the highest (200-150 mb) layer is found to have an unreliable vertical velocity, the value is set to zero, and the uncertainty is assigned to 3 cm/sec. Whenever the vertical velocity is determined by vertical interpolation or set to zero, a note to that effect is entered by the IBM 709 on the output.

At this stage, vertical velocities of reasonable reliability have been computed for each 50-mb layer of each sounding. The values are next averaged horizontally using the three-point running-mean equation,

$$\bar{w}_0 = \frac{w_0 + w_1}{2}\,\frac{t_0 - t_{-1}}{t_1 - t_{-1}} + \frac{w_{-1} + w_0}{2}\,\frac{t_1 - t_0}{t_1 - t_{-1}} \qquad \text{(A-12)}$$

* For the serial ascent cases these levels were at intervals of 30-seconds for soundings taken at UW and 1-minute for the SEA soundings

The subscripts $0, -1, 1$ refer to the central, previous, and subsequent soundings. The uncertainty of these averaged vertical velocities is computed assuming independence of the uncertainties in w_0, w_{-1}, and w_1.

A 'quality' is then assigned to each of the averaged vertical velocities depending upon its reliability. The criteria selected are:

Good: $\delta\overline{w} < \overline{w}/2$

Fair: $\overline{w}/2 \leq \delta\overline{w} \leq \overline{w}$

Close: $\overline{w} < \delta\overline{w} \leq 3$ cm/sec

Bad: $\delta\overline{w} > \overline{w}$ and $\delta\overline{w} > 3$ cm/sec .

By printing the quality beside the vertical velocity, one can easily scan the output and determine the reliability of the values.

3. Treatment of the Acceleration Term, ACC

To this point the acceleration term in the advective temperature change equation (A-8) has been neglected. Combining Equations (A-1) and (A-8), we have

$$w = \frac{-\frac{\partial T}{\partial t} + ADV + \frac{TV}{g}\frac{\partial}{\partial z}\left(w\frac{\partial V}{\partial z}\right)}{\Gamma - \gamma} . \qquad (A-13)$$

Defining

$$ON \equiv -\frac{\partial T}{\partial t} + ADV ; \; S \equiv \Gamma - \gamma ; \; C \equiv \frac{TV}{g} , \qquad (A-14)$$

we have the differential equation

$$\frac{C\frac{\partial V}{\partial z}\,dw}{\left(C\frac{\partial^2 V}{\partial z^2} - S\right)w + ON} + dz = 0 . \qquad (A-15)$$

By integrating over 50-mb layers while using the mean values of the coefficients as constants, we have

$$w_{1U} = w_0 \exp\left(\alpha_U\right) + \beta_U\left[\exp\left(\alpha_U\right) - 1\right] , \qquad (A-16)$$

and

$$w_{1D} = w_2 \exp(\alpha_U) + \beta_U \left[\exp(-\alpha_D) - 1\right] \qquad \text{(A-17)}$$

where

$$\alpha \equiv \left(\frac{-\Delta z \left(C \frac{\partial^2 V}{\partial z^2} \right) - S}{C \frac{\partial V}{\partial z}} \right), \qquad \beta \equiv \frac{ON}{C \frac{\partial^2 V}{\partial z^2} - S}, \qquad \text{(A-18)}$$

and Δz is the thickness of the 50-mb layer. The subscripts U and D on α and β indicate that these constants are the appropriate averages for the integration up to (U) level '1' from level '0' or down to (D) level '1' from level '2'. The boundary conditions, w_0 and w_1 are taken to be the mean vertical velocities from Equation (A-12).

The previous paragraph indicates how one can use the values of w computed without the acceleration term as boundary conditions for integrations of the more complete expression over 50-mb thicknesses upward and downward. If the acceleration term has a negligible effect, the integrated values will be consistent with the initial values, that is, $(w_{1U} + w_{1D}) / 2$, will be nearly equal to $\overline{w}_0$ from Equation (A-12). If inconsistencies are present, a second approximation, $w_1 \equiv \frac{w_{1U} + w_{1D} + 2\overline{w}_0}{4}$, can be computed. These new values can be used as boundary conditions in another set of integrations, making a further check of consistency.

The computer performed such successive integrations through ten cycles. When the coefficients α and β were first computed, tests were made to prevent the use of unreasonable values. Nevertheless, the successive integrations often did not converge but would oscillate and/or become unstable. It is, however, possible to determine from the first few integrations whether or not the initial vertical velocities are consistent with values computed from the more complete expression. If inconsistencies are present, the sign and the general magnitude of the error can be estimated.

The effect of accelerations on the expression for the advective temperature change can be handled only crudely and only with difficulty. It is believed that this crude correction and consistency check is of value, for it explains some tremendous values of $\partial w / \partial z$ which would be obtained in regions of strong $\partial V / \partial z$ if ACC were to be neglected entirely.

4. Computation of the Uncertainty in the Vertical Velocities

The reliability of vertical velocities computed by the single-station adiabatic method varies considerably from point to point. A knowledge of the reliability at each point is extremely useful, if not necessary, for the proper analysis of the field of values. It is found that, while some values are unreliable, enough reliable values are computed to allow a reasonable analysis. The unreliable values can be disregarded.

The uncertainty in the vertical velocities is found to depend mainly on the relative magnitudes of the terms rather than on the uncertainties of the terms. For instance a certain error in the denominator, which introduces a small error in w when the denominator is large, can introduce a tremendous w-error when the denominator is small. Certain arbitrary, but reasonable, uncertainties in the observations – corresponding to average conditions rather than extreme conditions – will be assigned. From the magnitude of the terms in each case, the effect of these observational uncertainties on the vertical velocity can then be computed.

From Equations (A-1) and (A-9) the following expression can be written:

$$w = \frac{-\frac{\partial T}{\partial t} + ADV + \left.\frac{dT}{dt}\right|_D}{\Gamma - \gamma} \equiv \frac{N}{S} \quad , \tag{A-19}$$

where

$$S \equiv \Gamma - \gamma \; ; \; N \equiv -\frac{\partial T}{\partial t} + ADV + \left.\frac{dT}{dt}\right|_D$$

Since the errors in numerator and denominator are independent, from error theory and a Taylor series,

$$(\delta w)^2 = \left(\frac{\partial w}{\partial N}\,\delta N + \frac{\partial^2 w}{\partial N^2}\,\frac{(\delta N^2)}{2} + \ldots\right)^2 + \left(\frac{\partial w}{\partial S}\,\delta S + \frac{\partial^2 w}{\partial S^2}\,\frac{\delta S^2}{2} + \ldots\right)^2 \quad ,$$

where $\delta\chi$ indicates the uncertainty in χ .* The last set of terms will not converge unless $\delta S / S < 1$. With this condition convergence does result and

* The equations would be equally valid if $\delta\chi$ were the standard deviation, absolute deviation, RMS deviation, etc. as long as consistency is maintained.

$$(\delta w)^2 = w^2 \left[\left(\frac{\delta N}{N} \right) + \frac{(\delta S)^2}{S^2 + 2S\ \delta S + (\delta S)^2} \right]$$

For random δS errors, $S\,\delta S$ vanishes and

$$\left(\frac{\delta w}{w} \right)^2 = \left(\frac{\delta N}{N} \right)^2 + \frac{(\delta S)^2}{S^2 + (\delta S)^2} \quad ; \quad \frac{\delta S}{S} < 1 . \tag{A-20}$$

The uncertainty in the numerator is,

$$(\delta N)^2 = \left(\delta \frac{\partial T}{\partial t} \right)^2 + (\delta\, ADV)^2 + \left(\delta \left. \frac{dT}{dt} \right|_0 \right)^2 , \tag{A-21}$$

since the errors in the three terms are independent. Equation (A-11) can be re-written,

$$\frac{\partial T}{\partial t} = \frac{1}{DDT} \left[\frac{T_{+1} - T_0}{D} + (T_0 - T_{-1})\, D \right] ,$$

where

$$DDT \equiv t_{+1} - t_{-1} \quad ; \quad D \equiv \frac{t_{+1} - t_0}{t_0 - t_{-1}}$$

Notice that D is unity if the soundings are equally spaced in time. Since the errors in temperature of different soundings are independent, we can denote the uncertainty in any of the temperatures as δT. Therefore,

$$\left(\delta \frac{\partial T}{\partial t} \right)^2 = \left[\frac{2\,(D + 1/D^2 - 1)}{DDT^2} \right] (\delta T)^2 \equiv [DD]\ (\delta T)^2 . \tag{A-22}$$

ADV is proportional to: $- \left(\frac{\vec{V}_1 + \vec{V}_2}{2} \right) \cdot \left(\frac{\vec{V}_2 - \vec{V}_1}{2} \times \vec{k} \right)$

$$ADV = K \frac{\bar{p}}{p_2 - p_1} V_1 V_2 \sin \Delta\phi ,$$

where K is constant and the winds at levels p_2 and p_1 are (V_1 , ϕ_1) and (V_2 , ϕ_2) respectively, and $\Delta\phi \equiv \phi_2 - \phi_1$. $\bar{p}$ is the mean pressure between

between p_2 and p_1. Since we select a fixed pressure interval of 50 mb, only the winds are uncertain. Hence,

$$\frac{\delta \text{ ADV}}{\text{ADV}} = \frac{\delta (V_1 V_2 \sin \Delta\phi)}{V_1 V_2 \sin \Delta\phi} \tag{A-23}$$

To obtain an understanding of the uncertainties in the denominator, introduce the parameter ξ to indicate the fraction of the time during which the process is pseudo-adiabatic. We find

$$w = \frac{-\frac{\partial T}{\partial t} + \text{ADV} + \left.\frac{dT}{dt}\right|_D}{\gamma_d - \gamma - \xi (\gamma_d - \gamma_s)} , \tag{A-24}$$

where γ_d and γ_s are the dry and moist adiabatic lapse rates and are known very accurately. The uncertainty in the denominator can be written

$$(\delta S)^2 = (\delta\gamma)^2 + \left[(\gamma_d - \gamma_s)\, \delta\xi\right]^2 \tag{A-25}$$

Combining Equations (A-20) through (A-25),

$$\left(\frac{\delta w}{w}\right)^2 = \frac{D\,D(\delta T)^2 + \frac{\text{ADV}^2}{(V_1 V_2 \sin \Delta\phi)^2}\left[\delta (V_1 V_2 \sin \Delta\phi)\right]^2 + \left(\delta \left.\frac{dT}{dt}\right|_D\right)^2}{\left(-\frac{\partial T}{\partial t} + \text{ADV} + \left.\frac{dT}{dt}\right|_D\right)^2} + \frac{(\delta\gamma)^2 + \left[(\gamma_d - \gamma_s)\, \delta\xi\right]^2}{S^2 + (\delta\gamma)^2 + \left[(\gamma_d - \gamma_s)\, \delta\xi\right]^2} \tag{A-26}$$

Arbitrary, but reasonable, values can now be assigned to δT, $\delta (V_1 V_2 \sin \Delta\phi)$, $\delta \left.\frac{dT}{dt}\right|_D$, $\delta\gamma$, and $\delta\xi$, which will allow the computer to evaluate δw at each point. Each temperature is an average over 50 mb and will, on the average, depend on the temperature measured at two levels. Hence,

$$(\delta T)^2 = (\delta T_S)^2 + \frac{(\delta T_R)^2}{2} ,$$

where δT_R and δT_S are the random and systematic errors in the point measurements. We will assume $(\delta T)^2 = 0.18$, which corresponds to $(\delta T_S, \delta T_R)$ of (0.368°, 0.3°) or (0.3°, 0.425°).

Many times $\delta\xi$ will be zero – it is either dry adiabatic or moist adiabatic. Other times, however, even with soundings at close intervals, $\delta\xi$ may be about 0.2. We will assign $\delta S = 0.5°C/km$. This value is equivalent to $(\delta Y, \delta\xi)$ of (0.5, 0) or, at about 700 mb, (0.25, 0.20).

We will further assign $\delta(V_1 V_2 \sin\Delta\phi) / (V_1 V_2 \sin\Delta\phi)$ to be 0.28. Approximately,

$$\left[\frac{\delta(V_1 V_2 \sin\Delta\phi)}{V_1 V_2 \sin\Delta\phi}\right]^2 = \left[\frac{\delta(V_1 V_2)}{V_1 V_2}\right] + \left[\frac{\delta\,\Delta\phi}{\Delta\phi}\right]^2 ,$$

and with this approximation the value of 0.28 would correspond to $(\delta\,\Delta\phi/\Delta\phi$, $\delta V_1 V_2 / V_1 V_2)$ of (1/4, 6/50). The approximation is fairly valid except for large $\Delta\phi$, or when $\delta V_1 V_2$ is well correlated with $\delta\,\Delta\phi$.*

In Equation (A-26), $\delta \left.\frac{dT}{dt}\right|_D$ is immaterial unless it exceeds about 0.2°C per hour. For 50-mb layers averaged over several hours, diabatic effects are seldom of this magnitude. In cases of evaporation, however, this term is very large. As an example, the evaporation of 0.01 inch of precipitation in 100 mb in one hour corresponds to a $(dT/dt|_{evap.}$ of about 0.6°C/hour. It is very difficult to objectively calculate this effect for all the cases. Instead, we will neglect $(dT/dt)|_{evap.}$ in the computations and consider it qualitatively in the analysis and quantitatively for selected cases.

With the above assignments of measurement uncertainties and the relegation of important diabatic effects to qualitative evaluation, Equation (A-26) becomes,

$$\left(\frac{\delta w}{w}\right)^2 = \frac{0.18\,DD + 0.0784\,ADV^2}{\left(-\frac{\partial T}{\partial t} + ADV\right)^2} + \frac{0.25}{S^2 + 0.25} \qquad \text{(A-27)}$$

It is this equation that was used in computing the uncertainties in the individual vertical velocities. The two terms on the right reflect the contribution of uncertainties in the numerator and denominator, respectively, to the uncertainty in w. The

* The validity of the approximation has no direct bearing on the computations, but only on interpreting the significance of the assigned uncertainty, 0.28.

contribution of these two factors was computed and listed separately along with the total δw .

For the much needed 'summary and conclusions' of this appendix, the reader is referred to Section 3. 3 in the text.

Appendix B

SELECTED CHARTS FROM THE ANALYSIS REPORTS

Figures B-1, B-2 and B-3 are the time-section analyses which appeared in Volumes II, III, and IV, respectively, of the analysis reports.[32, 33, 34]. The frontal analyses are based primarily upon the thermal field and considerable weight has been given to continuity, in time and space, on the synoptic constant-level charts. The cloud analyses in Figures 4, 5, and 6 are believed to be more accurate in those places where they differ from the preliminary analyses in this appendix.

Figures B-4 through B-14 contain the surface and 500-mb charts for selected periods covered by the time sections. These charts represent only a portion of the material available in the analysis reports.

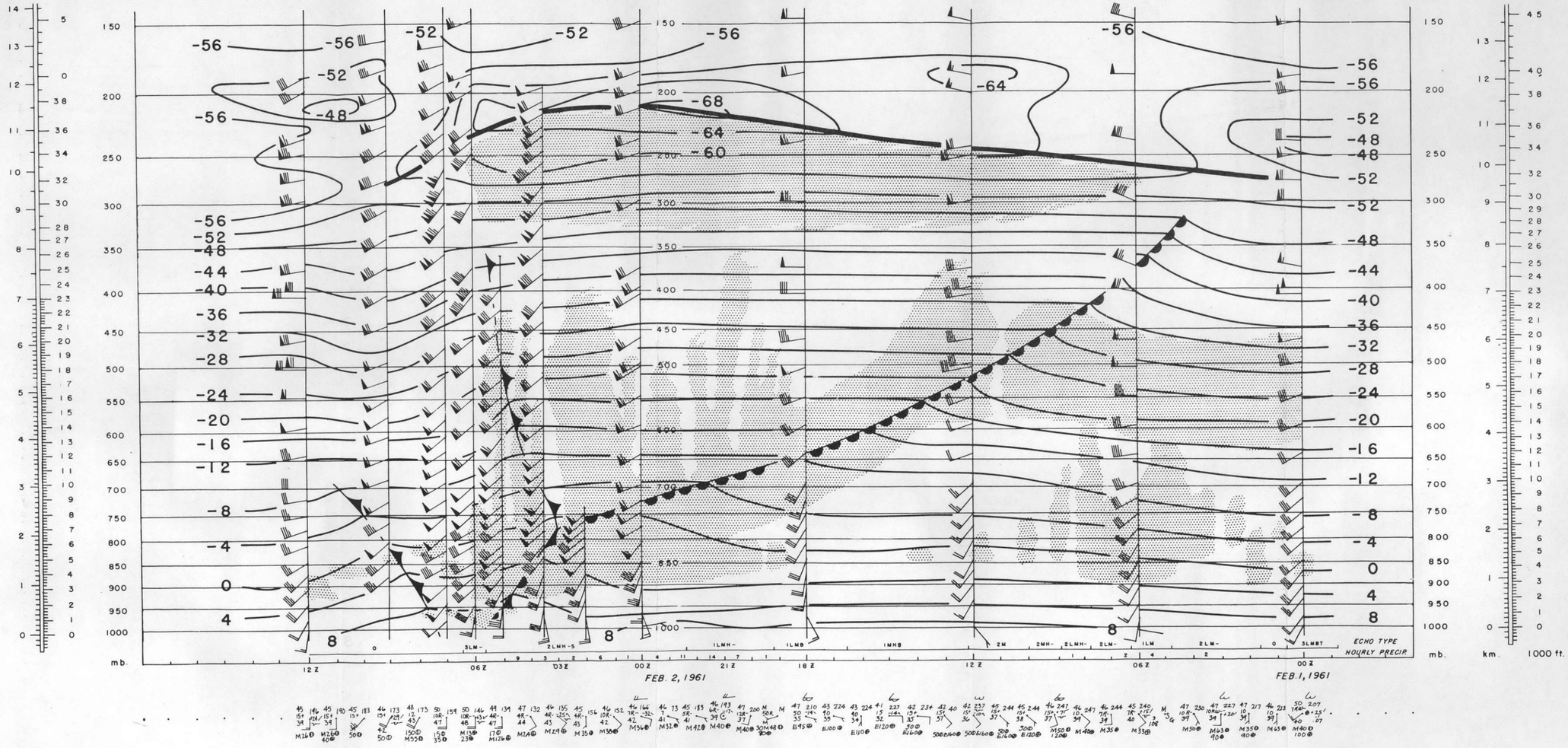

Figure B-1. Time Section for Seattle, February 1, 2, 1961. Winds denoted by usual convention. Heavy lines represent frontal, inversion, or tropopause discontinuities; fine lines, isotherms. Estimated cloud areas are stippled. Echo type, hourly precipitation (in hundredths of an inch), and hourly surface observations (at SEA) are entered at the bottom of the section. Soundings are plotted at observation time (30 minutes after time of release).

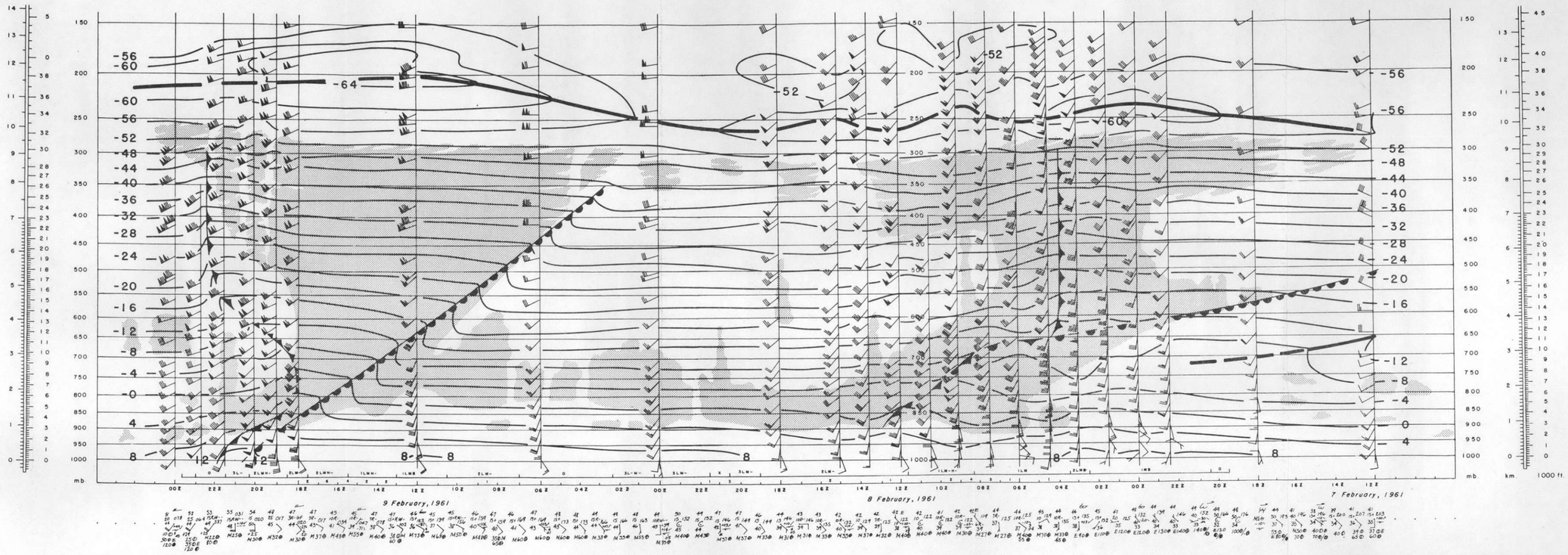

Figure B-2. Time Section for Seattle, February 7-10, 1961. Winds denoted by usual convention. Heavy lines represent frontal, inversion, or tropopause discontinuities; fine lines, isotherms. Estimated cloud areas are stippled. Echo type, hourly precipitation (in hundredths of an inch), and hourly surface observations (at SEA) are entered at the bottom of the section. Soundings are plotted at observation time (30 minutes after time of release).

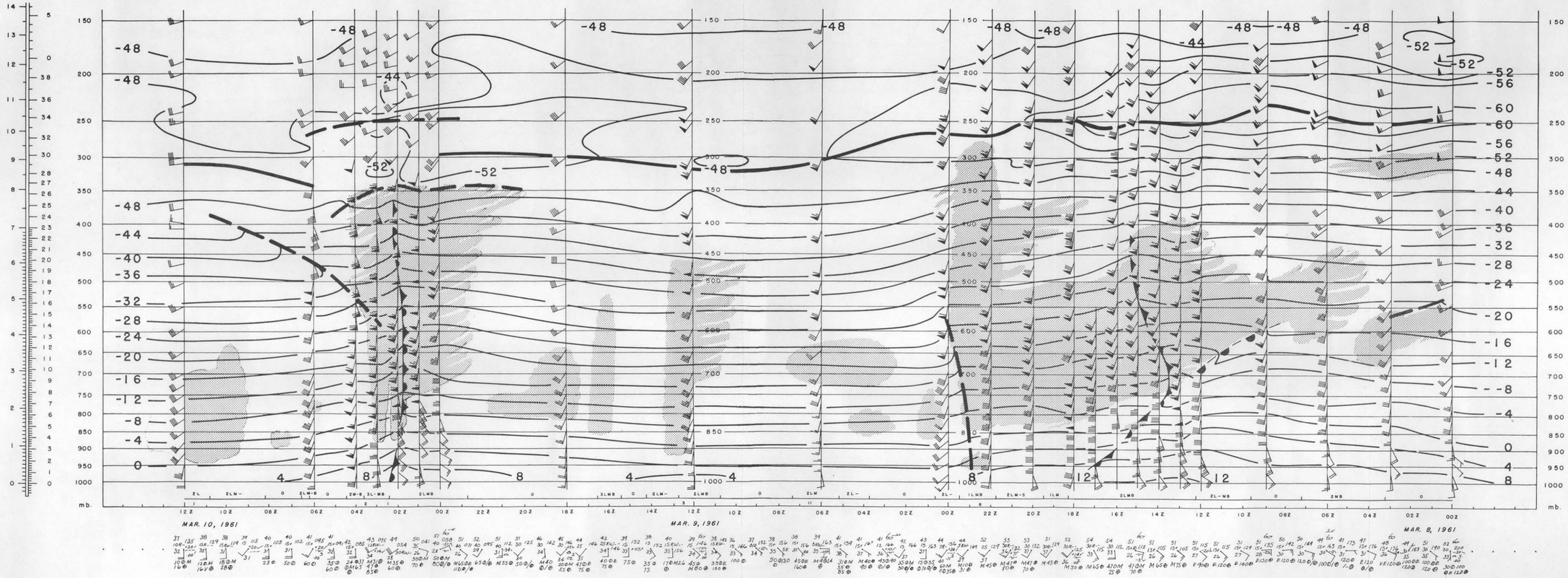

Figure B-3. Time Section for Seattle, March 8-10, 1961. Winds denoted by usual convention. Heavy lines represent frontal, inversion, or tropopause discontinuities; fine lines, isotherms. Estimated cloud areas are stippled. Echo type, hourly precipitation (in hundredths of an inch), and hourly surface observations (at SEA) are entered at the bottom of the section.

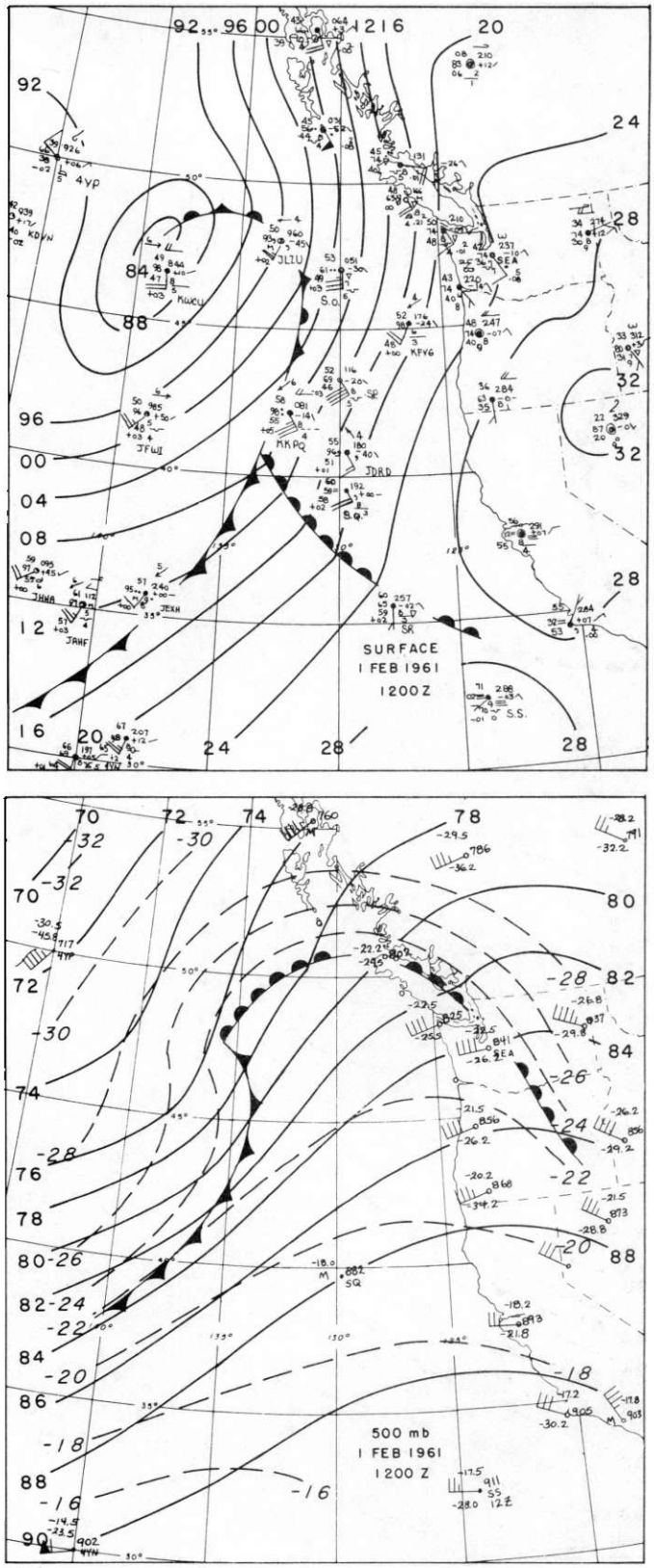

Figure B-4. Charts for 1200 GCT February 1, 1961. Upper, surface; lower, 500-mb.

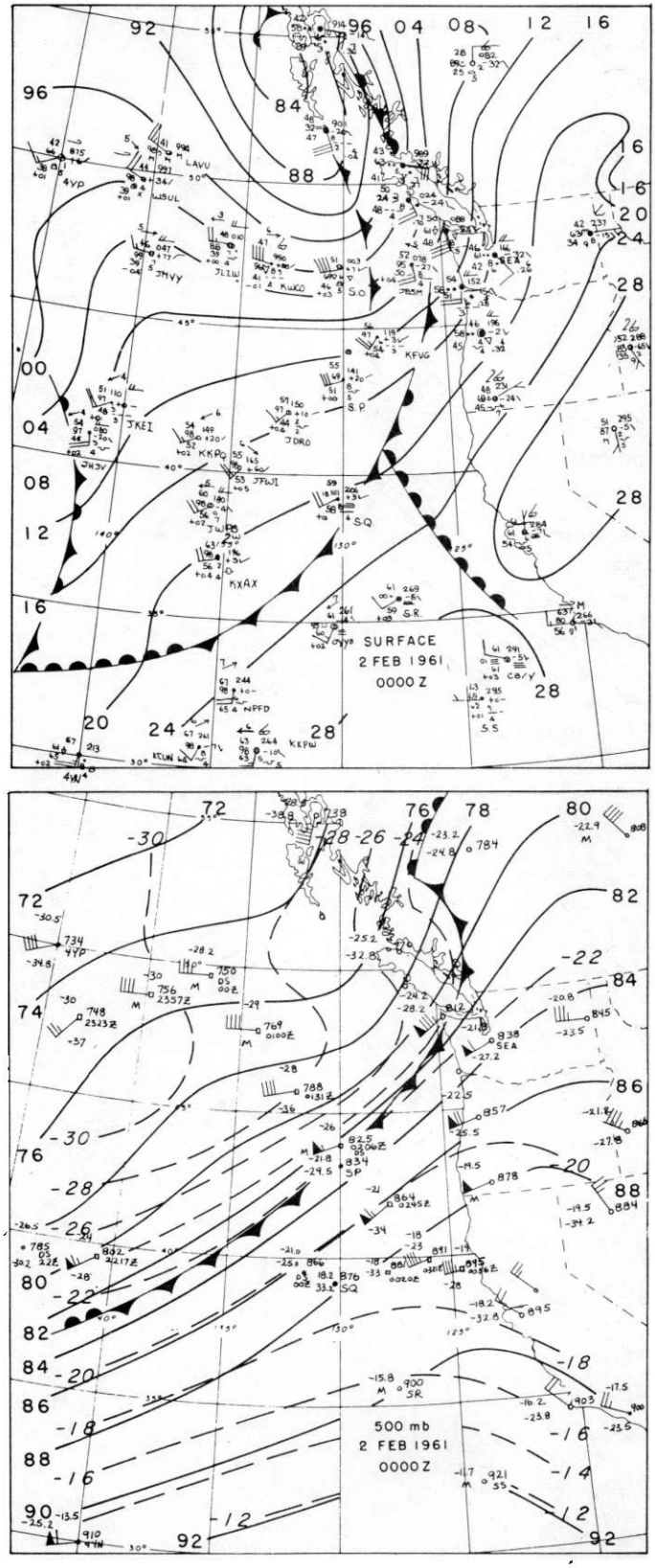

Figure B-5. Charts for 0000 GCT February 2, 1961. Upper, surface; lower, 500-mb.

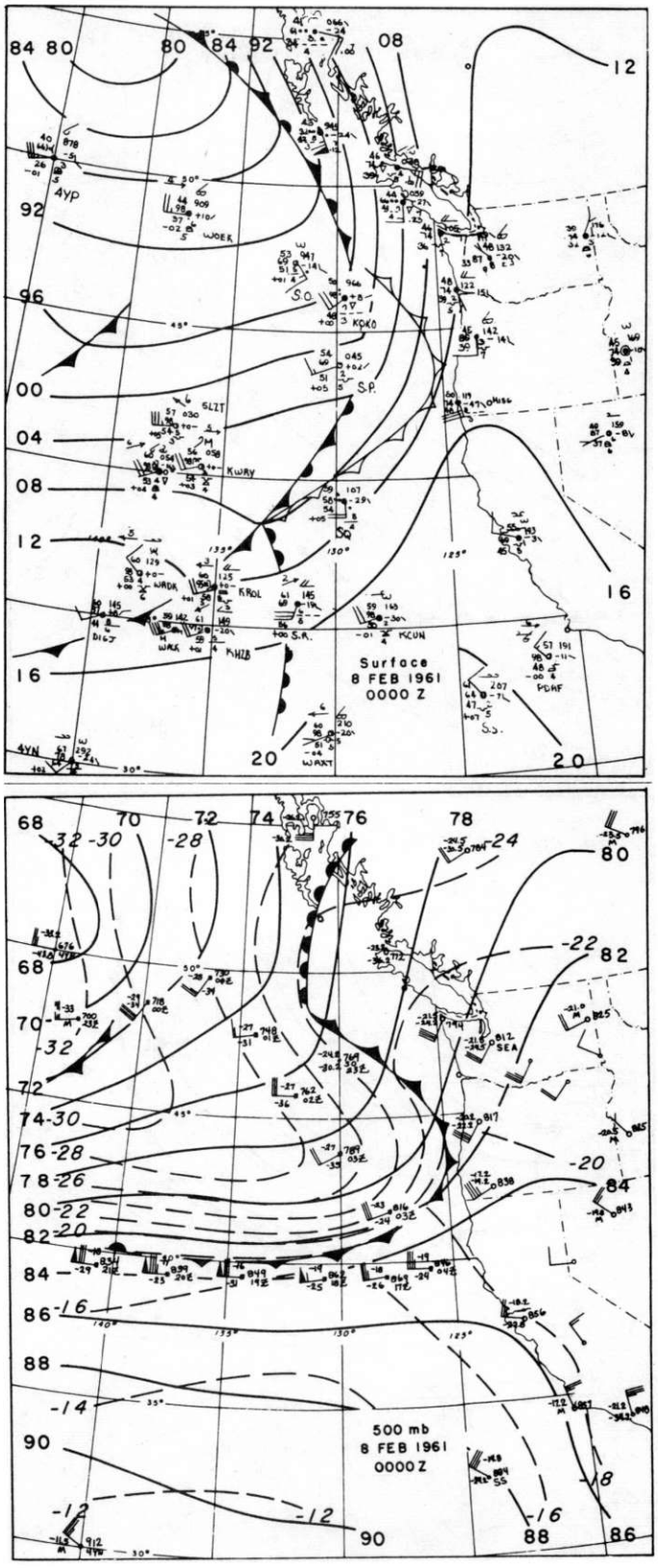

Figure B-6. Charts for 0000 GCT, February 8, 1961. Upper, surface; lower, 500-mb.

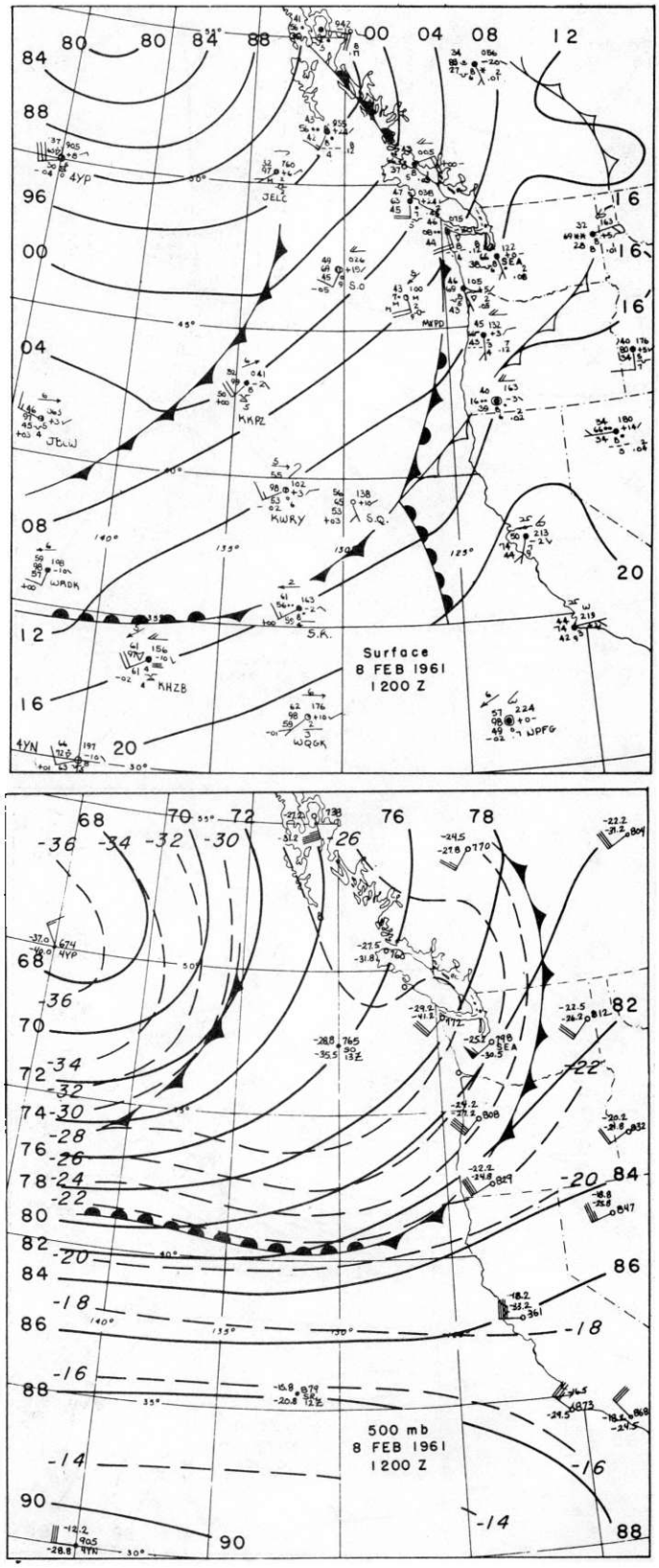

Figure B-7. Charts for 1200 GCT, February 8, 1961. Upper, surface; lower, 500-mb.

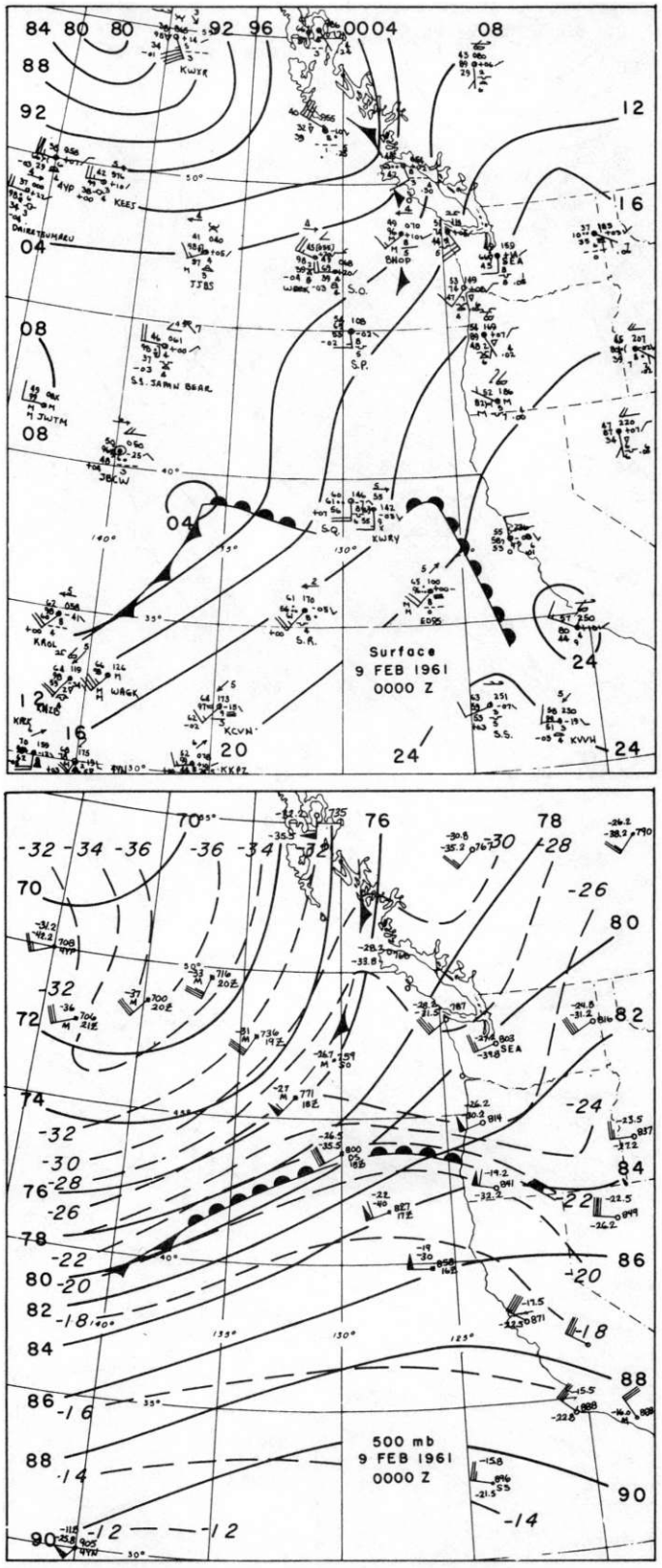

Figure B-8. Charts for 0000 GCT, February 9, 1961. Upper, surface; lower, 500-mb.

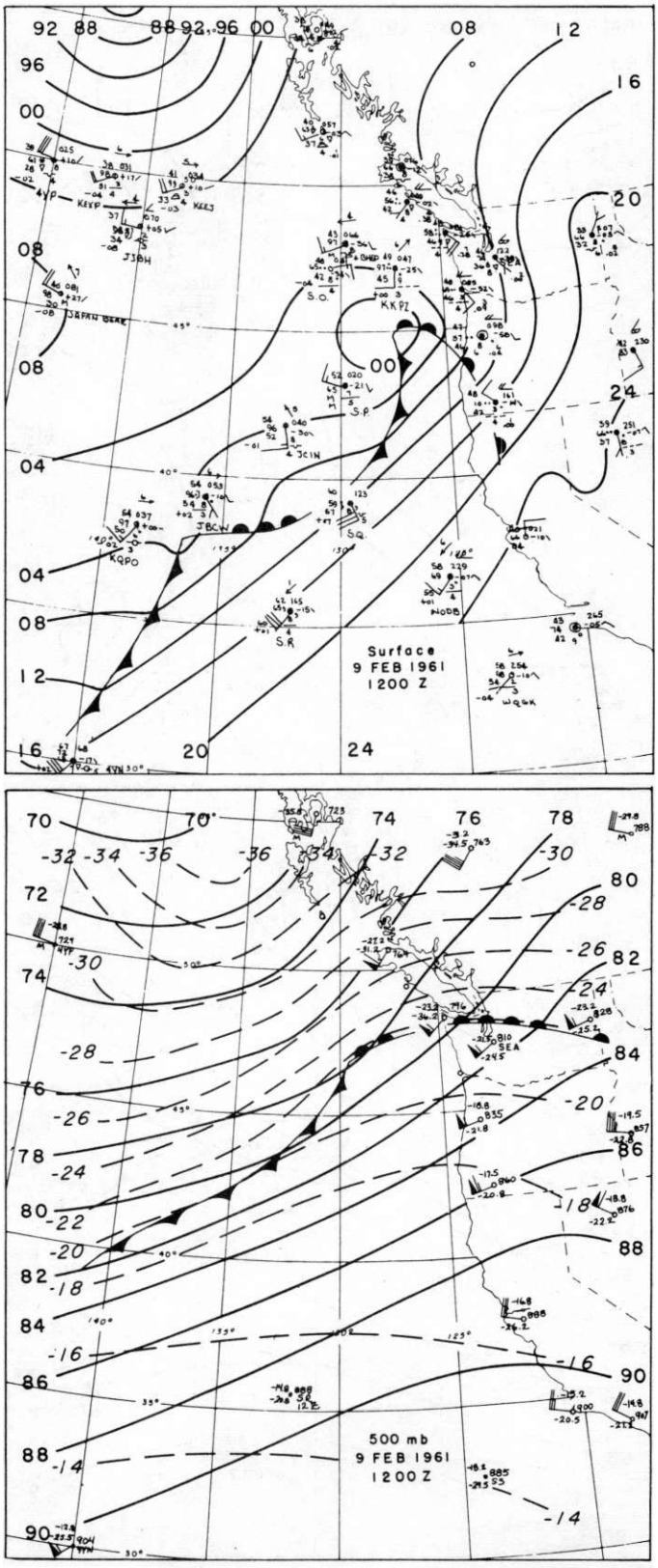

Figure B-9. Charts for 1200 GCT, February 9, 1961. Upper, surface; lower, 500-mb.

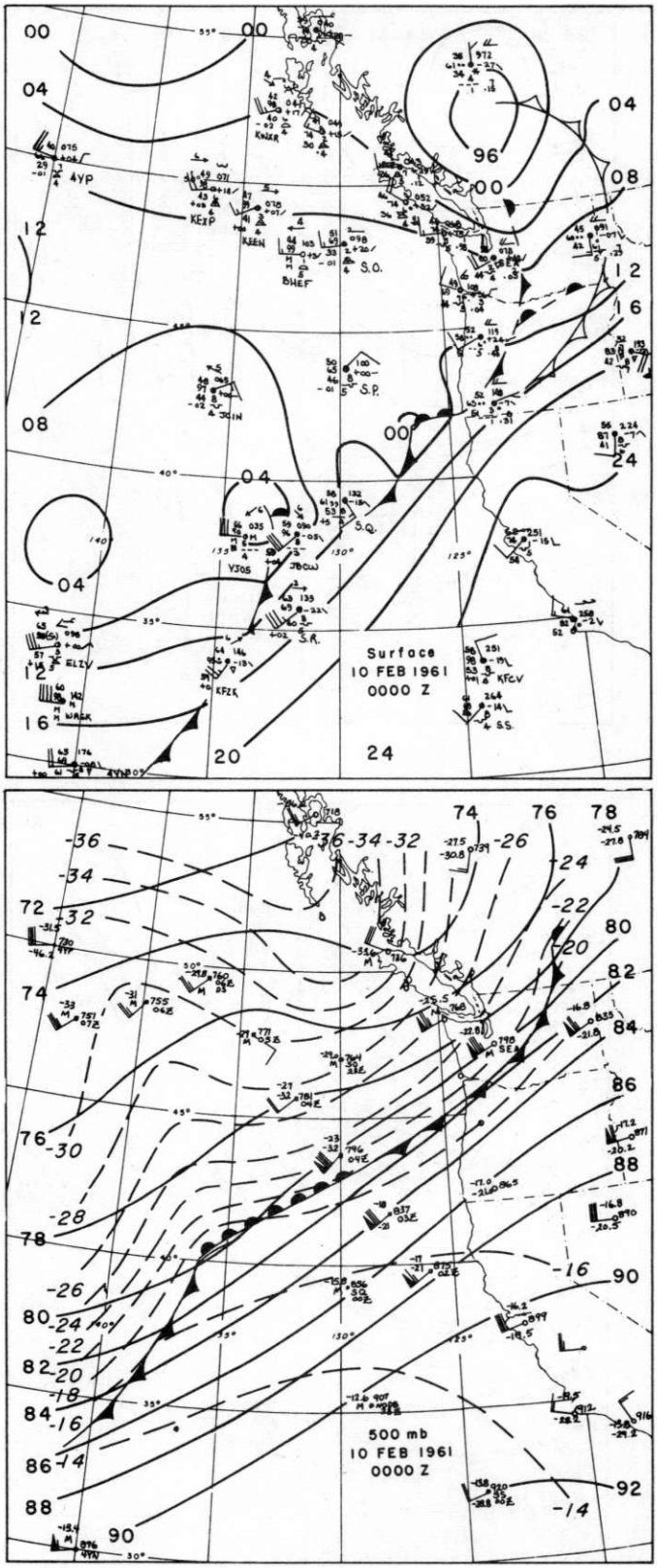

Figure B-10. Charts for 0000 GCT, February 10, 1961. Upper, surface, lower, 500-mb.

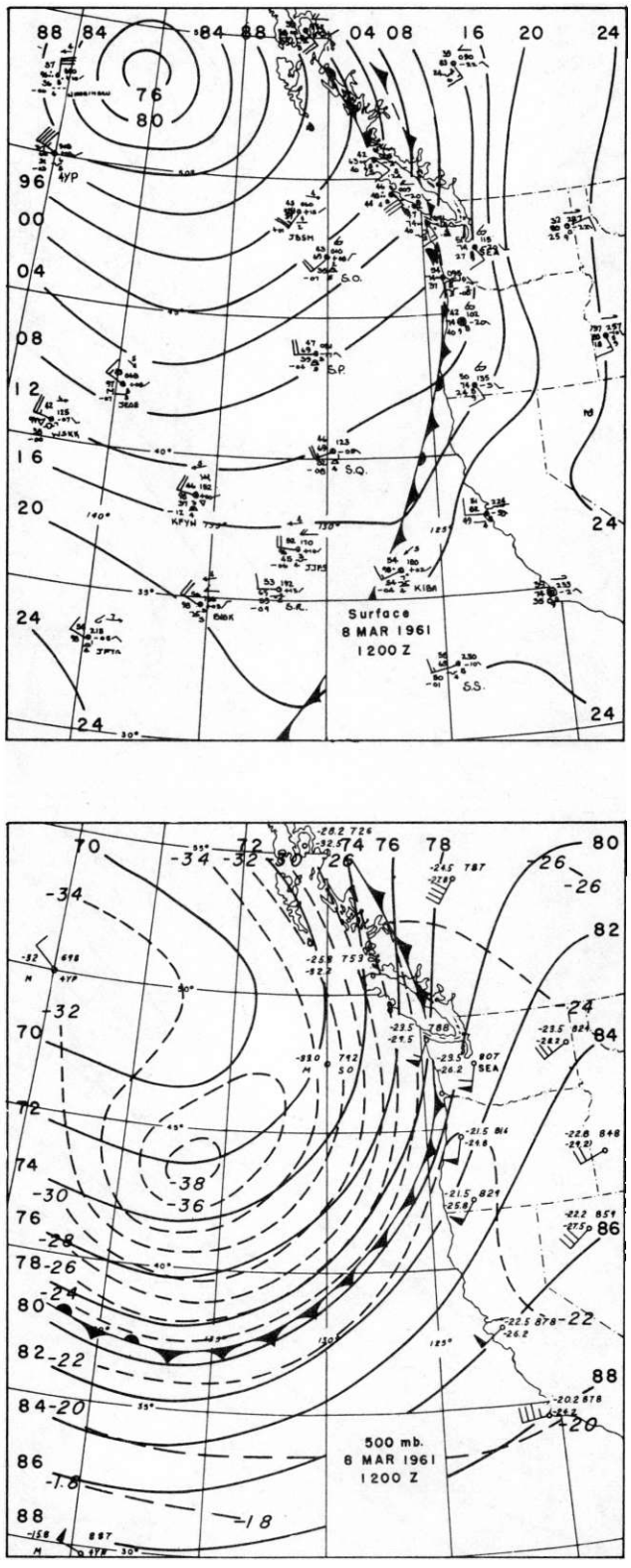

Figure B-11. Charts for 1200 GCT, March 8, 1961. Upper, surface; lower, 500-mb.

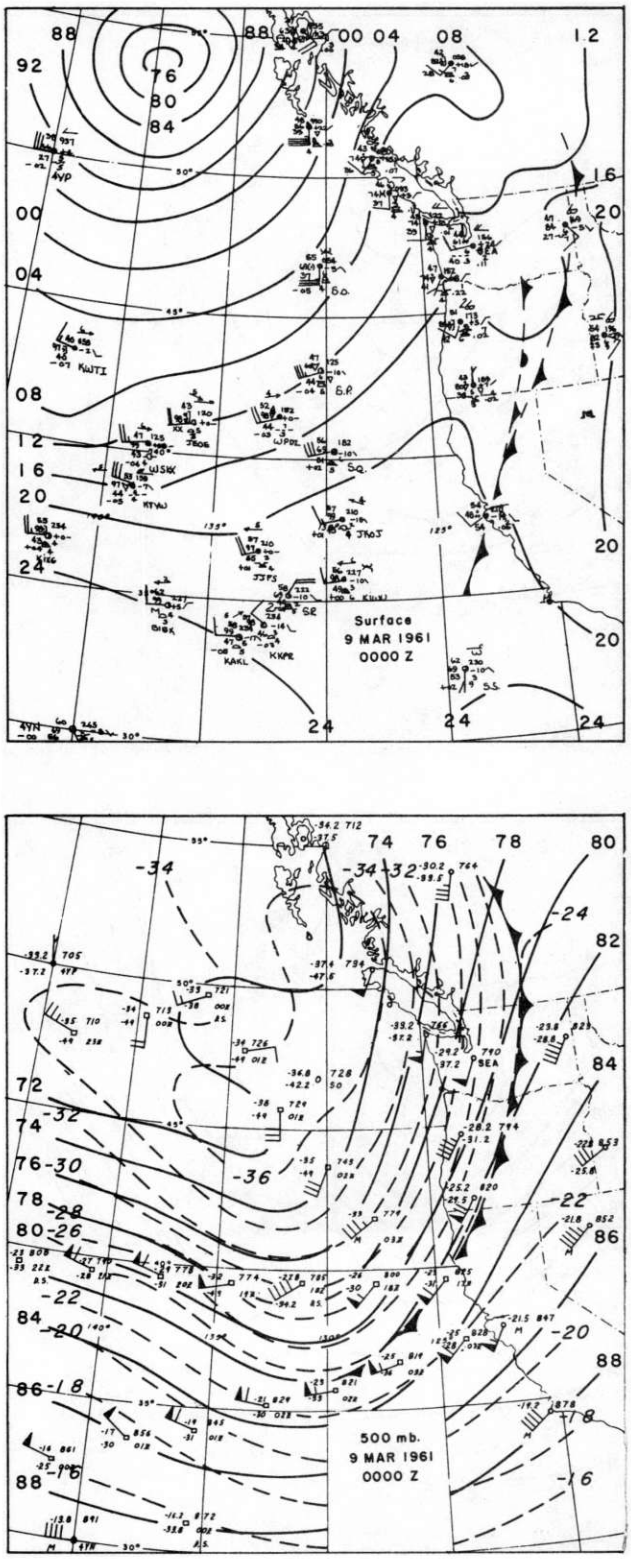

Figure B-12. Charts for 0000 GCT, March 9, 1961. Upper, surface; lower, 500-mb.

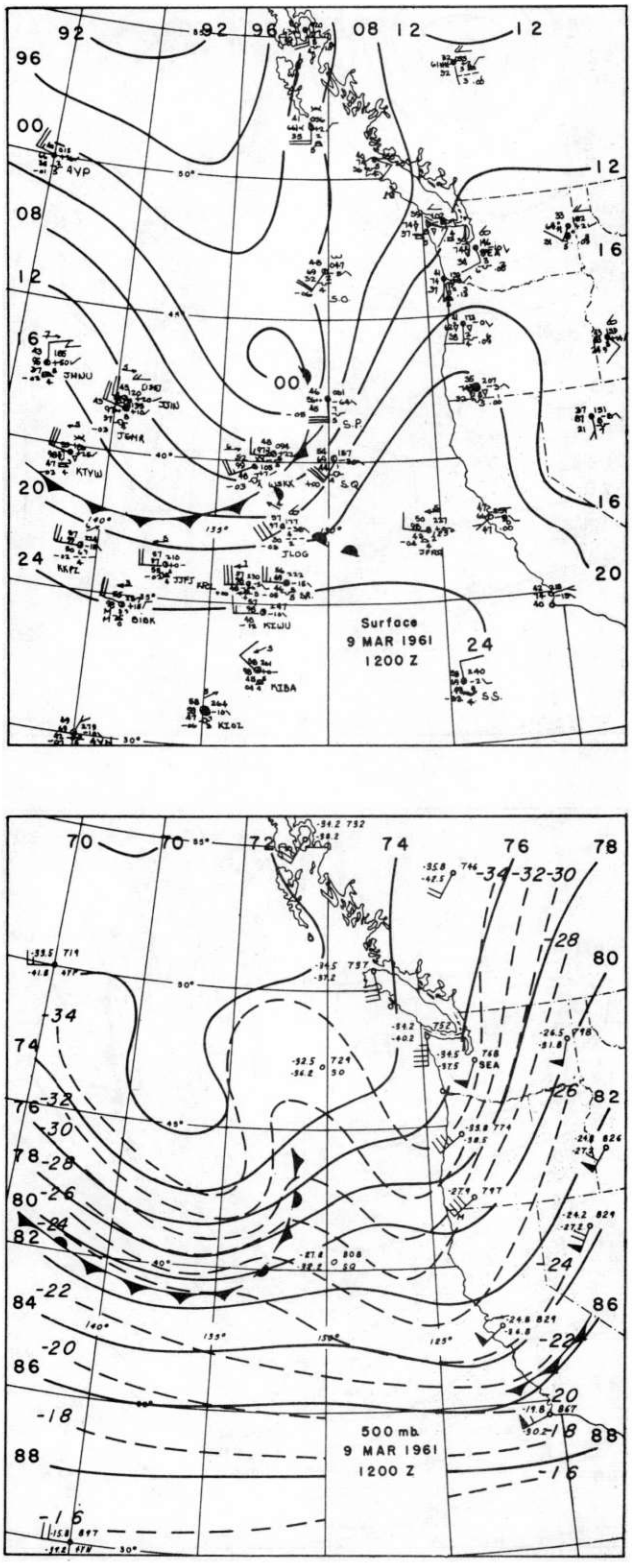

Figure B-13. Charts for 1200 GCT, March 9, 1961. Upper, surface; lower, 500-mb.

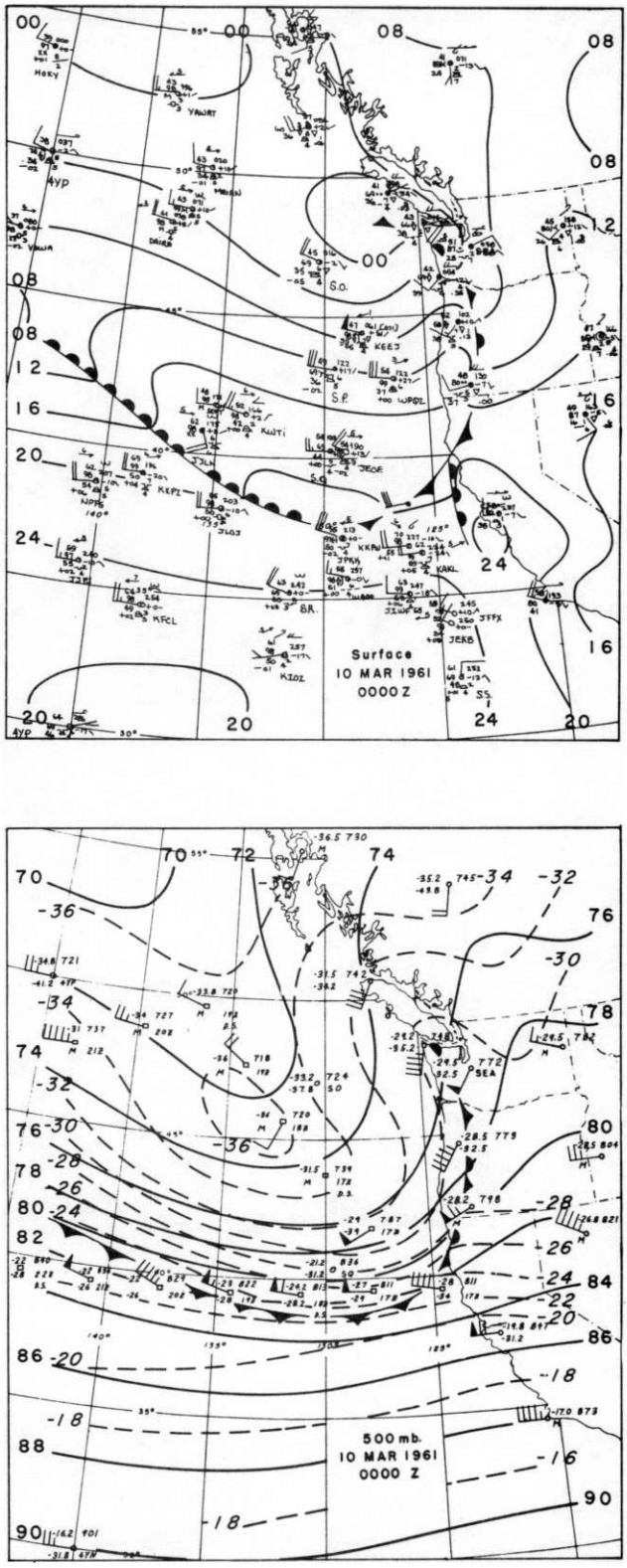

Figure B-14. Charts for 0000 GCT, March 10, 1961. Upper, surface; lower, 500-mb.

References

1. T. BERGERON, Methods in scientific weather analysis and forecasting, The Atmosphere and Sea in Motion, New York, The Rockefeller Institute Press, 440-474 (1959).
2. C. L. GODSKE, T. BERGERON, J. BJERKNES, and R. C. BUNDGAARD, Dynamic Meteorology and Weather Forecasting, Boston, Amer. Meteor. Soc.; Washington, D. C., Carnegie Institution of Washington, 800 pp. (1957).
3. J. BJERKNES and E. PALMÉN, Investigation of selected European cyclones by means of serial ascents, Geofys, Publ., 12(2):5-62 (1937).
4. T. BERGERON, On the physics of fronts, Bull. Amer. Meteor. Soc., 18:265-275 (1937).
5. R. C. SUTCLIFFE, Principles of synoptic weather forecasting, Quart. J. Roy. Meteor. Soc., 78: 291-320 (1952).
6. E. PALMÉN, The aerology of extratropical disturbances, Compendium of Meteorology, Boston, Amer. Meteor. Soc., 599-620 (1951).
7. W. L. GODSON, The structure of North American weather systems, Centenary Proc. Roy. Meteor. Soc., London, 89-106 (1950).
8. W. L. GODSON, The synoptic properties of frontal surfaces, Quart. J. Roy. Meteor. Soc., 77: 633-653 (1951).
9. A. L. JACOBSON, Some remarks on frontal structure, U.S. Weather Bureau, Great Falls, Montana, 21 pp. (unpublished).
10. J. J. TALJAARD, W. SCHMITT, and H. VAN LOON, Frontal analysis with application to the Southern Hemisphere, Notos, 10(1-4): 25-58 (1961).
11. R. J. REED, A study of a characteristic type of upper-level frontogenesis, J. Meteor., 12: 226-237 (1955).
12. R. J. REED, and E. F. DANIELSEN, Fronts in the vicinity of the tropopause, Arch. Meteor. Geophys. u. Bioklimatol., Ser. A., 11: 1-17 (1959).
13. R. M. ENDLICH, and G. S. McLEAN, The structure of the jet stream core, J. of Meteor., 14: 543-552 (1957).

14. C. W. NEWTON, Variation in frontal structure of upper level troughs, Geophysica, 6(3-4): 357-375 (1958).

15. H. L. KUO, Three-dimensional disturbances in a baroclinic zonal current, J. Meteor., 9: 260-278 (1952).

16. E. F. DANIELSEN and E. P. McCLAIN, Zonal distribution of baroclinity for three Pacific storms, J. Meteor., 12: 314-323, (1955).

17. J. S. SAWYER, The free atmosphere in the vicinity of fronts, Geophys. Mem. No. 96, Great Britain Meteorological Office, M. O. 584d, 24 pp. (1955).

18. C. F. BROOKS, A cloud cross section of a winter cyclone, Mon. Wea. Rev., 48: 26-28 (1920).

19. R. J. BOUCHER, Synoptic-physical implications of 1.25 cm vertical beam radar echoes, Meteor. Radar Studies No. 5, Blue Hill Meteorological Observatories, Harvard University (1957).

20. R. J. BOUCHER, and R. J. NEWCOMB, Synoptic interpretation of some TIROS vortex patterns: a preliminary cyclone model, J. Appl. Meteor., 1: 127-136 (1962).

21. R. E. NAGLE and S. M. SEREBRENY, Radar precipitation echo and satellite cloud observations of a maritime cyclone, J. Appl. Meteor., 1: 279-295 (1962).

22. W. H. HOECKER, Cloud systems and precipitation processes in Pacific Coast storms, Mon. Wea. Rev., 84: 421-426 (1956).

23. F. HALL, Storm structure in Pacific Coast cyclones, U.S. Weather Bureau Manuscript, March 1956. (Also presented to a meeting of the Amer. Meteor. Soc., January 1956)

24. J. H. CONOVER and S. H. WOLLASTON, Cloud systems of a winter cyclone, J. Meteor., 6: 249-260 (1949).

25. J. M. AUSTIN and R. H. BLACKMER, Variability of cold front precipitation, Bull. Amer. Meteor. Soc., 37: 447-453 (1956).

26. H. W. SANSOM, A study of cold fronts over the British Isles, Quart. J. Roy. Meteor. Soc., 77: 96-120 (1951).

27. L. J. BATTAN, Radar Meteorology, Chicago, The University of Chicago Press, 161 pp. (1959).

28. B. J. MASON, The Physics of Clouds, Oxford University Press, London, England, 481 pp. (1957).

29. C. W. KREITZBERG, Preliminary results of a study of Pacific storm systems using 1.87 cm radar, Tech. Note No. 1, Contract AF 19(604)-5192, University of Washington (1961).

30. D. ATLAS, The origin of "stalactites" on precipitation echoes, Proc. Fifth Weather Radar Conf., Boston, Amer. Meteor. Soc., 329-334 (1955).

31. R. J. REED, Case of January 6-8, Tech. Report No. 3, Contract AF 19(604)-5192, University of Washington, 44 pp. (1961).

32. C. W. KREITZBERG and R. J. REED, Case of February 1-2, 1961, Tech. Rept. No. 4, Contract AF 19(604)-5192, University of Washington, 46 pp. (1961).

33. C. W. KREITZBERG and R. J. REED, Case of February 7-10, 1961, Tech. R Rept. No. 5, Contract AF 19(604)-5192, University of Washington, 64 pp. (1961).

34. C. W. KREITZBERG, Volume 4, Case of March 8-10, 1961, Tech. Rept. No. 6, Contract AF 19(604)-5192, University of Washington, 72 pp. (1961).

35. R. J. REED, Volume 5, Case of June 5-7, 1961, Tech. Rept. No. 7, Contract AF 19(604)-5192, University of Washington, 55 pp. (1961).

36. R. J. LIST, Smithsonian Meteorological Tables, Sixth Revised Edition. Smithsonian Institute, Washington, D. C., p. 350, (1958).

37. M. ERICKON, Study of turbulence and vertical motion in the upper atmosphere derived from ascension rates of balloons, Geophysica, 4(4):153-174, (1954).

38. K. L. SINKA, Determination of radiosonde ascent rates, Sci. and Cult., 22: 684-686, (1957).

39. G. J. HALTINER and F. L. MARTIN, Dynamic and Physical Meteorology, McGraw Hill, New York, 470 pp. (1957).

40. R. J. REED and C. W. KREITZBERG, Application of radar data to problems in synoptic meteorology, Final Report, Contract AF 19(604)-5192, University of Washington, 82 pp. (1962).

41. L. A. VUORELA, A study of velocity distribution in some jet stream cases over western Europe, Geophysica, 6(2): 68-90 (1957).

42. P. J. KIEFER, The thermodynamic properties of water and water vapor, Mon. Wea. Rev., 69: 329-331 (1941).

43. N. R. BEERS, Meteorological thermodynamics and atmospheric statics, Handbook of Meteorology, McGraw-Hill, New York, 313-410 (1945).

44. S. PETTERSSEN, Weather Analysis and Forecasting, Vol. 1, McGraw-Hill, New York, 428 pp. (1956).

45. R. WEXLER and D. ATLAS, Precipitation generating cells, J. Meteor., 16: 327-332 (1959).

46. C. W. NEWTON, Structure and mechanism of the pre-frontal squall line, J. Meteor., 7: 210-222 (1950).

47. A. ELIASSEN, On the vertical circulation in frontal zones, Geofys. Publ., 24: 147-160 (1962).

48. W. J. SAUCIER, Principles of Meteorological Analysis, The University of Chicago Press, Chicago, Illinois, 438 pp. (1955).

49. E. F. DANIELSEN, The laminar structure of the atmosphere and its relation to the concept of a tropopause, Arch. Meteor. Geophys. u Bioklimatol., Ser. A 11: 293-332 (1959).

50. D. P. McINTYRE, The Canadian 3-front, 3-jet stream model, Geophysica, 6(3-4): 309-324 (1958).

51. J. A. LEESE, The role of advection in the formation of vortex cloud patterns, Tellus, 14: 409-421 (1962).

52. R. C. SUTCLIFFE, A contribution to the problem of development, Quart. J. Roy. Meteor. Soc., 73: 370-383 (1947).

53. F. SANDERS, A. J. WAGNER, and T. N. CARLSON, Specification of cloudiness and precipitation by multi-level dynamical models, Scientific Report No. 1, Contract AF 19(604)-5491, Massachusetts Institute of Technology, 111 pp. (1960).

54. R. S. SCORER, Natural Aeronautics, Pergamon Press, New York, 312 pp. (1958).

55. C. W. NEWTON and H. R. NEWTON, Dynamical interactions between large convective clouds and environment with vertical shear, J. Meteor., 16: 483-496 (1959).

GENERAL DESIGN CO., BEDFORD, MASS.